Energy-Based Wetting for Color-Gradient Lattice Boltzmann Fluid Simulations

Ezra Kas
5687292

A thesis presented for the degree of
Master of Science
at the Delft University of Technology
to be defended publicly on Wednesday, November 27th at 1:00 PM.

Assessment Committee
Dr. Gianluca di Staso (Flow Matters Consultancy, TU Eindhoven)
Dr. Remco M. Hartkamp (TU Delft)
Prof. Johan T. Padding (TU Delft)
Dr. Martin Rohde (TU Delft)
Dr. Peter R. Wellens (TU Delft)

Energy, Flow & Process Technology
TU Delft
Netherlands
November 27th 2024

TU Delft Delft University of Technology

ABSTRACT

Drop-on-Demand Inkjet Printing requires jetting ink particles at 100kHz at velocities of 10m/s from sub-millimeter-scale printhead assemblies, and represents a physics-rich engineering problem. CFD simulations have been used to study the jetting process. From meniscus deformation at the nozzle, to the presence of entrained particles in the jet, modeling contact line dynamics is very important.

Color-Gradient Lattice Boltzmann (CG-LBM) simulations can capture surface tension between fluids. Contact angles with solids are often imposed on geometrical grounds as boundary conditions. Alternative *energy-based* wetting, based on solid-liquid surface tension/energy arguments, is investigated for its applicability in the inkjet printing regime.

CG-LBM fluid-fluid interfaces are *diffuse*, despite modelling macroscopically sharp interfaces. This requires interpolation of viscosity in the interface region: new arguments are given to support the idea that this interpolation is free, and can be chosen, for example, on the basis of validation results.

New theory on CG-LBM for any number N of fluids is developed, and broadens the applicability of known N-fluid algorithms, allowing the use of in-simulation phase definitions that are more suitable for large density ratios among fluids.

The use of *superviscous particles* is investigated, where an N-fluid CG-LBM implementation is leveraged by using very viscous fluids to model solids. Wetting would then be mediated by the CG-LBM fluid-fluid interaction framework. The way CG-LBM maintains fluid-fluid interfaces is now also extended to the solid-fluid interfaces, and can lead to catastrophic spurious smearing of physical features.

Separately, recognizing the fundamental physical similarity of surface-tension across fluid-fluid and fluid-solid interfaces, wetting phenomena were simulated with additional fluid-fluid-like interactions near walls. This *solid-phase perturbation* approach was consistently formulated thanks to the new N-fluid CG-LBM theory developed earlier. Inaccuracies arise when these interactions are not paired with a diffuse fluid-solid interface, similar to those maintained between fluids in CG-LBM.

Sufficient results are obtained to motivate future development of solid-phase perturbation, which indeed describes solid-fluid and fluid-fluid surface-tensile interaction in a unified framework.

Contents

List of Figures

List of Tables

Chapter 1 | Introduction

1.1 Drop-on-Demand Inkjet Printing

Inkjet printing is familiar for its application to graphical printing, but should be viewed fundamentally as a sophisticated additive manufacturing or physical processing technique, with applications in the electronics or pharmaceutical industries for example. Such applications can indeed benefit from the technique's precise control of delivered material and extreme achievable reliability [13, 22].

Whereas other older techniques used a continuous ink-jet's instability and tendency to breakup into droplets, *drop-on-demand* inkjet printing produces every drop individually by using a pressure-wave in the printhead with a piezoelectric actuator. The interface with ambient air at the nozzle responds to this wave and deforms, releasing a small jet which forms into a droplet. This principle is shown in figure 1.1. From the printhead acoustics, surface-tensile effects and wetting near the nozzle, jet instabilities and droplet in-flight dynamics, splashing and other phenomena on the substrate, all occurring for a sub-millimeter-scale printhead assembly to eject micrometer-scale droplets at frequencies reaching $100\mathrm{kHz}$ and velocities of $10\,\mathrm{m\,s^{-1}}$, drop-on-demand inkjet printing is clearly a very physics-rich engineering problem[2, 13, 22].

Drop-on-demand inkjet printing demands extreme reliability, from droplet production to impact [13]. Because an accurate description of this microfluidic multiphase flow is necessary to good R&D, and due to prototyping requirements and the difficulty of measurement (e.g. optical) access at such scales, numerical modeling is a valuable tool to the development of better inkjet printing technology, also helping support experimental results with a common theoretical basis [13]. Current research interests are discussed in section 1.3, and have been tackled by Flow Matters Consultancy using *lattice Boltzmann* simulations.

1.2 Multiphase Lattice Boltzmann Simulations

The Navier-Stokes equations (NSE), the governing equations of fluid motion, can be solved numerically with traditional finite-difference, finite-volume, and finite-elements methods [3, 9]. *Lattice Boltzmann* is a family of alternative methods (LBM) which are profoundly different from the aforementioned discretization techniques, because the equation being solved, the Boltzmann equation, is *not* the NSE, and is not formulated for fluid flow. Indeed, while the NSE does describe fluid flow, the Boltzmann equation describes the dynamics of large numbers of idealized particles, which resemble molecules more than fluid elements [8, 17]. Remarkably, a mathematical link between Navier-Stokes and the Boltzmann equation means that solutions to the latter can be consistent with those of the former. A unique strength of LBM is that all major computational steps occur locally (in space and time) and are therefore completely independent of each other, allowing for straightforward massive parallelization which traditional techniques cannot match [8, 13]. LBM can be extended or reframed to study other advection-diffusion equations, multiphase flows, fluid-structure interaction, turbulence, non-hydrodynamic transport phenomena, and quantum mechanics [5, 6, 8, 17].

In LBM, the ability to act on simulated phenomena at the microscopic level greatly increases flexibility in defining boundary conditions, contributing to its popularity in simulating complex geometries such as porous media flow, and phenomena that can escape macroscopic formulation, such as phase change and capillary phenomena [6, 8, 16, 17]. This uniquely marks LBM as a suitable technique for porous media flows, with applications in geological engineering and carbon sequestration [4, 12, 20, 24], biological flows and cardiovascular pathologies in particular [8, 16, 23], electrolyzer, battery, and fuel cell research [1, 7, 10,

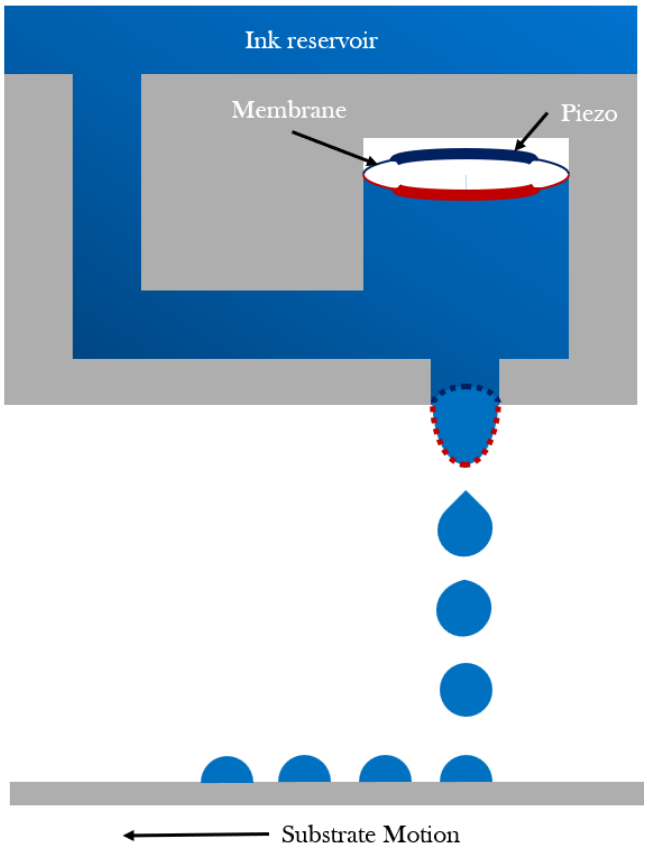

Figure 1.1: Drop-on-Demand Inkjet Printing Working Process. The piezoelectric element induces a pressure wave and flow inside the printhead, the energy of which is directed towards the meniscus at the nozzle. Fluid inertia pushes out a small jet, which forms a droplet. Adapted from [13].

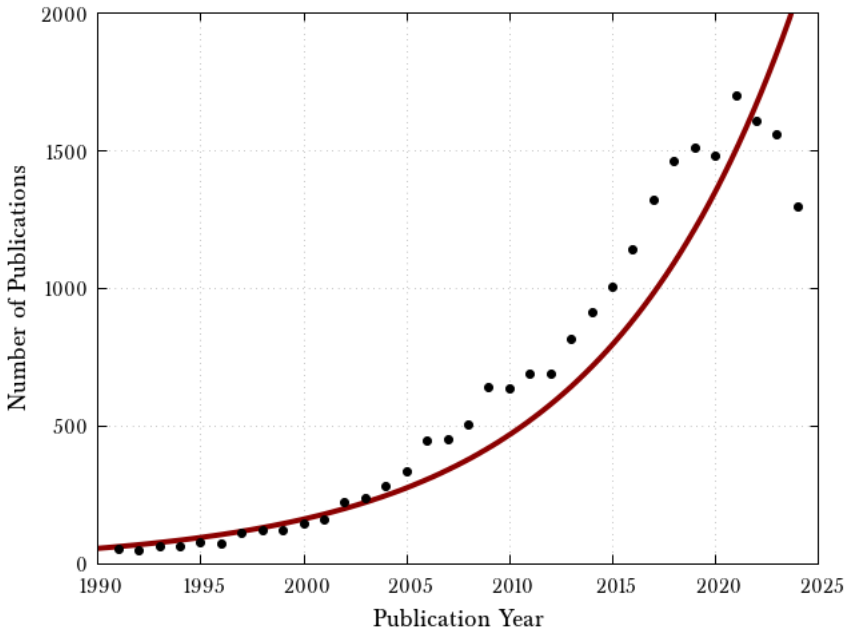

Figure 1.2: Publications over Time with "Lattice Boltzmann" as 'topic' (i.e. title, abstracts, and keywords) in the Web of Science database. Adapted from [18] with new data, retrieved on November 14th 2024.

11, 14, 15, 19, 21], clearly in line with UN sustainable development goals of Good Health and Well-Being, Affordable and Clean Energy, and Climate Action at the very least. These characteristics have contributed to an exponential increase in LBM-related publications, as seen in figure 1.2.

1.3 Research Question and Report Structure

Researchers associated with Flow Matters Consultancy have successfully used LBM to study drop-on-demand inkjet printing. This report's precursor work [2] demonstrated that LBM was comparably stable and accurate compared to established traditional methods. The ease of parallelization of LBM made it possible to efficiently investigate asymmetric jetting, most notably due to nozzle defects or entrained solid particles. Flow Matters Consultancy is specifically interested in better capturing meniscus contact-line dynamics and wetting on moving particles, and their effects on jet and droplet dynamics after ejection. The complexity of the simulated flow calls for continued development and especially improved support of dynamic capillary phenomena. Such phenomena are a subtle interplay of microscopic interactions, which combined with viscous and velocity-dependent parameters, have macroscopic consequences, raising the following question:

How can Lattice Boltzmann Methods be used to simulate multiphase flows with dynamic capillary phenomena?

To answer this question, part I will first summarize relevant background knowledge. Chapter 2 gives a general overview of the relevant fluid dynamics. Chapter 3 then describes the LBM implementation in the precursor work [2], *Color-Gradient LBM* (CG-LBM), which is suitable for multiphase simulations without phase-change.

Part II includes the literature review and new theory on multiphase LBM simulations. Chapter 4 refines the research question to investigate an intriguing class of wetting implementation, which mediates solid-fluid capillary interaction similarly to how fluid-fluid interaction is handled. A systematic review of the literature will confirm that these *energy-based* implementations have not been applied in the demanding

regime of drop-on-demand inkjet printing simulations. Chapter 5 describes which techniques will be attempted in the thesis, namely the use of very viscous fluids to model solids, and additional solid-fluid interactions near walls. Finally, chapter 6 presents new theory concerning multiphase simulations in LBM, extending the applicability of certain CG-LBM algorithms.

Part III contains the thesis' results from simulations. Chapter 7 documents the extension of Flow Matters' LBM code to support any number N of fluids. Chapter 8 discusses the use of *superviscous fluids* to model solids. CG-LBM is characterized by the use of diffuse (as opposed to sharp) interfaces between fluids, the effects of which on superviscous fluids have not been studied. Chapter 9 presents an adaptation of *solid-phase perturbation*, a technique that models wetting by setting surface-tensions between fluids and solids. Chapter 10 concludes on recommendations arising from this thesis' results.

Chapter 1 References

[1] M. Abubaker, C.H. Sohn, and H.M. Ali. "Wetting characteristics of Li-ion battery electrodes: Impact of calendaring and current collector contact angle - A Lattice Boltzmann Method investigation". In: *Energy Reports* 11 (2024). doi: 10.1016/j.egyr.2024.01.069.

[2] Karun Pravin Nirod Datadien. "Directional instabilities in microdroplet jetting: a numerical approach". PhD thesis. Applied Physics and Science Education, Jan. 31, 2024.

[3] J.H. Ferziger, M. Perić, and R.L. Street. *Computational Methods for Fluid Dynamics, Fourth Edition*. Computational Methods for Fluid Dynamics. 2019. 1 p. doi: 10.1007/978-3-319-99693-6.

[4] RC Guo et al. "Role of heterogeneous surface wettability on dynamic immiscible displacement, capillary pressure, and relative permeability in a CO2-water-rock system". In: *ADVANCES IN WATER RESOURCES* 165 (July 2022). doi: 10.1016/j.advwatres.2022.104226.

[5] Yangyu Guo and Moran Wang. "Lattice Boltzmann modeling of phonon transport". In: *Journal of Computational Physics* 315 (June 15, 2016). doi: 10.1016/j.jcp.2016.03.041.

[6] Haibo Huang, Michael C. Sukop, and Xi-Yun Lu. *Multiphase Lattice Boltzmann Methods: Theory and Application*. Wiley, July 2015. doi: 10.1002/9781118971451.

[7] DH Jeon et al. "Mechanistic Insight into Wettability Enhancement of Lithium-Ion Batteries Using a Ceramic-Coated Layer". In: *ACS NANO* 17.2 (Jan. 24, 2023). doi: 10.1021/acsnano.2c09526.

[8] Timm Krüger et al. *The Lattice Boltzmann Method: Principles and Practice*. Graduate Texts in Physics. Springer, 2016.

[9] Pijush K. Kundu et al. *Fluid Mechanics*. Sixth edition. Amsterdam: Elsevier/AP, 2016.

[10] Q. Li et al. "Effect of porous transport layer wettability on oxygen transportation in proton exchange membrane water electrolysis". In: *Journal of Power Sources* 606 (2024). doi: 10.1016/j.jpowsour.2024.234554.

[11] J. Liao et al. "Simulation of the purging process of liquid water in a gas diffusion layer with a wetting gradient using the lattice Boltzmann method". In: *Transport in Porous Media* 148.2 (2023). doi: 10.1007/s11242-023-01950-4.

[12] Haihu Liu et al. "Multiphase lattice Boltzmann simulations for porous media applications". In: *Computational Geosciences* 20.4 (Aug. 1, 2016). doi: 10.1007/s10596-015-9542-3.

[13] D. Lohse. "Fundamental Fluid Dynamics Challenges in Inkjet Printing". In: *Annual Review of Fluid Mechanics* 54 (2021). doi: 10.1146/annurev-fluid-022321-114001.

[14] T. Min and Q. Zhou. "Effects of liquid water on transport in the catalyst layer of proton exchange membrane fuel cells". In: *Frontiers in Energy Research* 11 (2023). doi: 10.3389/fenrg.2023.1330124.

[15] YT Mu et al. "Mesoscopic modeling impacts of liquid water saturation, and platinum distribution on gas transport resistances in a PEMFC catalyst layer". In: *ELECTROCHIMICA ACTA* 388 (Aug. 20, 2021). doi: 10.1016/j.electacta.2021.138659.

[16] K. J. Petersen, Joshua Brinkerhoff, and Joshua Brinkerhoff. "On the lattice Boltzmann method and its application to turbulent, multiphase flows of various fluids including cryogens: A review". In: *Physics of Fluids* 33.4 (Apr. 21, 2021). doi: 10.1063/5.0046938.

[17] S. Succi. *The lattice Boltzmann equation for fluid dynamics and beyond*. Numerical mathematics and scientific computation. Oxford, New York: Clarendon Press ; Oxford University Press, 2001.

[18] M.C. Sukop and D.T. Thorne. *Lattice boltzmann modeling: An introduction for geoscientists and engineers*. Lattice Boltzmann Modeling: An Introduction for Geoscientists and Engineers. 2006. 1 p. doi: 10.1007/978-3-540-27982-2.

[19] M. Suo et al. "Pore-scale numerical investigation of water transport in metal foam flow fields of proton exchange membrane fuel cells: Effect of structural parameters and wettability". In: *International Journal of Hydrogen Energy* 61 (2024). doi: 10.1016/j.ijhydene.2024.02.323.

[20] H Wang et al. "Pore-Scale Study on Shale Oil-CO2-Water Miscibility, Competitive Adsorption, and Multiphase Flow Behaviors". In: *LANGMUIR* (Aug. 15, 2023). doi: 10.1021/acs.langmuir.3c01570.

[21] J. Wanner and K.P. Birke. "Investigation of the influence of cell compression after winding on electrolyte wettability based on experiments and lattice Boltzmann simulation". In: *Journal of Energy Storage* 87 (2024). doi: 10.1016/j.est.2024.111410.

[22] Herman Wijshoff. "Structure and fluid-dynamics in piezo inkjet printheads". PhD thesis. University of Twente, Jan. 2008.

[23] Jingshu Wu and Cyrus K. Aidun. "Simulating 3D deformable particle suspensions using lattice Boltzmann method with discrete external boundary force". In: *International Journal for Numerical Methods in Fluids* 62.7 (Mar. 10, 2010). doi: 10.1002/fld.2043.

[24] T Zhang et al. "Pore-scale modelling of water sorption in nanopore systems of shale". In: *INTERNATIONAL JOURNAL OF COAL GEOLOGY* 273 (May 15, 2023). doi: 10.1016/j.coal.2023.104266.

Part I

Background

Chapter 2 | Fluid Dynamics

Key Points

- Continuum Fluid Dynamics are described by the Navier-Stokes equations.
- Multiphase Flows are characterized by the presence of several fluid or solid phases interacting with each other at interfaces.
- Interfacial phenomena related to intermolecular interactions manifest themselves at the macroscopic level as surface tension and wetting.
- Dimensionless Numbers can be used to identify hydrodynamic regimes and relevant physical phenomena.
- Drop-on-demand inkjet printing simulations must support large density and viscosity ratios, as well as capture capillary phenomena in dynamic situations.

In this chapter, a basic sense of multiphase fluid dynamics is provided to help identify the necessary capabilities of multiphase simulations of drop-on-demand inkjet printing.

2.1 The Navier-Stokes Equations

At the microscopic level, matter is described by the dynamics of individual atomic or subatomic particles. When a large enough number of these particles, constantly moving and undergoing interparticular interactions (e.g. collisions), are at sufficient density, they form a continuous substance which follows *fluid* behavior at a macroscopic level. A fluid is "a substance that deforms continuously under an applied shear stress"[9]. This means that a fluid element (a small volume within the bulk of fluid) will immediately deform in response to an applied shear stress. An *incompressible* fluid further does not exhibit any density variations. In that case, the following form of the *Navier-Stokes equations* (NSE) describes fluid mechanics [4, 8, 9]:

$$\rho \nabla \cdot \boldsymbol{u} = 0 \tag{2.1}$$

$$\frac{\partial \boldsymbol{u}}{\partial t} + \boldsymbol{u} \cdot \nabla \boldsymbol{u} = -\frac{1}{\rho}\nabla p + \frac{\mu}{\rho}\nabla^2 \boldsymbol{u} + \frac{\boldsymbol{F}}{\rho} \tag{2.2}$$

where equation (2.1) expresses mass conservation, and equation (2.2) momentum conservation; $\boldsymbol{u}$ is the local fluid velocity, p pressure, $\boldsymbol{F}$ is any kind of applied surface or body force, ρ is the density of the fluid, and μ is its (here, constant) dynamic viscosity, ∇ is the spatial gradient operator and t is time. The quantity $\nu = \mu/\rho$ is the fluid's kinematic viscosity. Boundary conditions to these partial differential equations notably include the *no-slip* boundary condition, where fluid in the immediate vicinity of a solid surface or wall must move at that wall's velocity.

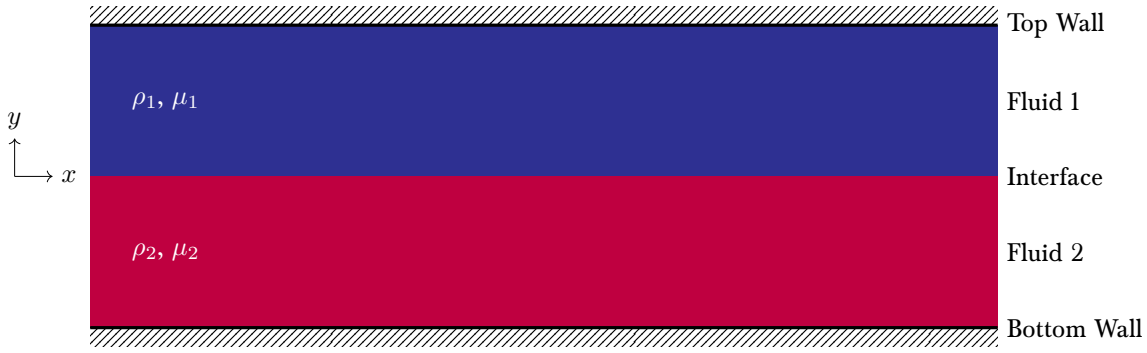

Figure 2.1: Stable, Laminar, Steady Stratified Couette Flow of fluid "1" over a fluid "2". Each has its own density and viscosity. Gravity is not considered here.

We can also write equation (2.2) with a material derivative $\frac{D}{Dt} = \frac{\partial}{\partial t} + \boldsymbol{u} \cdot \nabla$ [9]:

$$\frac{D}{Dt}(\rho \boldsymbol{u}) = -\nabla p + \mu \nabla^2 (\rho \boldsymbol{u}) + \boldsymbol{F} \tag{2.3}$$

The left-hand side is the material derivative of momentum, expressing the overall transport of fluid element momentum. This identifies the motors of fluid flow on the right-hand side: pressure gradients $-\nabla p$ and external forces $\boldsymbol{F}$. The $\mu \nabla^2 (\rho \boldsymbol{u})$ term represents viscous dissipation of momentum, and kinematic viscosity $\nu = \mu / \rho$ is therefore a ***momentum diffusivity***, playing the same role as heat diffusivity α in the heat equation[1]:

$$\frac{\partial T}{\partial t} = \alpha \nabla^2 T \tag{2.4}$$

where T is temperature. Since equation (2.4) describes the transport of heat by conduction alone, we clearly identify by analogy that viscosity and viscous dissipation tend to smoothen out momentum gradients.[1]

Returning to equation (2.2), we consider the flow field at a local point in space. With respect to some direction, a positive acceleration of the flow field (the first term on the left-hand side) is caused by forces in that direction, or favorable (negative) pressure gradients. The viscous term grows to the second order in $\boldsymbol{u}$: viscosity is a stabilizing term that always dissipates momentum, and does so increasingly with velocity. Conversely, the $\boldsymbol{u} \cdot \nabla \boldsymbol{u}$ advection term is nonlinear and notoriously troublesome, inviting chaos into the flow field, ultimately leading to the onset of turbulent flow [9, 11].

2.2 Multiphase Flows

Multiphase flow is characterized by the presence of additional fluid (gaseous or liquid) or solid phases in the flow. In the latter case, small solid particles could be entrained in the flow field. In the former, several fluids must be distinguishable at the macroscopic scale [2]: small bubbles of air entrained in water flow, stratified flow of oil above water, or the jetting of water through ambient air, for example.

Contact between distinguishable phases occurs at ***interfaces***. Air above a pool of water, for example, forms an interface with it. Just like a fluid typically obeys a no-slip boundary condition at a solid wall, additional boundary conditions apply at interfaces. Consider the stratified flow conditions of figure 2.1. At the moving top and fixed bottom wall, the fluids obey no-slip. But at the fluid-fluid interface, the shear stress of one fluid shears the other. An appropriate boundary condition is not no-slip, but a continuity of shear stresses, defined for fluids as:

$$\mu_1 \frac{\partial u_1}{\partial y}\bigg|_{\text{interface}} = \mu_2 \frac{\partial u_2}{\partial y}\bigg|_{\text{interface}} \tag{2.5}$$

[1]For incompressible flow, we can even claim that viscosity smoothens out *velocity* gradients.

where $\partial u_k/\partial y$ is the velocity gradient of fluid k orthogonal to the streamwise direction.[2] The existence of an interface between the two fluids implies that the fluids remain somewhat separate. If there is no mass-flux whatsoever across the interface, the fluids are *immiscible*, and there is no phase-change between the fluid phases: a fluid element in phase k located *at* the interface must not cross the interface. This corresponds to a kinematic boundary condition:

$$(\boldsymbol{u}_k \cdot \hat{\boldsymbol{n}})|_{\text{interface}} = \boldsymbol{u}_{\text{interface}} \cdot \hat{\boldsymbol{n}} \tag{2.6}$$

where $\boldsymbol{u}_k$ is the velocity of the fluid element of phase k, $\hat{\boldsymbol{n}}$ is the interface-normal vector, and the right-hand side is the interface's velocity normal to itself [9].

Equations (2.5) and (2.6) together respectively constrain the tangential and normal velocities in either phase around the interface. For immiscible, incompressible fluids, the Navier Stokes equations (2.2) apply for either phase, but are coupled together hydrodynamically by these boundary conditions at the interface [9].

2.2.1 Surface Tension

Immiscible fluids, such as oil and water, do not mix to form a single phase, and so coexist in separate phases at the interface. Spontaneous phase separation supposes that immiscible fluids minimize their free energy by remaining separate [6]. Conversely, attempting to mix immiscible fluids would raise this energy. Since the fundamental difference between this situation and some other pair of miscible fluids is the presence of the interface, these energy changes must be occurring at the deformable interface.

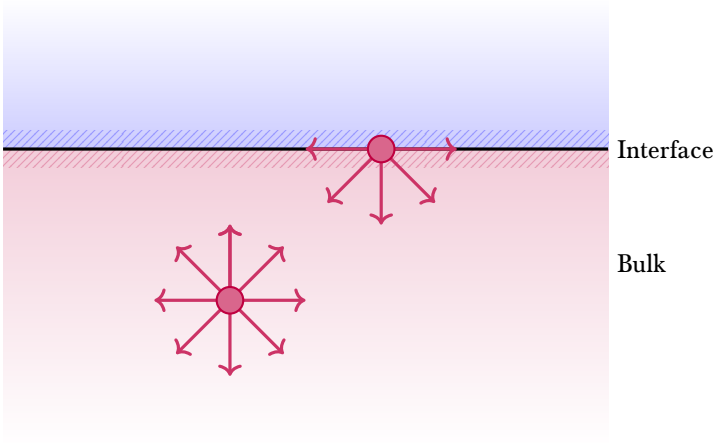

Figure 2.2: Intermolecular cohesive forces in the bulk and at the interface. In the bulk, molecules are surrounded and attracted by other molecules of their own kind. At the interface, they lose half of these interactions: there is an energy cost to reside there, and there exists a net force towards the bulk. Adapted from [5].

Molecules must attract one another to form a continuous fluid phase. Molecules also experience such *intermolecular forces* with molecules of different substances. Figure 2.2 shows how molecules in the bulk indeed experience more *cohesive* forces with molecules of their own substance than at the interface, where they lose half of these interactions, owing to the different nature of the molecules on the other side of the interface [5]. Molecules also experience *adhesive* forces with molecules of different species, but for immiscible fluids, these are weaker than the cohesive forces. The resulting tendency for molecules to be in the bulk implies an additional interface-normal pressure directed towards the bulk, and the tendency to minimize the surface-area of the interface.

Therefore, there exists an interfacial phenomenon for two fluids at equilibrium that:

- minimizes the system's free energy by maintaining an interface;

[2] Couette flow is essentially 1D, since velocity profiles only vary along y [9].

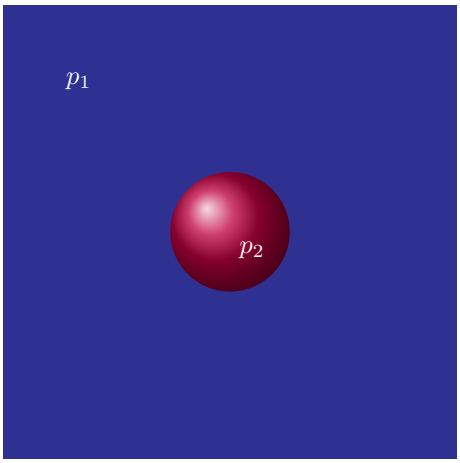

Figure 2.3: A spherical droplet of fluid "2" immersed in fluid "1". Its shape results from overpressure and minimization of surface area (and hence, surface energy) associated with surface tension. The pressure p_2 inside the droplet is larger than the pressure p_1 outside, due to surface tension.

- manifests itself with an interface-normal pressure jump.

Surface tension σ is indeed both

- the change of free energy F for a change in interface area A at constant temperature T, volume V, and amount of matter n [5]:

$$\sigma = \left[\frac{\partial F}{\partial A}\right]_{T,V,n} \tag{2.7}$$

- the scaling factor of the overpressure (or, *Laplace* pressure) Δp caused by local mean interface curvature $\bar{\kappa}$ [5, 9]:[3]

$$\Delta p = 2\sigma\bar{\kappa} \tag{2.9}$$

Equation (2.7) is the change in force required to deform a surface. Since work is force applied over a distance, we can also identify surface tension as the interface-normal force per unit length of interface required to deform the interface [5].

In figure 2.3, a volume of fluid "2" is immersed in fluid "1". Minimizing its surface area and the fluid-fluid interface, the volume adopts a spherical shape with radius R, and the mean curvature is $1/R$. The droplet's outward curvature indicates that the droplet is in state of overpressure, with pressure p_2:

$$p_2 = p_1 + \Delta p = p_1 + \sigma\frac{2}{R} \tag{2.10}$$

2.2.2 Wetting and Contact Angles

Surface tension also exists between a fluid and solid phase, and will manifest itself at three-phase boundaries between two fluids and a solid. Consider a drop of liquid in ambient gas, deposited on a flat solid surface. For the droplet to spread on the solid, it must:

1. deform its interface with the gas,

[3] The normal stress boundary condition is, more formally [9]:

$$\Delta p = -\sigma\nabla\cdot\hat{\boldsymbol{n}} \tag{2.8}$$

where $\hat{\boldsymbol{n}}$ is the unit-normal to the boundary's surface. Note this equation represents an additional interfacial boundary condition.

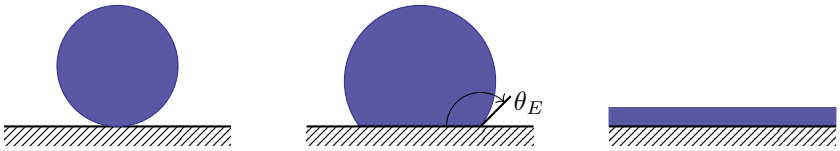

Figure 2.4: Liquid droplets deposited on a flat solid surface. On the left, a non-wetting droplet. In the middle, a partially wetting droplet. On the right, a fully wetting droplet would tend to form a film. The equilibrium of forces at the contact line defines the equilibrium contact angle θ_{E}.

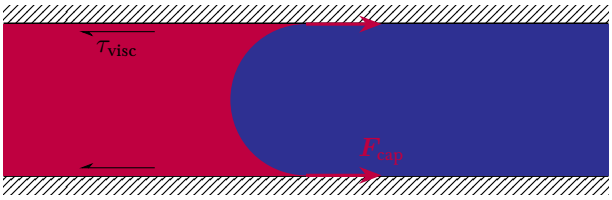

Figure 2.5: Capillary Intrusion in a Tube. The tube walls are wetting: capillary forces $\boldsymbol{F}_{\mathrm{cap}}$ drive the red fluid through the tube filled with blue fluid, while viscous stresses τ_{visc} oppose this movement. Viscous dissipation also happens at the meniscus and in the blue fluid, since it is displaced and must move.

2. increase its interface with the solid,
3. decrease the gas/solid interface.

These three processes are related respectively to the surface tensions:

1. between the two fluids σ_{LG},
2. between the liquid and the solid σ_{SL},
3. and between the gas and the solid σ_{SG}.

The work required for this spreading defines the *contact angle* θ_{E} formed by the three-phase contact line with the flat solid surface [5].

Figure 2.4 shows deposited droplets at equilibrium, where the balance of surface-tensile forces yields the equilibrium contact angle θ_{E}. The interface reduces to a line for three-phase contact. The surface-tensile forces between the fluids and the solid are aligned with the flat surface, and that between the two fluids is directed away from the solid surface at an angle θ_{E}. A simple force balance then yields *Young's law* [4, 5]:

$$\cos\theta_{\mathrm{E}} = \frac{\sigma_{\mathrm{SG}} - \sigma_{\mathrm{SL}}}{\sigma_{\mathrm{LG}}} \tag{2.11}$$

A less-wetting liquid will have a large equilibrium contact angle, and vice versa. A fully wetting droplet will tend to spread over the entire solid surface. *Capillary forces* associated with surface tension are stronger for small contact angles, and can drive fluid flow, as shown in figure 2.5.

The *dynamic contact angle* θ_{d} is the actual apparent contact angle away from static equilibrium. It is associated with a moving contact line overcoming viscous dissipation, and therefore is viscosity- and velocity-dependent. In addition, contact angle movement on the solid implies that the fluid does not obey no-slip at the microscopic scale, introducing dependence on a *slip length*, a microscopic material property [3, 5, 7].

2.3 Dimensionless Numbers

2.3.1 Principle

Taking equation (2.9) and normalizing all variables in terms of macroscopic characteristic values (e.g., a tube's diameter for characteristic length $\mathcal{L}$) yields a *non-dimensionalized* Navier-Stokes equation. The

viscous term becomes in terms of dimensionless velocity $\boldsymbol{u}^* = \boldsymbol{u}/\mathcal{U}$ (where $\mathcal{U}$ is the flow's characteristic velocity, e.g. domain inlet velocity) $\mathrm{Re}^{-1}\nabla^2\boldsymbol{u}^*$, where Re is the ***Reynolds number*** [9]:

$$\mathrm{Re} = \frac{\mathcal{U}\mathcal{L}}{\nu} \tag{2.12}$$

When Re is very large, the viscous term can then be neglected: momentum advection, represented by $\mathcal{U}\mathcal{L}$, is much more important than kinematic viscosity (or, momentum diffusion) ν. Dimensionless quantities like Re can be used to simplify equations by scaling out minor contributions. For an example, consider again the stratified flow in figure 2.1 and the boundary condition in equation (2.5). If the dimensionless ***viscosity ratio*** μ_1/μ_2 is very high, the boundary condition described by equation (2.5) can be simplified to a free-surface condition [9]:

$$\mu_1 \frac{\partial u_1}{\partial y}\bigg|_{\text{interface}} \approx 0 \tag{2.13}$$

Because physics should not depend on a particular set of units, dimensionless numbers can be used to express similar behavior across a wide range of physical scales [9]. For example, any liquid drop sitting on a partially wetting solid surface where the ambient gas density is negligible can be characterized by its Bond number Bo [5]:[4]

$$\mathrm{Bo} = \frac{\rho g V^{2/3}}{\sigma} \tag{2.14}$$

where ρ is the liquid's density, g is gravitational acceleration, V is the bubble's volume, and σ is the surface tension between the fluids. For a large Bo, gravity dominates and the droplet flattens, spreading despite surface tension opposing interface deformation. For a small Bo, surface tension dominates, gravity can be neglected, and the droplet adopts a spherical shape, sitting on the solid surface according to its equilibrium contact angle θ_{E}.

2.3.2 Inkjet Printing Parameter Space

Ink jetting in air supposes density ratios of $\lambda_\rho = \mathcal{O}(10^3)$ and kinematic viscosity ratios of $\lambda_\nu = \mathcal{O}(10^2)$ [4]. In piezoelectric drop-on-demand inkjet printing, droplet volumes are small, and so are Bond numbers: gravity can be neglected in considering droplet shapes [10]. As discussed in chapter 1, we are especially interested in the jetting of fluid particles through the nozzle. The pressure wave delivered by the piezoelectric element imparts inertial (kinetic) energy per unit volume to the fluid scaling with $\rho U^2 R^3$, where U is a characteristic ejection velocity for a droplet of characteristic length, or radius, R and density ρ. For the jet to pierce through the fluid-fluid interface at the meniscus, it must deform the interface with the surrounding gas, which is associated with an energy cost scaling with σR^2. The ratio of these energies gives the Weber number We:[5]

$$\mathrm{We} = \frac{\rho U^2 R}{\sigma} \tag{2.15}$$

If the inertial contribution is too weak, no droplet will be ejected [10].

With respect to fluid viscosity: on one hand, it damps the inertial force as described by the Reynolds number Re, which must then be large enough. Otherwise, all the energy from the pressure pulse is dissipated before reaching the nozzle. On the other hand, the required interface deformation also implies flow, and therefore viscous dissipation near the interface. The capillary number Ca represents this balance of viscous and inertial forces:

$$\mathrm{Ca} = \frac{\mu U}{\sigma} = \frac{\mathrm{We}}{\mathrm{Re}} \tag{2.16}$$

[4] The ambient gas density is neglected here, assuming that the dimensionless ratio between the liquid density and gas density is very large.

[5] These numbers are more typically defined in terms of *force* ratios, rather than energy ratios [10]. Either choice leads to the same scaling, though.

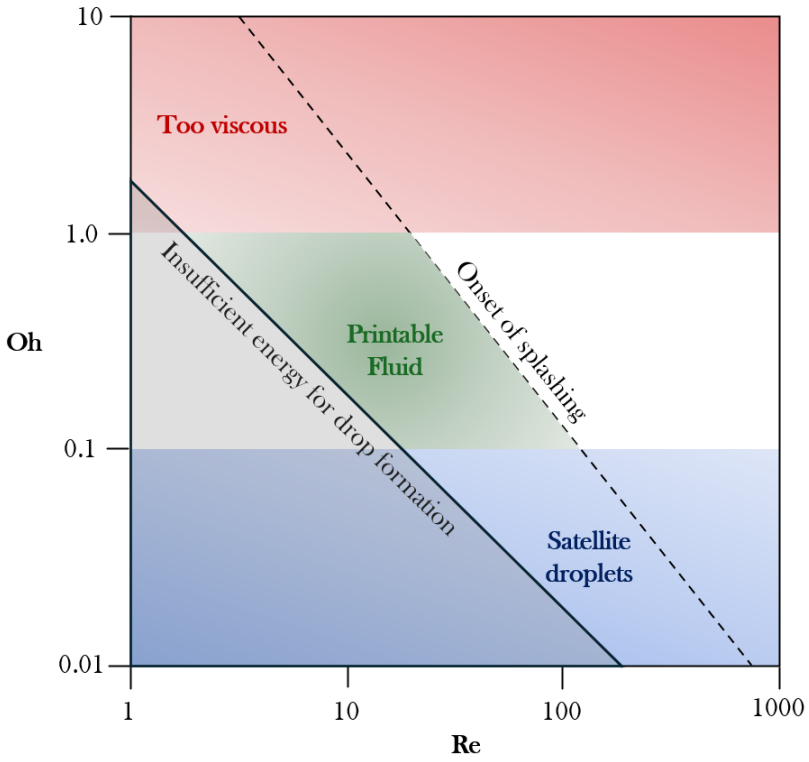

Figure 2.6: Dimensionless parameter map for "stable operation of drop-on-demand inkjet printing". Adapted from [10]

A similar scaling, but comparing viscous to capillary *timescales* yields the Ohnesorge number Oh [10]:[6]

$$\mathrm{Oh} = \frac{\mu}{\sqrt{\rho\sigma R}} = \frac{\mathrm{We}^{1/2}}{\mathrm{Re}} \tag{2.18}$$

If Oh is too large, then the meniscus will not deform due to viscous dissipation.

Figure 2.6 summarizes the requirements on dimensionless numbers for inkjet printing [10]. Low Re or Oh means that there is insufficient inertia to overcome viscous dissipation in the bulk, or the surface tension at the meniscus. If Oh is too large, too much energy is lost to viscous dissipation at the meniscus for jetting to occur. If Oh is too small, surface tension is so strong that larger droplets are unstable, and form smaller satellite droplets [2, 5, 10]. For large Re and smaller surface tensions (i.e., large Oh, owing to equations (2.15) and (2.18)), ejected droplets are susceptible to splash on the substrate, with is problematic for precise printing [10]. These factors together form a limited dimensionless parameter space in which drop-on-demand inkjet printing is possible.

The use of Lattice Boltzmann in the precursor work [4] and discussed in chapter 3 is rooted in the method's ability to simulate in this relevant parameter space:

- large fluid density and viscosity ratios,
- moderate Reynolds numbers corresponding to non-turbulent dynamic flow conditions with non-negligible viscous dissipation,

[6] Characteristic timescales of phenomena are found by forming a number with units of time from the essential fluid or flow properties associated with said phenomena. For viscous phenomena, one could use kinematic viscosity ν and any characteristic lengthscale $\mathcal{L}$:

$$t_{\text{viscous}} \sim \frac{\mathcal{L}^2}{\nu} \tag{2.17}$$

- moderate Ohnesorge numbers corresponding to non-negligible surface-tensile and capillary phenomena.

The last point implies that *wetting and contact-line dynamics should also be captured*, justifying the search for better wetting implementations.

Chapter 2 References

[1] Theodore L. Bergman et al. *Fundamentals of Heat and Mass Transfer*. 8th ed. 1 online resource (1045 pages) vols. New York: Wiley, 2017.

[2] Christopher E. Brennen. *Fundamentals of Multiphase Flow*. Cambridge University Press, 2005.

[3] Tak Shing Chan et al. "Cox–Voinov theory with slip". In: *Journal of Fluid Mechanics* 900 (2020). doi: 10.1017/jfm.2020.499.

[4] Karun Pravin Nirod Datadien. "Directional instabilities in microdroplet jetting: a numerical approach". PhD thesis. Applied Physics and Science Education, Jan. 31, 2024.

[5] Pierre-Gilles De Gennes, Françoise Brochard-Wyart, and David Quéré. *Capillarity and Wetting Phenomena*. New York, NY: Springer New York, 2004. doi: 10.1007/978-0-387-21656-0.

[6] Robert Holyst 1963- and Andrzej Poniewierski 1951-. *Thermodynamics for chemists, physicists and engineers*. 1 online resource : illustrations vols. Dordrecht: Springer, 2012.

[7] David Jacqmin. "Contact-line dynamics of a diffuse fluid interface". In: *Journal of Fluid Mechanics* 402 (2000). doi: 10.1017/S0022112099006874.

[8] Timm Krüger et al. *The Lattice Boltzmann Method: Principles and Practice*. Graduate Texts in Physics. Springer, 2016.

[9] Pijush K. Kundu et al. *Fluid Mechanics*. Sixth edition. Amsterdam: Elsevier/AP, 2016.

[10] D. Lohse. "Fundamental Fluid Dynamics Challenges in Inkjet Printing". In: *Annual Review of Fluid Mechanics* 54 (2021). doi: 10.1146/annurev-fluid-022321-114001.

[11] FTM Nieuwstadt, Bendiks Jan Boersma, and Jerry Westerweel. *Turbulence: Introduction to Theory and Applications of Turbulent Flows*. Springer, 2016. doi: 10.1007/978-3-319-31599-7.

Chapter 3 | Lattice Boltzmann Methods

Key Points

- The Boltzmann Equation (BE) describes the mesoscopic transport of particles populations, and has its roots in microscopic kinetic gas theory.
- The discretized BE, the Lattice Boltzmann Equation (LBE), can be broken down into simple local steps, and is as such naturally suited to parallelization.
- The Chapman-Enskog procedure provides a link between the mesoscopic scale description of the LBE and macroscopic scale Navier-Stokes fluid behavior.
- Central Moment Lattice Boltzmann formulations improve stability by resolving issues in Galilean invariance.
- Immiscible multiphase flows can be simulated with color-gradient methods.

This chapter describes the numerical method which will be used in the thesis, as a continuation of the work in [5]: a Central Moment, color-gradient Lattice Boltzmann Method for Immiscible Multiphase Flows. While certainly a mouthful, understanding the principle behind the technique is relatively straightforward. Starting from the origin of Lattice Boltzmann methods, we will clarify the technique's strengths and limitations, which will later better inform any choices relating to the implementation of wetting phenomena. Hurried readers already familiar with Lattice Boltzmann are invited to start at section 3.4.

3.1 Kinetic Gas Theory

3.1.1 The Particle Distribution Function and the Boltzmann Equation

Our starting point for Lattice Boltzmann Methods (LBM) is kinetic gas theory applied to dilute monoatomic gases. Our initial object of study is therefore a large collection of point particles. We introduce the *particle distribution function* $f(\boldsymbol{x}, \boldsymbol{\xi}, t)$ to describe the local proportion (or density) of particles at position $\boldsymbol{x}$ and time t with velocity $\boldsymbol{\xi}$ [15]. Particle distributions f also express the *probability* of particles occupying a certain velocity-state in space and time, describing *mesoscopic* population dynamics rather than microscopic particle (molecular) dynamics [25]. The group of particles represented through f is a *population*.

At the microscopic scale, Newton's laws describe each particles' motion between quasi-instantaneous binary collision events, the outcome of which are constrained by conservation of mass and momentum. The move to the mesoscopic scale averages the effects of collision events, lumping them together to affect a population f as a whole [25]. An expression for the evolution of $f(\boldsymbol{x}, \boldsymbol{\xi}, t)$ over time can be obtained by

taking a total time derivative, with the chain rule yielding, with index notation for vectors [15]:

$$\frac{df}{dt} = \frac{\partial f}{\partial t}\frac{dt}{dt} + \frac{\partial f}{\partial x_\alpha}\frac{dx_\alpha}{dt} + \frac{\partial f}{\partial \xi_\alpha}\frac{d\xi_\alpha}{dt} \tag{3.1}$$

Since the variations of f are due to collision events, we call the total derivative df/dt the ***collision operator*** $\Omega(f)$. The time-derivative of position x_α is velocity ξ_α, and as particle dynamics are described by Newton's laws, the time-derivative of velocity ξ_α is an acceleration which can be expressed as a local body force density F_α/ρ. In the absence of such a force, we recover the force-free ***Boltzmann equation*** (BE):

$$\boxed{\frac{\partial f}{\partial t} + \xi_\alpha \frac{\partial f}{\partial x_\alpha} = \Omega(f)} \tag{3.2}$$

The variations of f, and therefore the action of the collision operator Ω, must satisfy conservation of mass and momentum, the constraints to the microscopic collisions.

3.1.2 Moments of the Particle Distribution Function

The Boltzmann equation is also related to the ***macroscopic*** dynamics of the continuum gas formed by the microscopic particles. By integrating f over velocity space, we recover a local normalized particle count; in other words, the density ρ of the gas:

$$\int f d^3\xi = \rho \tag{3.3}$$

Integrating f in velocity space after multiplying it by the velocity n times corresponds to taking the n-th velocity ***moment*** of f, the zeroth moment then being mass density. Higher-order moments are related to other macroscopic quantities, with the first-order moment yielding momentum density [15]:

$$\int f \xi_\alpha d^3\xi = \rho u_\alpha \tag{3.4}$$

Taking the moments of the entire Boltzmann equation yields macroscopic scale conservation equations for mass and momentum [15].

3.1.3 Equilibrium Distributions and Collision Operators

At the microscopic scale, the particles in the system constantly travel and undergo elastic collisions across which no energy is dissipated, meaning that individual particles' velocity-states are constantly changing. At the mesoscopic scale however, a population of particles can reach an equilibrium state described by an ***equilibrium particle distribution function*** f^{eq}, which is also defined locally in space and time. It further depends on molecule velocities' deviations from mean (bulk fluid) velocity $\boldsymbol{u}$, which are associated with fluid temperature T [4, 15, 25].[1] An equilibrium distribution of particle velocity magnitudes is shown qualitatively in figure 3.1.

This implies that through the action of the collision operator $\Omega(f)$, a particle distribution f tends toward the equilibrium state f^{eq}. Were some spatially homogeneous particle distribution $f(\boldsymbol{\xi}, t=0)$ to relax to $f^{\text{eq}}(\boldsymbol{\xi})$ through exponential decay, we would have:

$$f(\boldsymbol{\xi}, t) = f^{\text{eq}}(\boldsymbol{\xi}) + \big(f(\boldsymbol{\xi}, t=0) - f^{\text{eq}}(\boldsymbol{\xi})\big)e^{-t/\tau} \tag{3.6}$$

where τ is a ***relaxation time***, a property of the mesoscopic ***gas*** formed by the microscopic particles. The consistency of equation (3.6) with the Boltzmann equation (3.2) leads to the definition of the ***BGK collision***

[1] In the force-free case, f^{eq} for a dilute monoatomic gas is [15]:

$$f^{\text{eq}}(\rho, \boldsymbol{u}, T, \boldsymbol{\xi}) = \frac{\rho}{(2\pi RT)^{d/2}} e^{-(\boldsymbol{\xi}-\boldsymbol{u})^2/(2RT)} \tag{3.5}$$

where d is the number of spatial dimensions, and $R = k_B/m$ is the gas constant expressed with the Boltzmann constant k_B and particle mass m.

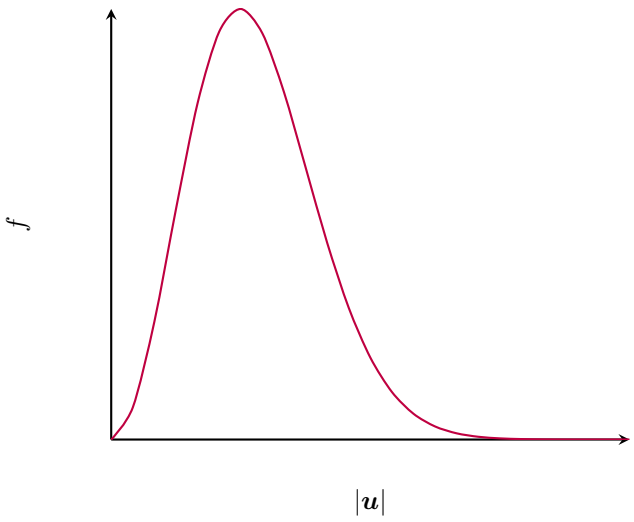

Figure 3.1: A typical equilibrium Maxwell Boltzmann distribution shape for velocity magnitude, towards which a population away from equilibrium tends to relax through collision events. Physically, population states relax to equilibrium distributions for each velocity *component*, not velocity magnitude.

operator [15]:[2]

$$\boxed{\Omega(f) = -\frac{1}{\tau}\left(f - f^{\text{eq}}\right)} \tag{3.7}$$

Together with the Boltzmann equation (3.2), the definition of the collision operator (which does not have to be the BGK) describes a system that can be discretized and solved numerically.

3.2 The Lattice Boltzmann Equation

3.2.1 Velocity, Space, and Time Discretization

Hermite Series Expansion

Owing to its form, the mesoscopic equilibrium f^{eq} (see equation (3.5) in footnote 1) can also be expressed with a Hermite series expansion. This procedure is not detailed here, although we note that the truncation of the expansion is clearly related to the conservation of moments: in our case, we are only interested in the first three orders, respectively related to conservation of mass, momentum, and energy. Following the non-dimensionalization of the Hermite-expanded equation truncated at the third order, we obtain using index notation [15]:

$$f^{\text{eq}}(\rho, \boldsymbol{u}, \theta, \boldsymbol{\xi}) \approx \omega(\boldsymbol{\xi})\rho\Big[1 + \xi_\alpha u_\alpha + (u_\alpha u_\beta + (\theta - 1)\delta_{\alpha\beta})(\xi_\alpha\xi_\beta - \delta_{\alpha\beta})\Big] \tag{3.8}$$

where θ is dimensionless temperature, $\delta_{\alpha\beta}$ is the Kronecker delta, and ω is a weight function of d the number of spatial dimensions, deviations from local velocity $\boldsymbol{\xi} - \boldsymbol{u}$, and θ.[3] Assuming an isothermal gas, $\theta = 1$. To finish the discretization, the Gauss-Hermite quadrature rule makes it possible to evaluate integrals of (3.8) (and in our case, the macroscopic moments of interest) *exactly* as sums of the integrand at points in velocity space called *abscissae*. Since we are only interested in reproducing the mesoscopic equilibrium distribution insofar as its moments recover mass, momentum, and energy conservation, this

[2] Named after Bhatnagar, Gross and Krook.

[3] The weight function is given by:

$$\omega = \frac{1}{(2\pi)^{d/2}} e^{-(\boldsymbol{\xi}-\boldsymbol{u})^2/(2\theta)} \tag{3.9}$$

means that the weights ω can be replaced with a set of q weights w_i related to Hermite polynomial values at the abscissae [15]. Since the abscissae are points in velocity space, this also means that we only need to consider a restricted set of q velocities $\boldsymbol{c}_i$ to recover the macroscopic moments, and that f^{eq} need only be known for each of these velocities indexed $i = 0, \ldots, (q-1)$. Velocity has been discretized, and we recover the ***discrete equilibrium distribution*** in index notation [15]:

$$f_i^{\text{eq}} = w_i \rho \left(1 + \frac{c_{i\alpha} u_\alpha}{c_s^2} + \frac{u_\alpha u_\beta (c_{i\alpha} c_{i_\beta} - c_s^2 \delta_{\alpha\beta})}{2 c_s^4} \right) \tag{3.10}$$

where c_s is the speed-of-sound, a constant related to the discrete velocity set as well as the equation of state for the gas at pressure $p = c_s^2 \rho$. The identical procedure of Hermite expansion and Gauss-Hermite quadrature can be applied to f, leading to the ***discrete-velocity Boltzmann equation*** [15]:

$$\frac{\partial f_i}{\partial t} + c_{i\alpha} \frac{\partial f_i}{\partial x_\alpha} = \Omega(f_i) \tag{3.11}$$

along all q directions in the velocity set.

Velocity Sets

Velocity sets of admissible particle velocities $\boldsymbol{c}_i$ arise naturally through the abscissae, and allow the computation of macroscopic moments.[4] Since the Hermite polynomial truncation and Gauss-Hermite quadrature are compatible with the conservation of mass and momentum inherited from the microscopic scale, the same moments are recovered at any f relaxing towards f^{eq}, except that the integrals of equations (3.3) and (3.4) are evaluated as discrete sums over the velocities $\boldsymbol{c}_i$ in the set:

$$\rho = \sum_i f_i = \sum_i f_i^{\text{eq}} \tag{3.13}$$

$$\rho \boldsymbol{u} = \sum_i f_i \boldsymbol{c}_i = \sum_i f_i^{\text{eq}} \boldsymbol{c}_i \tag{3.14}$$

Velocity sets are frequently denoted using DdQq notation, where d is still the number of spatial dimensions, and q is the number of discrete velocities. Figure 3.2 shows the velocity vectors in the D2Q9 velocity set, with vector weights:

$$w_i = \begin{cases} 4/9, & i = 0 \\ 1/9, & i = \{1,2,3,4\} \\ 1/36, & i = \{5,6,7,8\} \end{cases} \tag{3.15}$$

and lengths (in terms of discretized unit length Δx and timestep Δt):

$$|\boldsymbol{c}_i| = \begin{cases} 0, & i = 0 \\ 1, & i = \{1,2,3,4\} \\ \sqrt{2}, & i = \{5,6,7,8\} \end{cases} \tag{3.16}$$

The actual distances spanned by those velocities will depend on the spatial discretization. For all velocity sets used in this thesis, the lattice speed-of-sound is $c_s = 1/\sqrt{3}$ [15].

[4] Velocity sets can also be constructed by the satisfaction of isotropic conditions, which constrain the moments of the weights w_i in the set. Such conditions include, for example [15]:

$$\begin{gathered} \sum_i w_i = 1 \\ \sum_i w_i c_{i\alpha} = 0 \\ \sum_i w_i c_{i\alpha} c_{i\alpha} c_{i\beta} = c_s^2 \delta_{\alpha\beta} \end{gathered} \tag{3.12}$$

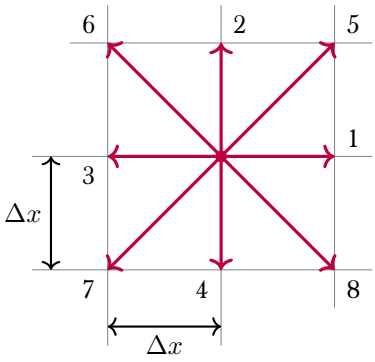

Figure 3.2: D2Q9 Velocity Set Diagram. The set is two-dimensional (D2) and contains nine (Q9) velocities, including the rest velocity indexed 0, which is a zero-vector. All velocities are vectors that end at the nodes of a uniform lattice.

Space and Time Discretization

Equation (3.11) is a first-order hyperbolic differential equation, for which the method of trajectories (or characteristics) and a simple single-point (or rectangular) discretization of a resultant time-integral of the collision operator Ω from 0 to timestep Δt yields [15]:

$$\boxed{f_i(\boldsymbol{x} + \boldsymbol{c}_i\Delta t, t + \Delta t) = f_i(\boldsymbol{x}, t) + \Delta t\Omega_i(\boldsymbol{x}, t)} \tag{3.17}$$

Space and time discretization are now clearly tied to the velocity sets: populations of particles represented by their distribution function f_i exist on *lattice nodes* at locations $\boldsymbol{x}$ in uniformly discretized space, and move once per timestep in the direction prescribed by their velocity $\boldsymbol{c}_i$ *exactly* to the location of another node.

3.2.2 Numerical Solution

Streaming and Collision

Equation (3.17) with the BGK operator in equation (3.7) yields the *lattice BGK equation* (LBGK):

$$f_i(\boldsymbol{x} + \boldsymbol{c}_i\Delta t, t + \Delta t) = f_i(\boldsymbol{x}, t) - \frac{\Delta t}{\tau}\Big(f_i(\boldsymbol{x}, t) - f_i^{\text{eq}}(\boldsymbol{x}, t)\Big) \tag{3.18}$$

The numerical solution of this equation is usually split into two separate and successive steps [15]:

- the *collision* step, where the precollision populations f_i at some lattice node $\boldsymbol{x}$ and time t relax towards equilibrium to become the post-collision populations: $f_i^\star$

$$f_i^\star(\boldsymbol{x}, t) = \left(1 - \frac{\Delta t}{\tau}\right) f_i(\boldsymbol{x}, t) + \frac{\Delta t}{\tau} f_i^{\text{eq}}(\boldsymbol{x}, t) \tag{3.19}$$

- the *streaming* step, where post collision populations move to the lattice node prescribed by their velocity $\boldsymbol{c}_i$:

$$f_i(\boldsymbol{x} + \boldsymbol{c}_i\Delta t, t + \Delta t) = f_i^\star(\boldsymbol{x}, t) \tag{3.20}$$

General Algorithm

Stepping equation (3.17) through time solves the mesoscopic behavior of our gas, and is connected to macroscopic quantities through velocity moments of f_i. Equations (3.19) and (3.20) display an extremely valuable characteristic of LBM: *the major steps occur entirely locally*, meaning the equations are naturally suited to parallelization. Information exchange between populations at a local site (and hence, between

populations streaming from different nodes in the system) occurs through the equilibrium population returned by equation (3.10), which requires the calculation of the macroscopic moments according to equations (3.13) and (3.14).

3.3 Modeling Hydrodynamic Behavior

3.3.1 Chapman-Enskog Analysis

While there is a connection to macroscopic scale quantities through the velocity moments of the populations, it remains that we are modeling the mesoscopic population dynamics of many idealized particles. Our interest in LBM, however, is its connection to fluid dynamics as described by the Navier-Stokes equations, and established by *Chapman-Enskog analysis*, the broad strokes of which are presented here following the derivation in [15].

Taylor Expansion

Introducing the following shorthand notation for spatial and temporal derivatives:

$$\frac{\partial}{\partial x_\alpha} = \partial_\alpha \qquad\qquad \frac{\partial}{\partial t} = \partial_t \tag{3.21}$$

and defining a total/material "lattice" derivative operator D_t [16, 24]:

$$D_t = \partial_t + c_{i\alpha}\partial_\alpha \tag{3.22}$$

and so, Taylor-expanding $f_i(\boldsymbol{x} + \boldsymbol{c}_i\Delta t, t + \Delta t)$ with D_t with respect to $f_i(\boldsymbol{x}, t)$ in equation (3.18), with $f_i = f_i(\boldsymbol{x}, t)$

$$\Delta t D_t f_i + \frac{1}{2}\Delta t^2 D_t^2 f_i + \mathcal{O}(\Delta t^3) = -\frac{\Delta t}{\tau}(f_i - f_i^{\text{eq}}) \tag{3.23}$$

truncating out the $\mathcal{O}(\Delta t^3)$ terms and subtracting from equation (3.23) itself operated by $(\Delta t/2)D_t$, also noting that the right-hand side of equation (3.23) has the *non-equilibrium contribution* to f_i, $f_i^{\text{neq}} = f_i - f_i^{\text{eq}}$, we obtain after reversing the substitutions of equation (3.22) [15]:

$$\Delta t(\partial_t + c_{i\alpha}\partial_\alpha)f_i = -\frac{\Delta t}{\tau}f_i^{\text{neq}} + \Delta t(\partial_t + c_{i\alpha}\partial_\alpha)\frac{\Delta t}{2\tau}f_i^{\text{neq}} \tag{3.24}$$

The Perturbation Expansion

Taking the first order moment of equation (3.24) will result in a momentum conservation equation, and the Euler equation when $f \approx f^{\text{eq}}$. This indicates that hydrodynamic behavior "beyond the Euler equation must be connected to the non-equilibrium part of f" [15]. Departures of f from equilibrium can be expressed as terms of orders of $\text{Kn} = l_{\text{mfp}}/\mathcal{L}$ (where l_{mfp} is the mean free path that microscopic particles travel between collisions, and $\mathcal{L}$ is the macroscopic lengthscale), and so up to the second order [15, 25]:

$$f_i = f_i^{\text{eq}} + \epsilon f_i^{(1)} + \epsilon^2 f_i^{(2)} + \dots \tag{3.25}$$

with $\epsilon = \text{Kn}$. This further leads in the differential operators applied to f [15, 25]:

$$\partial_\alpha = \epsilon\partial_\alpha^{(1)} \tag{3.26}$$

$$\partial_t = \epsilon\partial_t^{(1)} + \epsilon^2\partial_t^{(2)} \tag{3.27}$$

Recovering the Navier-Stokes Equations

By exanding terms in equation (3.24) with equations (3.25), (3.26), and (3.27), one finds two separate equations with terms of respectively order $\mathcal{O}(\epsilon)$ and $\mathcal{O}(\epsilon^2)$. By taking the velocity moments of these equations separately, we obtain $\mathcal{O}(\text{Kn})$ and $\mathcal{O}(\text{Kn}^2)$ "moment equations", with higher-order equations corresponding

to "corrections" to lower-order equations [15]. Combining these equations together, reversing the order expansions, recalling the ideal gas equation of state $p = c_s^2 \rho$, we obtain:

$$\partial_t \rho + \partial_\gamma (\rho u_\gamma) = 0 \tag{3.28}$$

$$\partial_t (\rho u_\alpha) + \partial_\beta (\rho u_\alpha u_\beta) = -\partial_\alpha p + \partial_\beta \left[\left(\rho c_s^2 (\tau - \Delta t/2) \right) (\partial_\beta u_\alpha + \partial_\alpha u_\beta) \right] \tag{3.29}$$

By comparing equation (3.29) with the Navier Stokes equation (2.2), we can establish a relationship between the real, physical kinematic viscosity ν and the relaxation time τ of our gas:

$$\boxed{\nu = c_s^2 \left(\tau - \frac{\Delta t}{2} \right)} \tag{3.30}$$

Once this substitution is made, an $\mathcal{O}(\boldsymbol{u}^3)$ term aside, we have an equation that is identical to the Navier Stokes equation. This means that the macroscopic behavior of the virtual gas with mesoscopic relaxation time τ is equivalent to that of a fluid described by the Navier Stokes equation with kinematic viscosity ν [15, 25].

Lattice Boltzmann Numerical Methods

Chapman-Enskog analysis shows that LBM is a numerical method to solve the Navier-Stokes equations (NSE), and so is based on the mesoscopic dynamics of *fictitious* microscopic particles, whose macroscopic behavior is *equivalent* to that of a fluid as described by the NSE. The fictitious micro- and mesoscopic physics do not have to reflect the actual micro- and mesoscopic physics of whatever composes the macroscopic scale fluid.[5] With respect to the hydrodynamics, "particles have no physical meaning", and only exist as momentum carriers to mimic macroscopic scale fluid dynamics [10]. The content of equilibrium distributions, the population distributions themselves, or collision operators can be adjusted to suit entirely mathematical considerations relating to a particular macroscopic transport equation that is known *a priori* [15, 25]. Relaxation time τ is strictly speaking only a numerical parameter, and equation (3.30) does not establish τ as an actual mesoscopic property of the real fluid with viscosity ν. Yet, the fictitious or approximate microscopic dynamics are apparently *sufficient* to explain to macroscopic dynamics at hand, and it remains that real physical macroscopic transport phenomena have their roots in real microscopic phenomena.

3.3.2 Accuracy and Stability

Accuracy

In section 3.2.1, the Hermite expansion of f^{eq} was truncated at the third term in order to *only* recover hydrodynamic moments from the equilibrium distribution, leading to an $\mathcal{O}(\boldsymbol{u}^3)$ modeling error term (where $\boldsymbol{u}$ is the mean flow velocity) in the recovered NSE (3.29), which limits the applicability of the presented LBM to low Mach number Ma regimes [15].

In section 3.3.1, the perturbation expansion and Chapman-Enskog analysis did not consider moment equations or expansions of the spatial derivative above $\mathcal{O}(\epsilon^2)$, effectively rendering the LBM a second-order accurate approximation in space of the NSE [15]. The scheme is also second-order accurate in time, as it can be shown that a (second-order) trapezoidal discretization that gave equation (3.17) leads to the very same LBE obtained by the single-point approximation used in section 3.2.1 [15].

Stability

For the BGK operator, both equations (3.6) and (3.30), for numerical stability as well as physical consistency, require that $\tau > \Delta t/2$. Therefore, a choice of collision operator determines stability conditions which can significantly restrict available parameter space [15].

[5] A tighter link is possible, and potentially desirable [25].

The choice of velocity set, through its connection to Hermite polynomials, also limits the number of independent conserved moments to the number of velocities in the set q. Many issues in stability are related to the presence of "*ghost modes*", the higher-order non-hydrodynamic moments beyond the first six (relating to mass, components of momentum and stress in 3D) [7, 15]. From this, it is already plain that larger velocity sets are required to capture relevant moments, and so larger velocity sets also add controllable degrees of freedom with respect to ghost moments, which can contribute to stability, as errors associated with these moments can grow especially when unaccounted for [15, 22, 25]. These issues can limit the applicability of LBM in some reference frames, or at high velocities or low viscosities, unless alternative implementations are used [15, 25].

3.3.3 Boundary Conditions

Boundary conditions to the NSE prescribe macroscopic variables at boundaries [16]. Since LBM is fundamentally a mesoscopic method, boundary conditions must be redefined at the population level. For periodicity between two boundaries for example, populations f_i streaming out of the domain at one boundary stream back into it at the other boundary according to their velocity $c_{i\alpha}$ [15]. Since there are more populations than hydrodynamic moments at a given node, enforcing macroscopic boundary conditions in LBM is a non-unique problem, meaning that several LBM boundary schemes can satisfy the same macroscopic boundary condition [15].

Bounce-Back Boundary Conditions

Macroscopic no-slip boundary conditions prescribe a fluid velocity, corresponding to the fluid's interaction with a solid wall [15, 16]. At the microscopic level, particles collide with the wall to exchange momentum. The reflection of a particle's wall-normal momentum corresponds to zero normal particle flux through the wall. If across a collision with the wall, the particle reverses its wall-tangential momentum, there is no relative transverse velocity between the particle and the wall. The combination of these two criteria (e.g., the particle being reflected back where it streamed from) is called ***bounce-back***, and correspond to a no-slip boundary condition [15].

At the mesoscopic population level, since admissible velocities are discretized in the velocity set, the boundary condition manifests itself as a redistribution of particles across populations.[6] Figure 3.3 shows how bounce-back boundary conditions are applied. The boundary nodes are located $\Delta x/2$ away from the flat immobile wall, which is aligned with the grid. During the streaming step, populations streaming towards the wall will return to boundary nodes according to the reflection described above. Numerically, this means that we are assigning particles streaming *away* from the wall based on the post-collision populations streaming *towards* the wall.[7] The bounce-back boundary condition for particles streaming away from a resting wall is then [15]:

$$f_{\bar{i}}(\boldsymbol{x}_\mathrm{b}, t + \Delta t) = f_i^\star(\boldsymbol{x}_\mathrm{b}, t) \tag{3.31}$$

where $f_{\bar{i}}$ is the population with velocity $\boldsymbol{c}_{\bar{i}} = -\boldsymbol{c}_i$, $\boldsymbol{x}_\mathrm{b}$ is the position of a boundary node, $t + \Delta t$ is the post-streaming time, and $f_i^\star(\boldsymbol{x}_\mathrm{b}, t)$ is the post-collision population with velocity $\boldsymbol{c}_i$ at the boundary node.

For a moving wall with velocity $\boldsymbol{u}_\mathrm{w}$, we add tangential corrections corresponding to the redistribution of particles across populations due to the wall's movement [15]:

$$f_{\bar{i}}(\boldsymbol{x}_\mathrm{b}, t + \Delta t) = f_i^\star(\boldsymbol{x}_\mathrm{b}, t) - 2 w_i \rho_\mathrm{w} \frac{\boldsymbol{c}_i \cdot \boldsymbol{u}_\mathrm{w}}{c_s^2} \tag{3.32}$$

where ρ_w is fluid density at the wall.[8]

[6] This is consistent with the fact that the particles are colliding with a wall: a collision operator Ω_i also redistributes particles across populations.

[7] Due to the reflection process, they are actually the same particles. Comfortingly, this satisfies conservation of mass and momentum, since microscopic particles are conserved.

[8] Wall density must be closed, for example with the constant density of an incompressible flow, a local volume-average, or a fixed density corresponding to a desired pressure. The simplest closure is to use the density of the node where the boundary condition is being applied.[15].

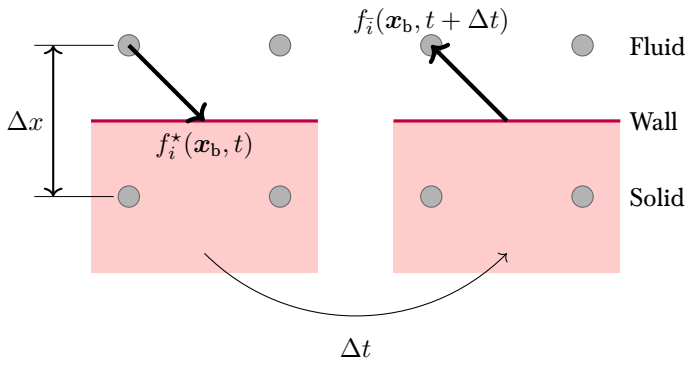

Figure 3.3: Bounce-Back Boundary Conditions. Bounce-Back boundary conditions are *link-wise* schemes, where the boundary nodes do not coincide with the location of the wall. Microscopic particles are conserved, because those streaming out the wall are those that previously streamed towards it. Adapted from [15].

3.3.4 Forcing Schemes

Forces are momentum-sources in the NSE, and therefore are microscopic particle sources in the LBE.[9] A *forcing scheme* introduces these sources at the mesoscopic level to recover the macroscopic force F_α, with Chapman-Enskog confirming the link between scales, while conserving mass and the momentum imparted by the force.

The discrete velocity Boltzmann equation (3.11) with a forcing term F_i is [15]:

$$\partial_t f_i + c_{i\alpha}\partial_\alpha f_i = \Omega_i + F_i \tag{3.33}$$

The forcing term F_i modifies particle momentum and hence the distribution of particles in populations f_i like the collision operator Ω_i, and so it comes as no surprise that F_i can be discretized much in the same way Ω_i was in section 3.2.1.[10] Indeed, the second-order truncation of the Hermite expansion of the forcing term F_i can be shown to be [15]:[11]

$$F_i = w_i\left(\frac{c_{i\alpha}}{c_s^2} + \frac{(c_{i\alpha}c_{i\beta} - c_s^2\delta_{\alpha\beta})u_\beta}{c_s^4}\right)F_\alpha \tag{3.34}$$

Following an algebraic redefinition of particle populations,[12] a second-order discretization similar to that done in section 3.2.1 with the BGK operator leads to:

$$\bar{f}_i(\boldsymbol{x} + \boldsymbol{c}_i\Delta, t+\Delta t) = \bar{f}_i - \frac{\Delta t}{\bar{\tau}}\left(\bar{f}_i(\boldsymbol{x}, t) - \bar{f}_i^{\mathrm{eq}}(\boldsymbol{x}, t)\right) + \left(1 - \frac{\Delta t}{2\bar{\tau}}\right)F_i\Delta t \tag{3.36}$$

where $\bar{\tau} = \tau + \Delta t/2$ is the new relaxation time, with the same relation to fluid kinematic viscosity as in equation (3.30). Chapman-Enskog analysis successfully recovers the NSE with a source term from equation (3.36)[15]. The formal modification of the populations and relaxation time are mathematical tricks to recover equations known *a priori*.[13] Equation (3.36) can then be treated numerically in exactly the

[9] When LBM is used as a Navier-Stokes solver, the microscopic particles have "no [necessary] physical meaning", and are only momentum carriers [10].

[10] The Hermite series expansion was used to find the equilibrium distribution f_i^{eq}, but recall that in the first place, f_i^{eq} is introduced by the BGK operator in equation (3.7).

[11] This arises from the expansion of the $\frac{F_\alpha}{\rho}\frac{f}{\xi_\alpha}$ term we originally omitted from the continuous Boltzmann equation in (3.1).

[12] The modified populations $\bar{f}_i$ are [15]:

$$\bar{f}_i = f_i - \frac{(\Omega_i + F_i)\Delta t}{2} \tag{3.35}$$

This redefinition is merely a mathematical trick to recover formally familiar equations.

[13] This is not troublesome, since we are approaching LBM merely as a numerical method to solve the NSE.

same way as equation (3.18), with the additional preliminary computation of the forcing term according to equation (3.34). Since forces are momentum sources, and so modify the moments corresponding to momentum, energy, etc., the addition of a forcing term and any change in variables (e.g. going from f_i to $\bar{f}_i$) will modify the computation of macroscopic moments. In the present case of ***Guo***-type forcing, the first-order moment in velocity of $\bar{f}_i$ (i.e. momentum) used to compute velocity is changed to[11, 15]:

$$\rho \boldsymbol{u} = \sum_i \bar{f}_i \boldsymbol{c}_i + \frac{\Delta t}{2} \sum_i F_i \boldsymbol{c}_{i\alpha} \tag{3.37}$$

3.4 Central Moments LBM

The precursor work [5] to this literature review resolves stability issues by the implementation of a ***central moments*** (CM) LBM as described in [7]. CM-LBM addresses the short-wavelength/high-frequency content of non-hydrodynamic ghost modes associated with the $\mathcal{O}(\boldsymbol{u}^3)$ error-term of section 3.3.2 [15, 22]. We did not initally discuss this error term with stability in mind, but since it introduces velocity-dependence in the results (and by extension, in the transport properties of the fluid [15]), it indeed leads to violation of Galilean invariance. The truncation ignores higher-order ghost moments for which Galilean invariance is now no longer guaranteed, translating as a stability issue.

3.4.1 Moment-Space Relaxation

In section 3.1, we introduced collision operators Ω as relaxing populations towards equilibrium. This relaxation redistributes particles across velocities $c_{i\alpha}$, which means that Ω effectively changes the momentum- or energy-state of particles, which are macroscopic moments: this implies that relaxation can also occur in ***moment-space***.

Indeed, it is possible to map populations f_i to moment-space m_k:

$$m_k = \sum_i M_{ki} f_i \tag{3.38}$$

where M_{ki} is a transformation matrix, adding populations to retrieve moments.[14] Note that equation (3.38) can also be applied to equilibrium distributions to find corresponding equilibrium moments $m_k^{\text{eq.}}$: relaxation during the collision step can now occur in moment-space. Using the BGK operator, we cannot distinguish between the relaxation of momentum or energy states, despite the fact that they correspond to different moments, since populations are relaxed directly. Following the transformation of equation (3.38), it is now possible to relax different moments m_k to post collision moments $m_k^\star$ at different rates ω_k, including the troublesome ghosts of section 3.3.2, enhancing stability [15, 25]:

$$m_k^\star = m_k + \omega_k \left(m_k - m_k^{\text{eq}} \right) \Delta t \tag{3.39}$$

before transforming back into population space. Only the macroscopic moments (which survive the Chapman-Enskog procedure to establish a link with kinematic viscosity ν) require $\omega_k = 1/\tau$ [7, 15].

3.4.2 Central Moments

The transformation matrix M_{ki} in equation (3.38) varies from method to method, and so there is significant freedom in defining which moments are being relaxed [15, 25]. The Galilean invariance of the flow implies the relaxation of similarly Galilean invariant moments: to break the dependence on the reference frame, CM-LBM relaxes ***central moments*** obtained by shifting lattice speeds $c_{i\alpha}$ by local fluid velocity u_α [10], producing a new set of velocities $\bar{c}_{i\alpha}$ used to calculate moments:

$$\bar{c}_{i\alpha} = c_{i\alpha} - u_\alpha \tag{3.40}$$

Local central moments and equilibrium central moments are obtained with equation (3.38), using the shifted velocities $\bar{c}_{i\alpha}$ in matrix M_{ki}. If the full set of q Hermite polynomials for a DdQq velocity set is used

[14] For example, summing all populations together (with a row of 1's in the martix M_{ki}) yields the zeroth-order moment, density ρ.

to define the equilibrium populations f_i^{eq}, most central equilibrium moments are actually null, and none depend on local fluid velocity $\boldsymbol{u}$ (they only depend on local density): they are Galilean invariant [9]. Using that full set for the equilibrium populations f_i^{eq} is actually done in certain CM-LBM implementations, since the resulting annihilation of most central moments can dramatically reduce computational overhead [8].[15]

Recall from section 3.3.4 that forces are momentum sources, and are therefore fundamentally similar to collision/relaxation at the mesoscopic level, as both phenomena redistribute momentum while conserving mass. Therefore, we can also treat forcing terms using central moments: again, using the full set of Hermite polynomials, we only find velocity-independent contributions to the post-collision and post-forcing populations [8].

3.5 Color-Gradient Multiphase Simulations

Among the many ways of simulating multiphase flows using LBM [14], we restrict ourselves to *color-gradient* (CG) methods as we continue previous work in [5]. Other methods are very briefly discussed in the literature in chapter 4. The method typically models two immiscible fluid phases with no phase change: the situation is characterized by interface-normal surface tension σ which opposes the deformation of fluid-fluid interfaces, leading to interface-normal pressure jumps proportional to σ and the interface's curvature [6].

The *color* in CG-LGM refers to either fluid: for example, a "red" fluid $l = r$ and a "blue" fluid $l = b$, each with their own single-phase reference densities ρ_l^0, leading to a density ratio $\lambda_\rho = \rho_r^0/\rho_b^0$. Locally, we distinguish between populations f_i^l of either fluid, leading to the density of fluid l:

$$\rho_l = \sum_i f_i^l \tag{3.41}$$

with total fluid density $\rho = \sum_k \rho_k$. To distinguish between phases in space, a phase-field indicator ρ^N is introduced [5]:[16]:

$$\rho^N = \frac{\rho_r - \rho_b}{\rho_r + \rho_b} \tag{3.42}$$

where $\rho^N = 1$ corresponds to pure red fluid, and $\rho^N = -1$ to pure blue fluid. A transition from one phase to another then manifests itself as variations and sign reversals of the phase-field ρ^N. This transition occurs over several lattice nodes, but actually models the presence of a sharp interface located where $\rho^N = 0$ [5, 19, 20]. Indeed, the diffusive nature of the interface in CG-LBM is entirely "auxiliary" to the implementation, especially enhancing stability and accuracy [17, 24].

3.5.1 Changes to Equilibrium and the Collision Step

The pressure p_l in each fluid l is calculated with:

$$p_l = \rho_l (c_s^l)^2 = \rho_l \frac{1 - \alpha_l}{2} \tag{3.43}$$

which introduces the parameter α_l, which defines the speed-of-sound c_s^l in the fluid l. It also appears in the modified rest (i.e. velocity-independent) component of the equilibrium distribution function $f_i^{l,\text{eq}}$ of fluid l through a term ϕ_i^l, which is linear in α_l. The effective equilibrium $f_i^{l,\text{eq}}$ towards which each fluid relaxes is now [5, 7, 21]:

$$f_i^{l,\text{eq}} = \rho_l \left[\phi_i^l + w_i \left(\frac{c_{i\alpha} u_\alpha}{c_s^2} + \frac{u_\alpha u_\beta (c_{i\alpha} c_{i_\beta} - c_s^2 \delta_{\alpha\beta})}{2 c_s^4} \right) \right] \tag{3.44}$$

[15] Strategic choices in truncation (and lack of correction) can also be made, since many higher-order central (ghost) moments may not harm the solution of a particular flow [7, 10].

[16] The densities can also be normalized by their reference state ρ_l^0 to avoid over-weighting the denser fluid for larger density ratios λ_ρ [1, 5]

where the parameter ϕ_i^l is defined for each velocity $\boldsymbol{c}_i$, like the weights w_i.[17] Note that all fluids share the same local macroscopic velocity, which is computed with the first velocity moment with respect to ***total*** density [18, 21]:

$$\rho u_\alpha = \sum_i \sum_l f_i^l c_{i\alpha} \tag{3.46}$$

This common velocity is how CG-LBM accomplishes hydrodynamic coupling: fluids are tied together by their first-and-above-order velocity moments, which include momentum and energy.

The redefined equilibrium in equation (3.44) injects the ideal gas equations of state (3.43) in the LBM algorithm, and therefore the density ratio λ_ρ: a Chapman-Enskog analysis returns the correct NSE for each fluid [21]. Equation (3.44) is for a second-order truncation of terms in the equilibrium distribution: in CM-LBM, higher-order terms may of course be retained. A single local value of relaxation time τ_{eff} (along with its corresponding relaxation rate ω_{eff} and kinematic viscosity ν_{eff}), typically interpolated from local fluids' pure-fluid values, is used to relax all fluid populations to their respective equilibria, with the collision operator $\Omega_i^{l(1)}$ for fluid l, yielding its post-collision populations $f_i^{l\star}$:

$$f_i^{l\star} = \Omega_i^{l(1)}(f_i^l) = \left(1 - \frac{\Delta t}{\tau_{\text{eff}}}\right) f_i^l + \frac{\Delta t}{\tau_{\text{eff}}} f_i^{l,\text{eq}} \tag{3.47}$$

In CM-LBM, the collision operator $\Omega_i^{l(1)}$ relaxes local central moments for each fluid to the equilibrium central moments to yield the post-collision populations $f_i^{l\star}$ [8].

Extended Equilibrium

The $\mathcal{O}(\boldsymbol{u}^3)$ term from section 3.3.2 also contains density gradients which are significant even at low Ma in multiphase simulations with non-unity density ratios λ_ρ [13, 17]. In this case, ***extended equilibrium*** (also called enhanced equilibrium) terms are injected to remove the error on purely mathematical grounds [5, 19, 20]. These terms Φ_i^l are added to the fluid equilibria $f_i^{l,\text{eq}}$ in equation 3.44, and can be expressed as [5]:

$$\Phi_i^l = \nu_{\text{eff}} \left[\psi_i (\boldsymbol{u} \cdot \nabla \rho_l) + \xi_i (\boldsymbol{G}_l : \boldsymbol{c}_i \otimes \boldsymbol{c}_i)\right] \tag{3.48}$$

$$\boldsymbol{G}_l = (\boldsymbol{u} \otimes \nabla \rho_l) + (\boldsymbol{u} \otimes \nabla \rho_l)^\top \tag{3.49}$$

where ψ_i and ξ_i are direction-dependent scalars.[18]

3.5.2 Perturbation and Recoloring

CG-LBM adds two additional steps in the algorithm, which are sequentially applied [7, 19, 21]:

- the ***perturbation*** step with operator $\Omega_i^{l,(2)}$, which generates interfacial tension in each phase to yield post-perturbation populations $f_i^{l\star\star}$ by generating a "volume-distributed interfacial force":

$$\boxed{f_i^{l\star\star} = \Omega_i^{l,(2)}(f_i^{l\star}) = f_i^{l\star} + \frac{A}{2} |\nabla \rho^N| \left[w_i \frac{(\boldsymbol{c}_i \cdot \nabla \rho^N)^2}{|\nabla \rho^N|^2} - B_i \right]} \tag{3.50}$$

  using a single spatially-varying parameter to inject a desired surface tension σ:

$$A = \frac{9}{4} \sigma / \tau_{\text{eff}} \tag{3.51}$$

[17] For the D2Q9 lattice, one may obtain:

$$\phi_i^l = \begin{cases} (1 + 5\alpha_l)/6, & i = 0 \\ (1 - \alpha_l)/6, & i = \{1, 2, 3, 4\} \\ (1 - \alpha_l)/24, & i = \{5, 6, 7, 8\} \end{cases} \tag{3.45}$$

This results from the down-projection of a D3Q19 scheme in [21] to D2Q9, according to a procedure outlined in [15].

[18] The full terms are given in the reference.

where B_i is defined for each velocity $\boldsymbol{c}_i$ in the set,[19] and $\nabla\rho^N$ is gradient of the phase-field ρ^N (the *color-gradient*).

The perturbation step generates interfacial tension by modifying the populations near the interface. For the implementation in [5], rooted in [21], Chapman-Enskog is used to find equation (3.50) by enforcing the consistency of the perturbation operator $\Omega_i^{(2)}$ with an interfacial force at the NSE level, locating a normal pressure jump across the interface defined by ρ^N. The perturbation step and the generation of interfacial tension ***does not*** keep phases separate on either side of the interface, however.

- the *recoloring* step with operator $\Omega_i^{l,(3)}$ which enforces immiscibility by redistributing fluid l particles in the post-perturbation populations $f_i^{l\star\star}$ into their fluid's phase while conserving mass and momentum, leading to the post-recoloring populations $f_i^{l\star\star\star}$ for each color:

$$\boxed{f_i^{l\star\star\star} = \Omega_i^{l,(3)}(f_i^{l\star\star}) = \begin{cases} \frac{\rho_r}{\rho} f_i^{\star\star} + \beta \frac{\rho_r \rho_b}{\rho^2} \cos(\varphi_i) f_i^{\text{eq}}|_{\boldsymbol{u}=\boldsymbol{0}}, & l = r \\ \frac{\rho_b}{\rho} f_i^{\star\star} - \beta \frac{\rho_r \rho_b}{\rho^2} \cos(\varphi_i) f_i^{\text{eq}}|_{\boldsymbol{u}=\boldsymbol{0}}, & l = b \end{cases}} \tag{3.53}$$

where $f_i^{\star\star} = \sum_l f_i^{l\star\star}$ is total post-perturbation population, β is a parameter related to the thickness of the auxiliary interface,[20] $f_i^{\text{eq}}|_{\boldsymbol{u}=\boldsymbol{0}} = \sum_l f_i^{l,\text{eq}}|_{\boldsymbol{u}=\boldsymbol{0}}$ is the total equilibrium population at null velocity, and φ_i is the angle between the color-gradient and a velocity $\boldsymbol{c}_i$, with:

$$\cos(\varphi_i) = \frac{\boldsymbol{c}_i \cdot \nabla\rho^N}{|\boldsymbol{c}_i||\nabla\rho^N|} \tag{3.54}$$

For either step, gradients are usually computed with isotropic gradient operators to preserve Galilean invariance, which are central finite-differences with all directions $\boldsymbol{c}_i$ in the velocity set weighted by w_i, for example for some scalar-valued function g [1, 5, 19]:

$$\nabla g(\boldsymbol{x}) = \frac{1}{c_s^2} \sum_i w_i g(\boldsymbol{x} + \boldsymbol{c}_i) c_{i\alpha} \tag{3.55}$$

3.5.3 Model Characteristics

Figure 3.4 shows the result of a CG-LBM simulation with density ratio $\lambda_\rho = 1\,000$. The pressure jump associated with surface tension manifests itself with the droplet's spherical shape, corresponding to a state of overpressure throughout the droplet. The precursor work [5] demonstrated that CG-LBM unlocked the parameter space required for inkjet printing simulations, namely a density ratio $\lambda_\rho = \mathcal{O}(10^3)$, with stabilizing central-moments implementations with enhanced equilibria. CG-LBM also allows to define viscous relaxation time τ independently from surface tension σ, which further facilitates parameter access and selection. Unlike other models, CG-LBM does not allow phase change (i.e. mass transfer across phases), which although limiting its use to immiscible fluids at timescales precluding evaporation, saves it from purely numerical phase change which can dissipate smaller droplets and features [5, 21].

Multiphase LBM is typically affected by ***spurious velocities*** near the interface, which are associated with lack of Galilean invariance and instability, and interface disintegration: CG-LBM with central-moments or enhanced equilibria, as well as isotropic gradient operators can keep those in check [5, 21, 24, 26]. Figure 3.5 shows velocity magnitudes for the droplet in figure 3.4: for this steady-state rest case, this entire field is due to spurious velocities. The latter occur along CG-LBM interfaces. Note that their magnitudes are smaller when the interface normal (and hence, the color-gradient) tends to align with the directions in the

[19] For example for D2Q9:

$$B_i = \begin{cases} -2/9, & i = 0 \\ 1/9, & i = \{1,2,3,4\} \\ 1/36, & i = \{5,6,7,8\} \end{cases} \tag{3.52}$$

This results from down-projection as indicated for ϕ_i^l.

[20] $0 < \beta < 1$, although $\beta < 1/\sqrt{2}$ is required for stability [12].

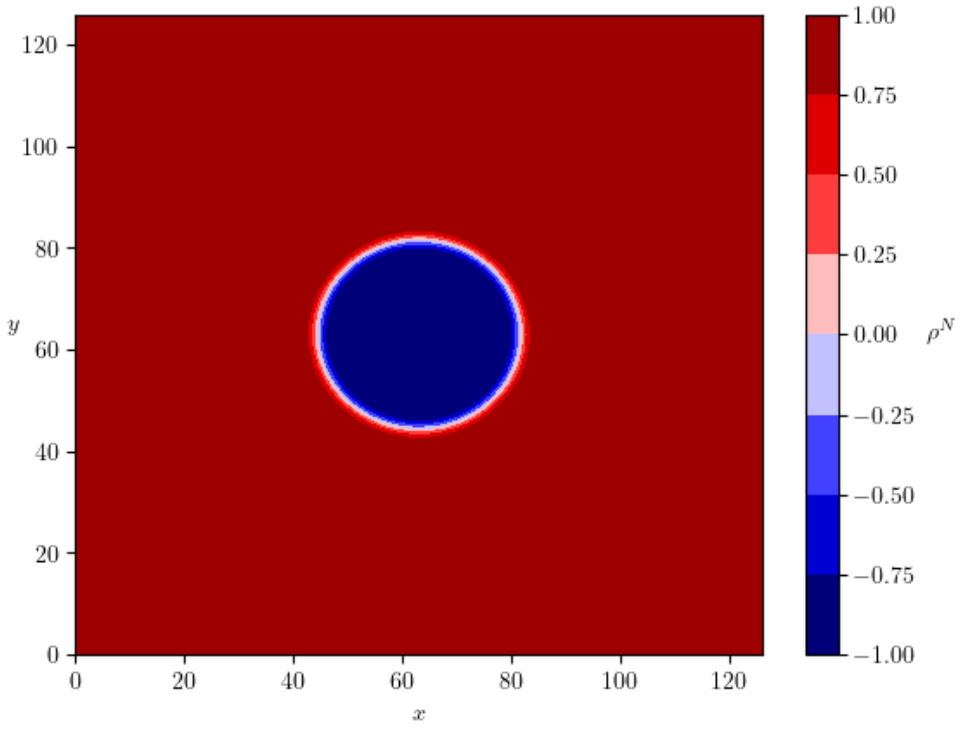

Figure 3.4: phase-field for a light blue droplet in heavy red medium in a converged CG-LBM simulation. The density ratio is $\lambda_\rho = 1\,000$, and the input surface tension is $\sigma = 0.1$. The radius of the circle fitted to the $\rho^N = 0$ contour corresponds to droplet radius and interface curvature, and using the pressure jump on either side of the interface where $|\rho^N| \to 1$, we can compute an effective in-simulation surface tension within 0.88% of the input value.

D2Q9 velocity set being used. The spurious velocity field hence depends on one's frame of reference, and is related to lack of Galilean invariance.

Using a Taylor series expansion, it can be shown that CG-LBM is, with respect to the interface itself, equivalent to an interface-tracking Allen-Cahn equation: this means that CG-LBM *implictly* tracks the interface [24]. Lower β parameters in the recoloring operator $\Omega_i^{(3)}$ lead to broader interfaces and more accuracy in evaluating the color-gradients $\nabla\rho^N$. That being said, the diffuse nature of the interface also adds an unphysical lengthscale to the simulation, which when of the order of actual flow features (e.g. droplet diameter) may interfere with results [24]. Figure 3.6 shows a planar interface maintained by the segregation operator. Analysis of the segregation operator and the equivalent Allen-Cahn system reveals a $\tanh$ phase-field transition across the interface [3, 23]. The analytical profile for a planar interface at rest and centered about $x = 0$, with the blue phase ($\rho^N < 0$) located at $x < 0$ is [12]:

$$\rho^N(x) = \tanh(\beta x) \tag{3.56}$$

where x is expressed in lattice units, and β is the segregation parameter used in the recoloring operator in equation (3.53).

3.6 Conclusions

LBM originates as a mesoscopic simulation tool, resolving the dynamics of large populations of molecule-like particles [25]. While its use to solve the NSE does not require flow-accurate mesoscopic or microscopic dynamics (the correct behavior arising at the macroscopic scale of interest), this connection to microscopic

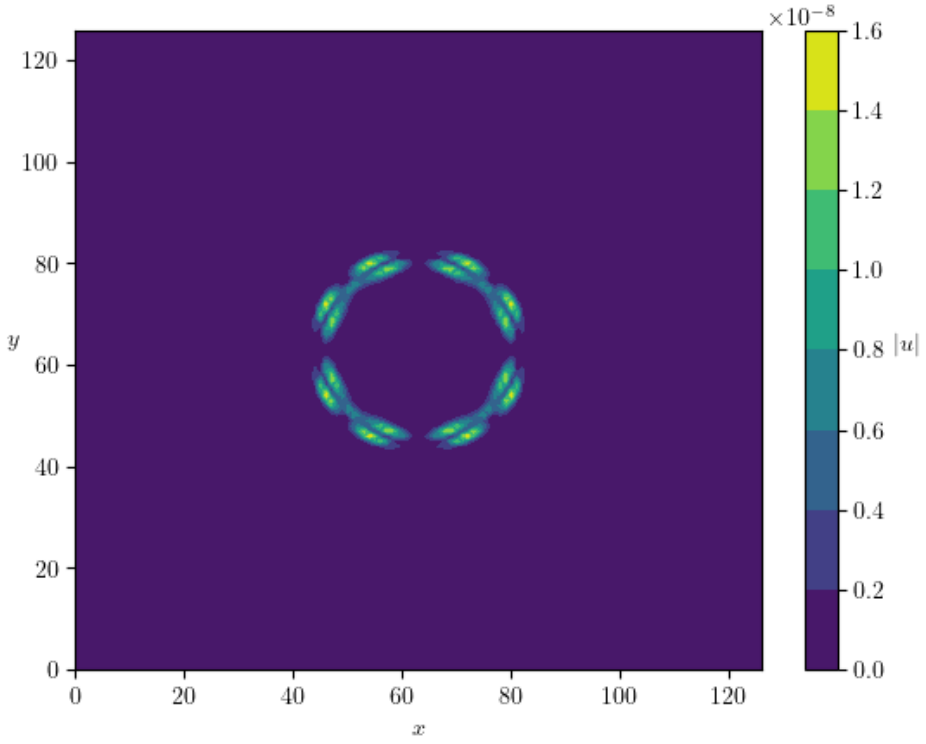

Figure 3.5: Velocity Magnitude Field for the droplet in figure 3.4. The magnitude of these spurious velocities is small. Note that a geometrical pattern arises, aligned with the D2Q9 velocity set in use: spurious velocities are related to a lack of Galilean invariance.

behavior is central to formulating even the simplest boundary conditions [15], where *particle/population*-boundary interactions are set, rather than at the macroscopic scale like in traditional CFD [16]. This connection is also *valuable* when expanding models to macroscopic phenomena strongly linked to the microscopic scale, such as surface tension and wetting originating from intermolecular forces [21]. Therefore, we will try to judge wetting schemes in relation to the microscopic interactions they imply.

Enforced macroscopic scale or micro/mesoscopic-scale-emergent behavior can be verified using Chapman-Enskog analysis [15], especially when the micro/mesoscopic connection was not the explicit starting point of an LBM extension, such as with CG-LBM.[21] Consequently, we will also consider wetting schemes by carefully analyzing their macroscopic content.

Extended equilibria arise essentially from mathematical considerations. Indeed, LBM stability is very much tied to Galilean invariance, and the presence of error terms which become problematic at certain regimes. We will leverage the advantages of CM-LBM and extended equilibria, which will allow us to investigate a wide range of density and viscosity ratios in multiphase simulations. It will be important, however, to temper claims by clearly identifying simulation regimes. For example, a CG-LBM implementation giving excellent results for static bubbles with non-unity density ratios can fail spectacularly for layered Poiseuille flow [19]. From a mathematical point of view as well, we will avoid harming LBM's locality.

[21]We note that *a posteriori* particle interactions were found to lead to an earlier form of CG-LBM, which indeed is usually designed to enforce known macroscopic behavior [2].

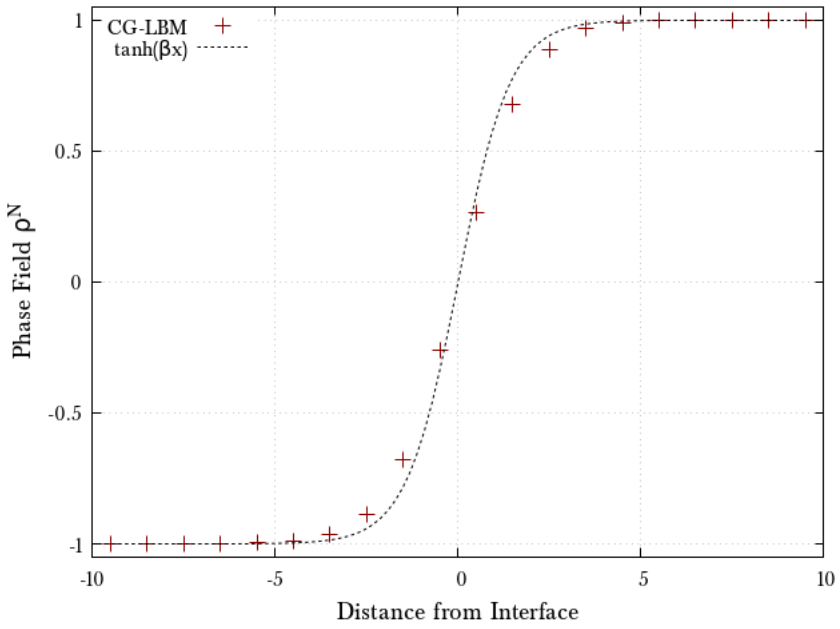

Figure 3.6: CG-LBM phase-field transition at the interface, with red phase to the left of the interface, blue phase to the right. At nodes close to the interface $\rho^N = 0$, both fluids exist in different proportions: the interface is diffuse. The segregation operator maintains $\tanh$ phase-field profiles according to the equation 3.56. The thickness of the interface is controlled by the segregation parameter β.

Chapter 3 References

[1] Yan Ba et al. "Multiple-relaxation-time color-gradient lattice Boltzmann model for simulating two-phase flows with high density ratio". In: *Phys. Rev. E* 94.2 (Aug. 2016). doi: 10.1103/PhysRevE.94.023310.

[2] Bruce M. Boghosian and Peter V. Coveney. "A particulate basis for an immiscible lattice-gas model". In: *Computer Physics Communications* 129.1 (July 2000). doi: 10.1016/s0010-4655(00)00091-6.

[3] K. Burgin et al. "Kinematics of chromodynamic multicomponent lattice Boltzmann simulation with a large density contrast". In: *Phys. Rev. E* 100.4 (Oct. 2019). doi: 10.1103/PhysRevE.100.043310.

[4] Carlo Cercignani. *The Boltzmann equation and its applications.* Applied mathematical sciences (Springer-Verlag New York Inc.); v. 67. New York: Springer-Verlag, 1988.

[5] Karun Pravin Nirod Datadien. "Directional instabilities in microdroplet jetting: a numerical approach". PhD thesis. Applied Physics and Science Education, Jan. 31, 2024.

[6] Pierre-Gilles De Gennes, Françoise Brochard-Wyart, and David Quéré. *Capillarity and Wetting Phenomena.* New York, NY: Springer New York, 2004. doi: 10.1007/978-0-387-21656-0.

[7] Alessandro De Rosis and Christophe Coreixas. "Multiphysics flow simulations using D3Q19 lattice Boltzmann methods based on central moments". In: *Physics of Fluids* 32.11 (Nov. 2020). doi: 10.1063/5.0026316.

[8] Alessandro De Rosis, Rongzong Huang, and Christophe Coreixas. "Universal formulation of central-moments-based lattice Boltzmann method with external forcing for the simulation of multiphysics phenomena". In: *Physics of Fluids* 31.11 (Nov. 2019). doi: 10.1063/1.5124719.

[9] Alessandro De Rosis and Kai H. Luo. "Role of higher-order Hermite polynomials in the central-moments-based lattice Boltzmann framework". In: *Phys. Rev. E* 99.1 (Jan. 2019). doi: 10.1103/PhysRevE.99.013301.

[10] Martin Geier, Andreas Greiner, and Jan G. Korvink. "Cascaded digital lattice Boltzmann automata for high Reynolds number flow". In: *Phys. Rev. E* 73.6 (June 2006). doi: 10.1103/PhysRevE.73.066705.

[11] Zhaoli Guo and T. S. Zhao. "Lattice Boltzmann model for incompressible flows through porous media". In: *Phys. Rev. E* 66.3 (Sept. 2002). doi: 10.1103/PhysRevE.66.036304.

[12] I. Halliday, A. P. Hollis, and C. M. Care. "Lattice Boltzmann algorithm for continuum multicomponent flow". In: *Phys. Rev. E* 76.2 (Aug. 2007). doi: 10.1103/PhysRevE.76.026708.

[13] D.J. Holdych et al. "An improved hydrodynamics formulation for multiphase flow lattice-boltzmann models". In: *International Journal of Modern Physics C* 9.8 (1998). doi: 10.1142/S0129183198001266.

[14] Haibo Huang, Michael C. Sukop, and Xi-Yun Lu. *Multiphase Lattice Boltzmann Methods: Theory and Application.* Wiley, July 2015. doi: 10.1002/9781118971451.

[15] Timm Krüger et al. *The Lattice Boltzmann Method: Principles and Practice.* Graduate Texts in Physics. Springer, 2016.

[16] Pijush K. Kundu et al. *Fluid Mechanics.* Sixth edition. Amsterdam: Elsevier/AP, 2016.

[17] Sébastien Leclaire, Marcelo Reggio, and Jean-Yves Trépanier. "Numerical evaluation of two recoloring operators for an immiscible two-phase flow lattice Boltzmann model". In: *Applied Mathematical Modelling* 36.5 (2012). doi: https://doi.org/10.1016/j.apm.2011.08.027.

[18] Sébastien Leclaire, Marcelo Reggio, and Jean-Yves Trépanier. "Progress and investigation on lattice Boltzmann modeling of multiple immiscible fluids or components with variable density and viscosity ratios". In: *Journal of Computational Physics* 246 (2013). doi: https://doi.org/10.1016/j.jcp.2013.03.039.

[19] Sébastien Leclaire et al. "Enhanced equilibrium distribution functions for simulating immiscible multiphase flows with variable density ratios in a class of lattice Boltzmann models". In: *International Journal of Multiphase Flow* 57 (2013). doi: https://doi.org/10.1016/j.ijmultiphaseflow.2013.07.001.

[20] Sébastien Leclaire et al. "Generalized three-dimensional lattice Boltzmann color-gradient method for immiscible two-phase pore-scale imbibition and drainage in porous media." In: *Physical review. E* 95.3 (Mar. 2017). doi: 10.1103/PhysRevE.95.033306.

[21] Haihu Liu, Albert J. Valocchi, and Qinjun Kang. "Three-dimensional lattice Boltzmann model for immiscible two-phase flow simulations". In: *Phys. Rev. E* 85.4 (Apr. 2012). doi: 10.1103/PhysRevE.85.046309.

[22] Alessandro De Rosis. "Non-orthogonal central moments relaxing to a discrete equilibrium: A D2Q9 lattice Boltzmann model". In: *Europhysics Letters* 116.4 (Jan. 2017). doi: 10.1209/0295-5075/116/44003.

[23] T. J. Spencer, I. Halliday, and C. M. Care. "Lattice Boltzmann equation method for multiple immiscible continuum fluids". In: *Phys. Rev. E* 82.6 (Dec. 2010). doi: 10.1103/PhysRevE.82.066701.

[24] A. Subhedar et al. "Interface tracking characteristics of color-gradient lattice Boltzmann model for immiscible fluids". In: *Phys. Rev. E* 101.1 (Jan. 2020). doi: 10.1103/PhysRevE.101.013313.

[25] S. Succi. *The lattice Boltzmann equation for fluid dynamics and beyond*. Numerical mathematics and scientific computation. Oxford, New York: Clarendon Press ; Oxford University Press, 2001.

[26] Jonas Tölke. "Lattice Boltzmann simulations of binary fluid flow through porous media". In: *Philosophical Transactions of the Royal Society of London. Series A: Mathematical, Physical and Engineering Sciences* 360.1792 (Mar. 2002). doi: 10.1098/rsta.2001.0944.

Part II

Literature and Theory

Chapter 4 | Literature Review

Key Points

- Energy-based wetting implementations in multiphase LBM define solid-liquid interaction forces or energies, sometimes at the microscopic level, from which contact angles naturally arise.
- Geometry-based wetting implementations in multiphase LBM directly define and enforce contact angles.
- A systematic literature review reveals that energy-based methods that work at high density and viscosity ratios have not been developed for CG-LBM.

4.1 Towards Alternatives

In chapter 2, we outlined that ink-jetting simulations must handle immiscible fluids at high density and viscosity ratios under dynamic conditions. Described in chapter 3, Central Moment Color-Gradient LBM has already been used to successfully simulate this jetting process [4, 20]. Expanding on these achievements, the implementation of wetting on mobile particles, along with the better capture of dynamic wetting phenomena at the meniscus, is desired, as discussed in chapter 1.

The physical relation between the apparent macroscopic contact angle, another contact angle measured closer to the contact line, and other microscopic parameters such as slip length, especially in dynamic situations, is not always clear [5]. What is clear, though, is that:

Intermolecular interactions precede their macroscopic manifestations, such as contact angles.

Just beyond the molecular scale of cohesive and adhesive intermolecular forces, surface tension characterizes an interface as soon as it can be described continuously. Apparent contact angles are described at the macroscopic scale, and therefore depend on the aforementioned microscopic interactions. This would suggest that simulations might benefit from wetting implementations based on energy-related arguments (such as surface energy or surface tension balance at equilibrium) and microscopic interactions, rather than geometry and fixed contact angles. This goes hand-in-hand with the preference to leverage the microscopic foundations of LBM indicated in the conclusions of chapter 3.

However, even without sub-lattice or microscopic input (e.g., contact angle hysteresis windows or microscopic slip lengths from section 2.2.2), geometry-based LBM wetting schemes that directly enforce contact angles near solid surfaces actually exhibit variations in macroscopic contact angles in dynamic situations, which remarkably can match physical scaling laws [15, 26]. This justifies the use of such conditions in dynamic situations, like in [4]. Despite its reference to clearly-defined microscopic phenomena, LBM does not need to reflect the real micro- and mesoscopic physics to mimic Navier-Stokes behavior [9,

22] Additionally, because of CG-LBM's implicit interface tracking, a geometry-based boundary condition in CG-LBM may well be essentially equivalent to an energy-based condition, were interface-tracking done explicitly [6]. Whether an energy-based framework is intrinsically advantageous therefore remains to be seen.

Since we already know that CG-LBM will be used, and that we clarified our interest in defining and evaluating energy-based wetting, the research question can be rephrased:

How can **energy-based wetting implementations in CG-LBM** be used to simulate multiphase flows with dynamic capillary phenomena?

4.2 Literature Search and Categorization

Appendix A documents the systematic approach used to gather the references to answer this question, targeting wetting boundary conditions in general, and other implementations tailored for moving or curved solid boundaries. References were categorized based on the refined research question in order to highlight a research gap:

- **Multiphase Method**
  Recognizing an energy-based implementation in CG-LBM starts by recognizing what LBM multiphase model was used. In addition, understanding non-CG wetting implementations may prove useful in defining novel or alternative methods for CG-LBM. References are sorted between CG-LBM, Shan-Chen (SC), and phase-field/Free-Energy (PF/FE). The latter two are fundamentally different multiphase methods, and in this report, PF/FE methods cover all explicitly interface-tracking methods [12].

- **Tested Density Ratio**
  Implementations with density ratios under $\mathcal{O}(10^2)$ were excluded from the review as unproven techniques in the ink-jet printing regime. Remaining papers reach either $\mathcal{O}(10^2)$ or $\mathcal{O}(10^3)$ density ratio. The viscosity ratio is not used as a selection criterion, because density ratio is a sufficient and more stringent selection criterion.

- **Wetting Method Basis**
  Clearly energy-related wetting implementations need to be identified. Results are divided between energy-based and geometry-related techniques.

4.3 Wetting Implementations

To frame later discussion, an overview of the most notable wetting implementations identified during the literature search is given.

4.3.1 Energy-based Techniques

Long-Range Forces

Long-range solid-fluid interactions, mirroring the physical microscopic basis of wetting [5],[1] are typical of Shan-Chen LBM multiphase models, where fluid-fluid cohesive interactions are implemented with a force which depends on local component density and the presence of neighboring particles of the other component. An analogous solid-fluid adhesion force $\boldsymbol{F}_{\text{ads},k}$ is used to mediate wetting between the solid and fluid k [12]:

$$\boldsymbol{F}_{\text{ads},k} = -G_{\text{ads},k}\rho_k(\boldsymbol{x},t)\sum_i w_i s(\boldsymbol{x}+\boldsymbol{c}_i\Delta t)\boldsymbol{c}_i \tag{4.1}$$

[1]These in-simulation interactions are "long-range" insofar as they apply to fluid particles which are not in immediate physical contact with the wall (i.e., they are not colliding with the wall). The physical counterpart interactions evoked here are Van der Waals forces between the solid walls and the fluid molecules.

where $G_{\text{ads},k}$ is an interaction strength parameter which governs wetting, and s is a switch function that is unity when $\boldsymbol{x} + \boldsymbol{c}_i \Delta t$ is a solid node. The interaction force sometimes also includes a virtual solid density as a tuning parameter [25, 27, 32]. Parameters are tuned by recovering a desired equilibrium contact angle, either analytically or with preliminary calibration simulations.

Energy-Minimizing Boundary Conditions

For explicit interface-tracking methods (PF/FE), boundary conditions are set on the phase-field, which follows the fluid-fluid interface: conditions on solid boundaries necessarily relate to contact-line behavior. PF/FE methods hinge on free energy minimization [12] (which is compatible with a definition of surface tension given in chapter 2 [5]) or the use of chemical energy potentials, which directly integrate contributions from wetting.

4.3.2 Geometry-based Techniques

Direct Enforcement Boundary Conditions

CG-LBM often directly enforces a desired equilibrium contact angle by reorienting the color-gradient vector $\nabla \rho^N$ at solid boundaries. Many such implementations redistribute particles to change the color-gradient unit vector without changing its magnitude [1, 17, 33]. This technique is used in the precursor work [4]. This direct enforcement may appear strict and inflexible, but can be augmented by contact angle hysteresis windows or velocity-dependent dynamic contact angle recalculation [1, 28].

Adapted phase-field Boundary Conditions

It is possible to reformulate phase-field boundary conditions from explicit interface-tracking methods for CG- and SC-LBM, which ***implicitly*** track the fluid-fluid interface, by identifying an equivalent proxy to the phase-field (e.g., the indicator ρ^N for CG-LBM, or the equivalent order parameter of SC) [24, 26]. These methods can lose their original energy-basis due to the lack of a free-energy minimization framework in either CG- or SC-LBM, for example. Despite this, these boundary conditions can lead to emergent and physically-consistent contact-line dynamics, likely due to embedded effective slip lengths [6, 26]. Since the method is geometry-based and is meant to enforce a particular contact angle, hysteresis windows can also be implemented.

4.4 Summary of Results

Table 4.1 shows the outcome of the categorization of the remaining references that were not filtered out by the systematic accumulation of sources. A fully green row would have indicated a proven energy-based CG-LBM wetting implementation, tried in the parameter space of drop-on-demand inkjet printing.

According to the literature review, and to the best of the author's knowledge:

There are no documented CG-LBM results with energy-based wetting implementations in the parameter space of drop-on-demand inkjet printing (e.g. high density and viscosity ratio under dynamic conditions).

Therefore, the refined research question from section 4.1 remains open. To answer it, we must first formulate or find such an energy-based wetting implementation. Initially, the use of a Shan-Chen-type long-range solid-fluid interaction in CG-LBM was considered. Shan-Chan uses formally-analogous short- and long-range interactions to model fluid-fluid and fluid-solid interactions, respectively [12]. This self-consistency acknowledges the fact that the intermolecular interactions that lead to surface tension are related, whether for fluid-fluid or fluid-solid interfaces [5].

Applying the same consistency in CG-LBM would mean defining surface tensions between the solid and the fluids. This would follow the conclusions of section 3.6, defining a method that:

Reference	Multiphase Model	Density Ratio	Wetting Method Basis
[1]	CG	**1000**	Geometry
[2]	SC	**100**	Energy
[3]	PF/FE	**1000**	Energy
[7]	PF/FE	**1000**	Geometry
[8]	PF/FE	**100**	Energy
[10]	PF/FE	**100**	Energy
[11]	SC	**1000**	Energy
[13]	PF/FE	**1000**	Geometry
[14]	SC	**1000**	Geometry
[16]	SC	**1000**	Energy
[17]	CG	**1000**	Geometry
[18]	PF/FE	**1000**	Energy
[21]	PF/FE	**100**	Geometry
[23]	PF/FE	**1000**	Geometry
[24]	SC	**1000**	Geometry
[25]	SC	**100**	Energy
[26]	CG	**100**	Geometry
[27]	SC	**1000**	Energy
[29]	PF/FE	**1000**	Geometry
[30]	SC	**100**	Energy
[31]	SC	**1000**	Energy
[33]	PF/FE	**1000**	Geometry
[34]	CG	**100**	Geometry
[35]	SC	**1000**	Energy

Table 4.1: Categorized Remaining References. A fully green row would have indicated a proven energy-based CG-LBM wetting implementation, tried in the parameter space of drop-on-demand inkjet printing.

- describes wetting at the microscopic scale in an analogous way to fluid-fluid interactions, which is physically consistent [5],
- mediates wetting with the perturbation and recoloring operators, which necessarily conserve mass and momentum [19],
- leverages the stability and sound mathematical formulation of a CG-LBM proven to work in the inkjet printing regime [4].

Chapter 4 References

[1] Takashi Akai, Branko Bijeljic, and Martin J. Blunt. "Wetting boundary condition for the color-gradient lattice Boltzmann method: Validation with analytical and experimental data". In: *Advances in Water Resources* 116 (2018). doi: https://doi.org/10.1016/j.advwatres.2018.03.014.

[2] S. Bommer et al. "Depinning of drops on inclined smooth and topographic surfaces: Experimental and lattice Boltzmann model study". In: *Langmuir* 30.37 (2014). doi: 10.1021/la501603x.

[3] K.W. Connington et al. "Lattice Boltzmann simulations of particle-laden liquid bridges: Effects of volume fraction and wettability". In: *International Journal of Multiphase Flow* 76 (2015). doi: 10.1016/j.ijmultiphaseflow.2015.05.014.

[4] Karun Pravin Nirod Datadien. "Directional instabilities in microdroplet jetting: a numerical approach". PhD thesis. Applied Physics and Science Education, Jan. 31, 2024.

[5] Pierre-Gilles De Gennes, Françoise Brochard-Wyart, and David Quéré. *Capillarity and Wetting Phenomena*. New York, NY: Springer New York, 2004. doi: 10.1007/978-0-387-21656-0.

[6] Hang Ding and Peter D. M. Spelt. "Wetting condition in diffuse interface simulations of contact line motion". In: *Phys. Rev. E* 75.4 (Apr. 2007). doi: 10.1103/PhysRevE.75.046708.

[7] A. Fakhari and D. Bolster. "Diffuse interface modeling of three-phase contact line dynamics on curved boundaries: A lattice Boltzmann model for large density and viscosity ratios". In: *Journal of Computational Physics* 334 (2017). doi: 10.1016/j.jcp.2017.01.025.

[8] S. Farokhirad and T. Lee. "Computational study of microparticle effect on self-propelled jumping of droplets from superhydrophobic substrates". In: *International Journal of Multiphase Flow* 95 (2017). doi: 10.1016/j.ijmultiphaseflow.2017.05.008.

[9] Martin Geier, Andreas Greiner, and Jan G. Korvink. "Cascaded digital lattice Boltzmann automata for high Reynolds number flow". In: *Phys. Rev. E* 73.6 (June 2006). doi: 10.1103/PhysRevE.73.066705.

[10] R. Haghani, M.H. Rahimian, and M. Taghilou. "LBM Simulation of a Droplet Dripping Down a Hole". In: *Engineering Applications of Computational Fluid Mechanics* 7.4 (2013). doi: 10.1080/19942060.2013.11015485.

[11] X. He and H. Peng. "Contact-point analysis of attached-wall cavitation evolution on chemically patterned surfaces using the lattice Boltzmann method". In: *Chemical Engineering Science* 287 (2024). doi: 10.1016/j.ces.2024.119753.

[12] Haibo Huang, Michael C. Sukop, and Xi-Yun Lu. *Multiphase Lattice Boltzmann Methods: Theory and Application*. Wiley, July 2015. doi: 10.1002/9781118971451.

[13] J.-J. Huang and L. Zhang. "Simplified method for wetting on curved boundaries in conservative phase-field lattice-Boltzmann simulation of two-phase flows with large density ratios". In: *Physics of Fluids* 34.8 (2022). doi: 10.1063/5.0101291.

[14] J. Jiang et al. "Discontinuous dewetting dynamics of highly viscous droplets on chemically heterogeneous substrates". In: *Journal of Colloid and Interface Science* 629 (2023). doi: 10.1016/j.jcis.2022.09.064.

[15] M. Latva-Kokko and Daniel H. Rothman. "Scaling of Dynamic Contact Angles in a Lattice-Boltzmann Model". In: *Phys. Rev. Lett.* 98.25 (June 2007). doi: 10.1103/PhysRevLett.98.254503.

[16] M.P. Lautenschlaeger et al. “Understanding Electrolyte Filling of Lithium-Ion Battery Electrodes on the Pore Scale Using the Lattice Boltzmann Method”. In: *Batteries and Supercaps* 5.7 (2022). doi: 10.1002/batt.202200090.

[17] Sébastien Leclaire et al. “Generalized three-dimensional lattice Boltzmann color-gradient method for immiscible two-phase pore-scale imbibition and drainage in porous media.” In: *Physical review. E* 95.3 (Mar. 2017). doi: 10.1103/PhysRevE.95.033306.

[18] R.-J. Li and Y. Morozumi. “A lattice boltzmann simulation of contact line motion and internal fluid flows in an evaporating droplet on homogenous substrates”. In: *Journal of Chemical Engineering of Japan* 45.3 (2012). doi: 10.1252/jcej.11we177.

[19] Haihu Liu, Albert J. Valocchi, and Qinjun Kang. “Three-dimensional lattice Boltzmann model for immiscible two-phase flow simulations”. In: *Phys. Rev. E* 85.4 (Apr. 2012). doi: 10.1103/PhysRevE.85.046309.

[20] D. Lohse. “Fundamental Fluid Dynamics Challenges in Inkjet Printing”. In: *Annual Review of Fluid Mechanics* 54 (2021). doi: 10.1146/annurev-fluid-022321-114001.

[21] X.-D. Niu et al. “A simple diffuse interface immersed-boundary scheme for multiphase flows with curved boundaries”. In: *International Journal of Multiphase Flow* 157 (2022). doi: 10.1016/j.ijmultiphaseflow.2022.104266.

[22] S. Succi. *The lattice Boltzmann equation for fluid dynamics and beyond*. Numerical mathematics and scientific computation. Oxford, New York: Clarendon Press ; Oxford University Press, 2001.

[23] M Sugimoto et al. “Coolant Wetting Simulation on Simplified Stator Coil Model by the Phase-Field Lattice Boltzmann Method”. In: *ENTROPY* 24.2 (Feb. 2022). doi: 10.3390/e24020219.

[24] J. Tang, S. Zhang, and H. Wu. “Simulating wetting phenomenon with large density ratios based on weighted-orthogonal multiple-relaxation-time pseudopotential lattice Boltzmann model”. In: *Computers and Fluids* 244 (2022). doi: 10.1016/j.compfluid.2022.105563.

[25] G. Wang, U. D’Ortona, and P. Guichardon. “Improved partially saturated method for the lattice Boltzmann pseudopotential multicomponent flows”. In: *Physical Review E* 107.3 (2023). doi: 10.1103/PhysRevE.107.035301.

[26] N. Wang, W. Ni, and H. Liu. “Geometrical wetting boundary condition for complex geometries in lattice Boltzmann color-gradient model”. In: *Physics of Fluids* 36.1 (2024). doi: 10.1063/5.0180592.

[27] GQ Wu and S Chen. “Simulating spray coating processes by a three-dimensional lattice Boltzmann method-immersed boundary method approach”. In: *CHEMICAL ENGINEERING SCIENCE* 263 (Dec. 14, 2022). doi: 10.1016/j.ces.2022.118091.

[28] Zhiyuan Xu, Haihu Liu, and Albert J. Valocchi. “Lattice Boltzmann simulation of immiscible two-phase flow with capillary valve effect in porous media”. In: *Water Resources Research* 53.5 (2017). doi: https://doi.org/10.1002/2017WR020373.

[29] Y.Y. Yan and Y.Q. Zu. “A lattice Boltzmann method for incompressible two-phase flows on partial wetting surface with large density ratio”. In: *Journal of Computational Physics* 227.1 (2007). doi: 10.1016/j.jcp.2007.08.010.

[30] K.A. Yuana et al. “Transient Lattice Boltzmann Numerical Simulation during the Dewetting of Liquid Droplet on a Flat Surface”. In: *Computers and Fluids* 255 (2023). doi: 10.1016/j.compfluid.2023.105836.

[31] Q.-Y. Zhang, D.-K. Sun, and M.-F. Zhu. “A multicomponent multiphase lattice Boltzmann model with large liquid-gas density ratios for simulations of wetting phenomena”. In: *Chinese Physics B* 26.8 (2017). doi: 10.1088/1674-1056/26/8/084701.

[32] T Zhang et al. “Pore-scale modelling of water sorption in nanopore systems of shale”. In: *INTERNATIONAL JOURNAL OF COAL GEOLOGY* 273 (May 15, 2023). doi: 10.1016/j.coal.2023.104266.

[33] X. Zhang et al. “Rayleigh-Plateau Instability of a Particle-Laden Liquid Column: A Lattice Boltzmann Study”. In: *Langmuir* 38.11 (2022). doi: 10.1021/acs.langmuir.1c03262.

[34] W. Zhao et al. “Simulation of droplet impacting a square solid obstacle in microchannel with different wettability by using high density ratio pseudopotential multiple-relaxation-time (MRT) lattice Boltzmann method (LBM)”. In: *Canadian Journal of Physics* 97.1 (2019). doi: 10.1139/cjp-2018-0126.

[35] Lin Zheng, Song Zheng, and Qinglan Zhai. “Phase-field lattice Boltzmann equation for wettable particle fluid dynamics”. In: *Phys. Rev. E* 108.2 (Aug. 2023). doi: 10.1103/PhysRevE.108.025304.

Chapter 5 | Alternative CG Wetting

Key Points

- Solid-Model Fluids (s-fluids) are fluid phases that mediate wetting on solid surfaces with additional CG fluid-fluid interactions.
- Superviscous s-fluids could be used to model solid particles with any N-fluid CG implementation.
- Solid Phase Perturbation (SPP) refers to additional fluid-phase perturbation near solid walls that cause fluids to preferentially wet them.
- SPP could enforce wetting on solid surfaces without boundary-conditions for any number of actual in-simulation fluid phases.

In this chapter, we discuss wetting implementations that, while unproven in the inkjet-printing regime, approach the hypothetical energy-based and CG-consistent formulation of the concluding remarks of section 4.4. After discussing their limitations, we describe possible adaptations to Flow Matters' CG-LBM implementation from [1]. We note that the described adaptations are by no means the only re-interpretations of these alternative wetting techniques.

5.1 Solid-Model Fluids

As described in [7], one possible way to model wetting is to introduce an additional fluid or fluid-like phase (the *solid-model fluid*) to the simulation to model capillary effects near solid surfaces. Shown in figure 5.1, a CG-LBM Smooth Particle Model (CG-SPM) models the solid with such a fluid, with its own surface tensions with other (actual) fluids, and is involved in the perturbation and recoloring steps. In this case, an $N > 2$ fluid CG implementation is required, which will be described in more detail in chapter 6: for the moment, consider only that CG can be extended to N-fluids by perturbing and recoloring each fluid with each other fluid with superimposed and independent contributions [6, 7].

5.1.1 Original Implementation

The additional solid-model fluid (s-fluid) is initialized with a separate phase-field ϕ_P, where the $\phi_P = 0.5$ contour marks the solid's boundary.[1] The diffuse interface transitions from the actual fluid to the solid with a truncated hyperbolic tangent profile: the fluid-solid interfaces are of the exact same nature as typical CG-LBM fluid-fluid interfaces. The s-fluid is contained within a thin solid wall which it wets completely,[2]

[1] The solid phase-field ϕ_P varies between 0 and 1, not -1 and 1.

[2] This is accomplished with a geometry-based boundary condition that directly enforces a null contact angle. The use of this boundary condition is incidental to the implementation: the actual wetting (between fluids and the s-fluid) is handled by the perturbation and recoloring operators through the surface tensions.

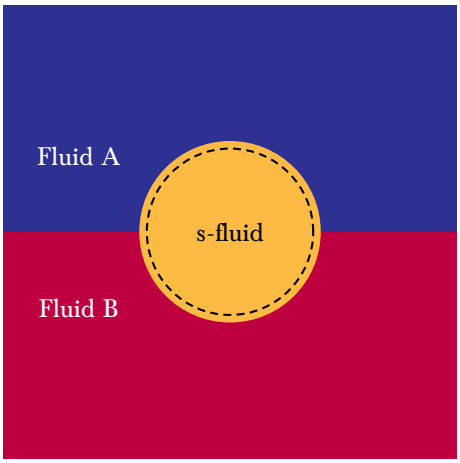

Figure 5.1: CG-SPM Multiphase Simulations. Using a smooth-particle-method, solid particles are modeled by a solid-model fluid (s-fluid), which is constrained within the actual boundaries of the solid (***the dotted line here***), yet also has a $\tanh$ profile like fluid-fluid CG-LBM interfaces. Wetting is mediated by the solid-model fluid's surface tensions, corresponding to either actual fluid's affinity with the actual solid. Adapted from [7]

occupying the entirety of the solid volume. The s-fluid has its own surface tensions σ_{Sl} with each fluid l, as well as a density ρ_S^0 matching that of the real solid being modelled. The s-fluid therefore also has its own CG-LBM α_S parameter and speed-of-sound c_s^S.

In N-fluid CG-LBM, the color-gradient $\boldsymbol{F}_{lm}$ is expressed for each pair of fluids l and m as [6]:

$$\boldsymbol{F}_{lm} = \frac{\rho_m}{\rho}\nabla\left(\frac{\rho_l}{\rho}\right) - \frac{\rho_l}{\rho}\nabla\left(\frac{\rho_m}{\rho}\right) \tag{5.1}$$

where $\rho = \sum_k \rho_k + \rho_S\phi_S$ is the total density calculated with ***all*** phases, including the k actual fluids and the s-fluid. The color-gradient now also tracks solid boundaries. Both the perturbation and recoloring operators are otherwise run for all pairs among the N fluids including the s-fluid, and wetting is now mediated by the tunable solid-liquid surface tensions σ_{Sl}. The involvement of solid-liquid surface tensions is consistent with Young's law in equation 2.11, which is used to define a wetting parameter χ, which for $N = 2$ fluid simulations with a red r and blue b fluid is set by:

$$\chi = \frac{\sigma_{Sr} - \sigma_{Sb}}{\sigma_{rb}} = \cos\theta_E \tag{5.2}$$

where θ_E is the desired static equilibrium contact angle.

No-slip is not strictly enforced at the solid boundary. Solid particles' positions are updated based on a momentum-exchange scheme between the fluid in the vicinity of the solid boundary (marked by ϕ_S) and the virtual solid particle. Hydrodynamic forces in the fluid bulk are essentially distributed across the now-diffuse solid-boundary, and are the inverse of the force felt by the virtual solid particle, the position of which is updated at every timestep and injected in the simulation by an updated solid phase-field ϕ_S. For fixed particles especially, this model is very similar to so-called partially saturated bounce-back methods. Both are able to accurately resolve hydrodynamic forces despite the diffuse solid interface, which can even be beneficial to modelling curved surfaces [5, 10].

Limitations

The model requires setting density ρ_S^0 and viscosity ν_S for the s-fluid. The original publication only investigates unity density ratios across both fluids and the s-fluid [7]. For mobile particles, the density is constrained by the ***actual*** solid density. In-simulation, the solid boundaries are identified by $\rho_S/\rho =$

$\rho_S^0 \phi_S / \rho = 0.5$, where ρ is the total local density.[3] However, if a heavy fluid displaces a light fluid (or vice versa), the local value of ρ will change for constant $\rho_S^0 \phi_S$: the wall position is dependent on flow conditions, which is a serious model error for simulating solid particles.

In CG-LBM, a single local value of viscosity must be used across relaxation and perturbation steps. For unity viscosity ratio across all fluids, the presence of s-fluid does not affect local fluid viscosity regardless of interpolation, and hydrodynamics near solid boundaries are treated exclusively by the momentum-exchange algorithm and the body forces applied to the fluid. For any other viscosity ratio, the s-fluid's viscosity will pollute local relaxation, and affect hydrodynamic behavior unpredictably.

Together, these issues make it challenging to use s-fluids as formulated in [7] in the ink-jet printing regime. Additionally, while SPM resolves the required hydrodynamics, the momentum-exchange and resulting forcing is significantly more complex than bounce-back boundary conditions, even in their extended formulations for curved or sub-lattice surfaces [5, 9]. This adds complexity to the code and reduces flexibility in handling solid surfaces.

5.1.2 Adapting the Model

The modeling of mobile particles constrains s-fluid density to that of the actual solid, and density ratios across fluids are practically inevitable. The issue of fluid-density-dependent wall/interface positions actually mirrors an issue with CG phase-fields in general, which will be described in more detail in chapter 7. Indeed, alternative phase-field formulations yield more consistent interface positions at non-unity density ratios. However, to the best of the author's knowledge, $N > 2$ fluid CG-LBM publications define the color- (or phase-field-) gradient without defining what the corresponding individual fluid phase-fields are [6, 7]. Clarifying which interfaces N-fluid CG-LBM is actually tracking is an important first step before using it for any purpose.

To avoid the added complexity of actually diffuse solid surfaces and the momentum exchange algorithm, we will investigate the use of *actual fluid directly as a solid model*. Leveraging the extended range of accessible viscosity of CM-LBM, extremely viscous fluid particles could be used to approach rigid-body motion.

Physically, these *superviscous fluid particles* would enforce no-slip by viscous dissipation near their surfaces. The particles will of course shear and deform, a model error which dissipates energy. For s-fluid viscosity tending towards infinity, momentum is transferred and shared instantaneously throughout the s-fluid. When viscosity (or *shear resistance*) is high enough, the particle should convert applied forces (hydrodynamic or capillary) into other less resistive degrees of freedom, such as linear or rotational momentum, and display rigid-body-like motion.

Numerically, CG-LBM additionally features diffuse interfaces and local viscosity interpolation, the effects of which on s-fluid modeling need to be investigated. S-fluid particle surfaces are actually maintained by the recoloring operator, since they are effectively fluid-fluid interfaces. The consequences of this are also unclear.

This leads to the following questions:

Research Questions: Superviscous Particles

- What are the phase-fields for N-fluid CG?
- What is the effect of diffuse CG-LBM interfaces on momentum-transfer to s-fluids?
- Could superviscous particles be used in the ink-jet printing regime?

[3] Reference [7] doesn't explicitly state this, but must be the case for unity density ratios for the condition "$\rho_C = 0.5$" actually given in the paper, index C corresponding to the s-fluid.

5.2 Solid-Phase Perturbation

Reference [7] on CG-SPM mediates wetting with fluid-fluid-like interactions by using an s-fluid, but also defines an entirely different fluid population, which streams, relaxes, and requires boundary treatment, whereas it was only needed to define additional perturbation. Similar to Shan-Chen long-range solid/liquid interaction [3], additional perturbation to the actual fluid populations near solid walls, ***solid-phase perturbation*** (SPP), could be used to mediate wetting without the definition of an additional fluid.

5.2.1 Original Implementation

In [2], SPP acts on fluid l population by an additional perturbation Δf_i^l applied near solid boundaries:

$$\Delta f_i^l = \rho_l \cos(2(\theta_w - \theta_i))\sigma_{Sl} \tag{5.3}$$

where θ_w is the "orientation of the wall", θ_i is that of the perturbed direction i, and σ_{Sl} is a "wetting surface tension". The latter is analogous to fluid-fluid surface tensions, and is defined for each fluid l interacting with the solid S: a difference in σ_{Sl} among fluids will cause preferential wetting. All surface tension parameters are comparable to actual fluid surface tensions, and qualitatively satisfies Young's equation on the contact angle from equation 5.2.

Reference [4] presents a similar scheme by treating the wall as a "stationary fluid" with constant mass density at nodes by the wall, likewise leading to additional perturbation near the wall: no full fluid is allocated for this. Fluids then undergo regular perturbation with this wall-"fluid", presumably using the wall-normal vector as the interface-marking vector.

While additional perturbation is applied, the solid is not involved in the recoloring step: in CG-LBM, recoloring is a ***numerically***-based (as opposed to being formulated from thermodynamics) operation keeping phases separate. For the solid and the liquid, segregation is enforced by bounce-back boundary conditions, and CG-like recoloring steps are not required.

Limitations

Both [2] and [4] investigate density and viscosity ratios of $\mathcal{O}(1)$. Furthermore, while the term in equation 5.3 has some passing resemblance to our perturbation operator in equation (6.11),[4] it is expressed for a substantially different algorithm. Both references use older implementations of CG-LBM, with especially different segregation operators.[5]

For both [2] and [4], the authors do not make a firm claim on the relationship between the numerical surface tension parameters and the actual physical surface tensions with the solid. Equation (5.3) scales its perturbations with local fluid l density, and [4] uses a virtual constant solid ***density*** at solid boundaries as input to the wall-perturbation. Perturbation-weighting or such additional parameters have unclear physical basis, although they clearly have effects in-simulation, such as the tuning of dynamic contact angles [4].

Despite using perturbation very similar to that in section 3.5, reference [4] breaks the 1-to-1 correspondence between physical surface tension and the numerical parameter mediating surface tension: setting surface tensions even across fluid-fluid interfaces must be calibrated beforehand.[6] This is in sharp contract to modern CG-LBM, which maintains a strict relationship by fully constraining the expression for the perturbation step [8].

More importantly, while SPP in [4] is calibrated and produces a linear relationship between $\frac{\sigma_{Sr}-\sigma_{Sb}}{\sigma_{rb}}$ and equilibrium contact angle, and therefore has practical use,[7] this linear relationship does not strictly reproduce equation (5.2). In fact, for equal surface tension between either fluid and the solid, or even no surface tension between fluids and solid, ***the contact angle is not neutral*** ($90°$). This occurs despite there being supposedly no physical mechanism for any fluid to preferably wet and produce a non-neutral contact angle: the model is inaccurate. Quantitative performance of SPP in [2] is not given, and could not be evaluated away from neutral wetting.

[4] Consider that the dot product in equation (3.50) is similar to the dot product of wall-normals and velocity in equation (5.3).

[5] Reference [4] uses a very similar perturbation operator, however.

[6] We note that the relationship between the surface tension parameter and the physical surface tension is linear: the physics are actually reflected, and the 1-to-1 relationship is only broken by incorrect constant scaling of the perturbation term.

[7] At least at unity density and viscosity ratio.

5.2.2 Adapting the Model

To the author's knowledge, SPP has not been adapted to modern CG-LBM as described in section 3.5. Modern CG-LBM actually uses physical surface tension directly as a numerical parameter [6, 8], making it perhaps possible to directly use physical surface energies in defining fluid-solid relationships.

Initially, it was believed that adapting this technique would require defining a fully diffuse solid-liquid interface placed in the vicinity of solid walls. This would resemble the s-fluid method of reference [7], but only using ϕ_S in entirely separate perturbation steps near solid boundaries, and without defining an actual fluid. However, for fixed solid boundaries especially, why define a diffuse interface when the exact position of the fluid-solid interface is actually known, at least for flat walls coinciding with domain boundaries? Since SPP is completely unproven for modern CG-LBM, it is sensible to start with such a simple case. Besides, using a diffuse boundary implies the definition of a diffuse interface thickness for the solid, an additional parameter with no connection to any physical phenomena. Therefore, perturbation formally similar to typical fluid-fluid CG-LBM interaction near solid walls will only be added at the first boundary node beyond the wall.

As few additional non-physical parameters as possible will be added: no solid density will be defined as in [4]. However, special care will be given to understand the effect of boundary conditions: the non-neutral contact angle produced in [4] for no or neutral SPP is apparently caused only by the prescription of solid density at the wall.

Together, this poses the following questions:

Research Questions: Solid-Phase Perturbation

- Can SPP be adapted to modern CG-LBM to induce wetting/dewetting behavior?
- Can SPP be restricted to a single node off solid boundaries?
- Could SPP be used in the ink-jet printing regime?

Chapter 5 References

[1] Karun Pravin Nirod Datadien. "Directional instabilities in microdroplet jetting: a numerical approach". PhD thesis. Applied Physics and Science Education, Jan. 31, 2024.

[2] M.M. Dupin, I. Halliday, and C.M. Care. "Multi-component lattice Boltzmann equation for mesoscale blood flow". In: *Journal of Physics A: Mathematical and General* 36.31 (2003). doi: 10.1088/0305-4470/36/31/313.

[3] Haibo Huang, Michael C. Sukop, and Xi-Yun Lu. *Multiphase Lattice Boltzmann Methods: Theory and Application*. Wiley, July 2015. doi: 10.1002/9781118971451.

[4] A. Kawasaki et al. "A lattice Boltzmann model for contact-line motions". In: *Computers and Mathematics with Applications* 55.7 (2008). doi: 10.1016/j.camwa.2007.08.026.

[5] Timm Krüger et al. *The Lattice Boltzmann Method: Principles and Practice*. Graduate Texts in Physics. Springer, 2016.

[6] Sébastien Leclaire, Marcelo Reggio, and Jean-Yves Trépanier. "Progress and investigation on lattice Boltzmann modeling of multiple immiscible fluids or components with variable density and viscosity ratios". In: *Journal of Computational Physics* 246 (2013). doi: https://doi.org/10.1016/j.jcp.2013.03.039.

[7] Y.K. Lee and K.H. Ahn. "Particle dynamics at fluid interfaces studied by the color gradient lattice Boltzmann method coupled with the smoothed profile method". In: *Physical Review E* 101.5 (2020). doi: 10.1103/PhysRevE.101.053302.

[8] Haihu Liu, Albert J. Valocchi, and Qinjun Kang. "Three-dimensional lattice Boltzmann model for immiscible two-phase flow simulations". In: *Phys. Rev. E* 85.4 (Apr. 2012). doi: 10.1103/PhysRevE.85.046309.

[9] C. Livi et al. "Influence of numerical resolution on the dynamics of finite-size particles with the lattice Boltzmann method". In: *Physical Review E* 103.1 (2021). doi: 10.1103/PhysRevE.103.013303.

[10] Young Ki Lee. "Applications of lattice Boltzmann method combined with smoothed profile method for particulate flows: a brief review". In: (Oct. 21, 2023). doi: 10.1007/s13367-023-00077-8.

Chapter 6 | N-fluid CG-LBM Theory

Key Points

- Colorblind CG-LBM is a strictly equivalent formulation of CG-LBM which limits computation storage.
- In CG-LBM, fluids locally form a multi-component mixture with its own properties.
- Some of these mixture properties are constrained, while the choice of local viscosity is free.
- A novel N-fluid phase-field formulation is proposed that links N-fluid CG-LBM to its tracked phase-fields.

In this chapter, extensions of CG-LBM to N-fluids are presented, notably in their memory- and computationally efficient form: *Colorblind* CG-LBM. New theory regarding phase-fields and mixture properties in N-fluid CG-LBM is presented, showing that local viscosity interpolation is free, and revealing the connection between N-fluid color-gradient and phase-fields for the first time.

6.1 N-Fluid CG-LBM

CG-LBM can be extended to N-fluids by increasing the number of populations f_i^k, each with their own fluid density ρ_k and contribution to momentum. Each additional fluid phase undergoes perturbation and recoloring with the others.

6.1.1 Colorblind CG-LBM

We first describe the state-of-the-art for colorblind CG-LBM, as developed in [5] and used in [6]. A *total population* f is used, which is the sum of individual fluid k populations [5]:

$$f_i = \sum_k f_i^k \tag{6.1}$$

from which follows a definition of macroscopic moments, with total density ρ equal to sum of individual fluid densities ρ_k:

$$\rho = \sum_i f_i \tag{6.2}$$

$$\rho = \sum_i \sum_k f_i^k = \sum_k \sum_i f_i^k \tag{6.3}$$

$$\rho = \sum_k \rho_k \tag{6.4}$$

and total momentum ρu_α:

$$\rho u_\alpha = \sum_i f_i c_{i\alpha} \tag{6.5}$$

$$\rho u_\alpha = \sum_i \sum_k f_i^k c_{i\alpha} = \sum_k \sum_i f_i^k c_{i\alpha} \tag{6.6}$$

Through equations (6.4) and (6.5), these moments contain the same macroscopic information as the CG-LBM presented in section 3.5, with the first-order moment equation (6.6) being identical to equation (3.46): indeed, cbCG is a ***strictly equivalent*** formulation of CG, without any simplifications or additional assumptions. The formulas presented here for colorblind populations are also always the corresponding sums of the individual fluid populations from section 3.5.

The colorblind function equilibrium f_i^{eq} is the sum of individual fluid k equilibria from equation (3.44) [5]:

$$f_i^{\text{eq}} = \sum_k f_i^{k,\text{eq}} \tag{6.7}$$

which in fact simplifies to:

$$f_i^{\text{eq}} = \rho \left[\bar{\phi}_i + w_i \left(\frac{c_{i\alpha} u_\alpha}{c_s^2} + \frac{u_\alpha u_\beta (c_{i\alpha} c_{i_\beta} - c_s^2 \delta_{\alpha\beta})}{2 c_s^4} \right) \right] \tag{6.8}$$

where $\bar{\phi}_i = \sum_k (\frac{\rho_k}{\rho}) \phi_i^k$ is the density-weighted arithmetic average of the rest component,[1] a point further discussed in section 6.1.2. Relaxation towards this equilibrium is otherwise unaffected, progressing at the same local relaxation time τ_{eff} from section 3.5 to yield the post-relaxation populations:

$$f_i^\star = \sum_k f_i^{k\star} = f_i \left(1 - \frac{\Delta t}{\tau_{\text{eff}}}\right) + f_i^{\text{eq}} \frac{\Delta t}{\tau_{\text{eff}}} \tag{6.9}$$

As noted in section 5.1, the color-gradient $\boldsymbol{F}_{lm}$ between two fluids l and m is [5]:

$$\boldsymbol{F}_{lm} = \frac{\rho_m}{\rho} \nabla \left(\frac{\rho_l}{\rho} \right) - \frac{\rho_l}{\rho} \nabla \left(\frac{\rho_m}{\rho} \right) \tag{6.10}$$

This color-gradient is used to perturb fluid l's post-relaxation populations $f_i^{l\star}$ with all other fluids to give the post-perturbation populations:

$$f_i^{l\star\star} = \Omega_i^{l,(2)}(f_i^{l\star}) = f_i^{l\star} + \sum_{\substack{m \\ m \neq l}} \frac{1}{2} A_{lm} C_{lm} |\boldsymbol{F}_{lm}| \left[w_i \frac{(\boldsymbol{c}_i \cdot \boldsymbol{F}_{lm})^2}{|\boldsymbol{F}_{lm}|^2} - B_i \right] \tag{6.11}$$

with

$$A_{lm} = \frac{9}{2} \sigma_{lm} \omega_{\text{eff}} \tag{6.12}$$

with σ_{lm} the surface tension between the two fluids, and $\omega_{\text{eff}} = 1/\tau_{\text{eff}}$ the local relaxation rate. The concentration factor C_{lm} limits the perturbations for sufficient local densities of the fluids.[2] The perturbations in equation (6.11) are independent of each other across all fluids: the *total* population can be directly perturbed to yield the total perturbed population $f_i^{\star\star}$ [5]:

$$f_i^{\star\star} = \sum_k f_i^{k\star\star} = \sum_k \Omega_i^{k,(2)}(f_i^{k\star}) \tag{6.14}$$

[1] Publications will usually refer to an average of $\alpha_k \to \bar{\alpha}$ [5]. Because ϕ_i^k is a linear function of α_k, using either average is equivalent.

[2] With a suggested form [5]:

$$C_{lm} = \min \left\{ \eta \frac{\rho_l}{\rho_l^0} \frac{\rho_m}{\rho_m^0}, 1 \right\} \tag{6.13}$$

The recoloring operator recovers the post-recoloring fluid l population $f_i^{l\star\star\star}$ from the total post-perturbation population:

$$f_i^{l\star\star\star} = \Omega_i^{l,(3)}(f_i^{\star\star}) = \frac{\rho_l}{\rho} f_i^{\star\star} + \sum_{\substack{m \\ m\neq l}} \beta_{lm} \frac{\rho_l}{\rho} \frac{\rho_m}{\rho} \cos(\varphi_i^{lm}) f_i^{\text{eq}}|_{\boldsymbol{u}=0} \tag{6.15}$$

where β_{lm} is the fluid-pair segregation parameter, and $\cos(\varphi_i^{lm})$ is defined with the fluid-pair color-gradient $\boldsymbol{F}_{lm}$ as in equation (3.54).[3] Fluids are recolored and streamed one-by-one from the total post-perturbation population $f_i^{\star\star}$, recovering the fluids' densities as the zeroth moment in velocity of the streamed populations [5]. The sum of all streamed populations is the next timestep's total population.

Extended Equilibria and Central Moments

The extended equilibrium terms in equations (3.48) and (3.49) are summed over all fluids to yield colorblind/total extended equilibrium terms Φ_i, which can be computed directly with the total density gradient $\nabla\rho$ [3]. Likewise, the CM implementation used in [1] is formulated colorblind with extended equilibrium terms [2]: it is possible to directly take the central moments of the total populations f_i. These total terms or total moments are strictly equivalent to the sum of individual fluid terms or moments because fluids all share the same local velocity and relaxation rate.

Relevance to Alternative Wetting

For N fluids, we have $\frac{1}{2}N(N-1)$ unique fluid pairs. Instead of storing populations growing with $\mathcal{O}(N^2)$, cbCG stores a single total population,[4] with a $\mathcal{O}(N)$ growth in density fields. The $\mathcal{O}(N^2)$ color-gradients of equation (6.10) are computed as required and not stored, with only the fractional densities $\frac{\rho_k}{\rho}$ and their gradients $\nabla(\frac{\rho_k}{\rho})$ being computed and stored, requiring storage and gradient computation needs growing with $\mathcal{O}(N)$ [5]. For M superviscous particles, each modeled with a separate fluid, cbCG ensures storage needs scale with $\mathcal{O}(M)$

Since only the total population is relaxed, cbCG also reduces local relaxation computations from $\mathcal{O}(N)$ to $\mathcal{O}(1)$ in each direction. The colorblind perturbation step in equation (6.14) requires $\frac{1}{2}N(N-1) = \mathcal{O}(N^2)$ local computations. The total number of computations can be divided by two, perturbing the total population by ***independent fluid-pairs***, leveraging $\boldsymbol{F}_{lm} = -\boldsymbol{F}_{ml}$:

$$\boxed{f_i^{\star\star} = \Omega_i^{(2)}(f_i^{\star}) = f_i^{\star} + \sum_l \sum_{m>l} A_{lm} C_{lm} |\boldsymbol{F}_{lm}| \left[w_i \frac{(\boldsymbol{c}_i \cdot \boldsymbol{F}_{lm})^2}{|\boldsymbol{F}_{lm}|^2} - B_i \right]} \tag{6.16}$$

To the best of the author's knowledge, this is the first time pair-wise perturbation is presented.

Equation (6.16) also includes the concentration term C_{lm} for each unique fluid-pair. Since solid-phase perturbation (SPP) should model the contact line, it should only be activated when at least two fluids are sufficiently present, which is exactly what C_{lm} does. Conversely, SPP is also relevant to N-fluid CG, insofar as it would set equilibrium contact angles for many fluids without an N-fluid generalized geometric boundary condition.

6.1.2 Local Mixtures

In this section, we argue that individual fluids present at a node form local mixtures. This has important consequences on local mixture properties, which are not consistently defined across publications. This fact will also prove very useful in section 6.2 when we define which phase-fields are being tracked in N-fluid CG-LBM.

[3] There is an ambiguity in documented N-fluid implementations for the rest equilibrium $f_i^{\text{eq}}|_{\boldsymbol{u}=0}$, which could be computed using all local fluids' equilibria, or only the fluids in the pair formed by fluids l and m [5, 6].

[4] Depending on the implementation of streaming, a cbCG implementation will typically need to store the total population, allocate a population used for the streaming of individual fluids, and a temporary population to store the sum of streamed fluid populations. This leads to a (constant) total of three populations to allocate.

At a given node in the interface region, several fluids must coexist. As was noted in section 3.5.1 for CG-LBM in general, fluids locally share the same macroscopic velocity u_α. Inspecting equation (6.6), we find the quantity:

$$\sum_i f_i^l c_{i\alpha} \tag{6.17}$$

This is the individual fluid l's contribution to total momentum, but this quantity is not necessarily conserved: only ***total*** local momentum ρu_α is recovered as the first velocity moment of the ***total*** population f_i, even when CG-LBM is not formulated colorblind [2, 5, 7, 9]. This allows local momentum transfer across components: ***the individual components collide with one another***, and therefore ***form a local mixture.*** At the macroscopic level, this multi-component fluid mixture must be also associated with its own local fluid properties.

Conversely, claiming that term (6.17) can be rewritten as:

$$\sum_i f_i^l c_{i\alpha} = \rho_l u_\alpha^l \tag{6.18}$$

leads to an expression of individual fluid l momentum-conservation, and introduces a fluid velocity u_α^l. For equation (6.6) to necessarily be satisfied requires $u_\alpha^l = u_\alpha$: all fluids' momentum contributions must be colinear. The simplest way to enforce this is by making all contributions to total population components (per velocity in the set) colinear as well:

$$f_i^l = \frac{\rho_l}{\rho} f_i \tag{6.19}$$

The recoloring step in equation (6.15) seems to imply this by recovering the fluid l populations with its fractional density. Yet, the single-fluid perturbation step in equation (6.11) violates equation (6.19) by perturbing some fluids more than others. Therefore, we will avoid the ambiguous claim that fluids have their own velocity u_α^k, because component momentum-conservation is not necessarily satisfied. Therefore, we still consider that fluids form local mixtures.

Speed-of-Sound Constant

Equations (6.7), which defines colorblind equilibrium as the sum of local fluid equilibria, and equation (3.44) defining said fluid equilibria, lead to:

$$\begin{aligned}
f_i^{\text{eq}} &= \sum_k f_i^{k,\text{eq}} \\
&= \sum_k \rho_k \left[\phi_i^k + w_i \left(\frac{c_{i\alpha} u_\alpha}{c_s^2} + \frac{u_\alpha u_\beta (c_{i\alpha} c_{i_\beta} - c_s^2 \delta_{\alpha\beta})}{2c_s^4} \right) \right] \\
f_i^{\text{eq}} &= \sum_k \rho_k \phi_i^k + \sum_k \rho_k w_i \left(\frac{c_{i\alpha} u_\alpha}{c_s^2} + \frac{u_\alpha u_\beta (c_{i\alpha} c_{i_\beta} - c_s^2 \delta_{\alpha\beta})}{2c_s^4} \right) \qquad (6.20) \\
&= \sum_k \rho \frac{\rho_k}{\rho} \phi_i^k + \rho w_i \left(\frac{c_{i\alpha} u_\alpha}{c_s^2} + \frac{u_\alpha u_\beta (c_{i\alpha} c_{i_\beta} - c_s^2 \delta_{\alpha\beta})}{2c_s^4} \right) \\
f_i^{\text{eq}} &= \rho \left[\bar{\phi}_i^k + w_i \left(\frac{c_{i\alpha} u_\alpha}{c_s^2} + \frac{u_\alpha u_\beta (c_{i\alpha} c_{i_\beta} - c_s^2 \delta_{\alpha\beta})}{2c_s^4} \right) \right] \qquad (6.21)
\end{aligned}$$

where $\bar{\phi}_i = \sum_k (\frac{\rho_k}{\rho}) \phi_i^k$, as noted previously. Recalling the CG-LBM equation of state (3.43) which defines a linear relationship between ϕ_i^k and α_k, $\bar{\phi}_i$ also defines a ***mixture*** speed-of-sound constant:

$$\boxed{\bar{\alpha} = \sum_k \left(\frac{\rho_k}{\rho} \right) \alpha_k} \tag{6.22}$$

which is a property of the local mixture. Its definition required that the velocity-related terms in (6.20) not depend on the summed k fluid index: a common local velocity among fluids implies a single multicomponent mixture, with a constrained mixture speed-of-sound constant $\bar{\alpha}$. This point is not trivial, as some publications propose inconsistent mixture speed-of-sound formulations which are not equivalent to (6.22) [2].[5]

Viscosity

As seen in equations (3.51) or (6.12), CG-LBM, colorblind or not, requires a single local relaxation time $\tau_{\text{eff}} = 1/\omega_{\text{eff}}$ in the perturbation step, also corresponding to a single local mixture viscosity ν_{eff} through Chapman-Enskog. Because only ***total*** momentum is definitely conserved, it is not necessarily the case that individual fluids locally relax at their pure-fluid times τ_k, as is proposed in [7].[6] For this to be consistent with colorblind equilibrium in equation (6.7) or colorblind relaxation in (6.9) actually requires (6.19), which we have already outlined as debatable.[7]

Therefore, it is only important that the same local value be used across relaxation and perturbation steps, and the interpolation of local viscosity appears to be free.[8]

6.2 N-Fluid phase-fields

To the best of the author's knowledge, this section clarifies which phase-fields are being tracked in N-fluid CG-LBM, for the first time, and a firm relationship between phase-field and color-gradient is established.

The cbCG implementation presented in [5] does not clearly define the phase-field for the fluids it is tracking with the color-gradient $\boldsymbol{F}_{lm}$ in equation (6.10).[9] CG-LBM indeed ***implicitly*** tracks the interface [10]: as long as the color-gradient $\boldsymbol{F}_{lm}$ is defined, the algorithm does not need to "know" or report where the interface is actually located.

An important clue is given in reference [5], which indicates that its color-gradient $\boldsymbol{F}_{lm}$ for $N = 2$ is half as long as $\nabla\rho^N$, the phase-field gradient presented in section 3.5[7]: the N-fluid color-gradient is related to ρ^N. We therefore define a two-fluid phase-field ρ^N_{lm}:

$$\rho^N_{lm} = \frac{\rho_l - \rho_m}{\rho_l + \rho_m} \tag{6.24}$$

and because $\rho = \rho_l + \rho_m$ and $\frac{\rho_m}{\rho} = 1 - \frac{\rho_l}{\rho}$:

$$\rho^N_{lm}|_{N=2} = 2\left(\frac{\rho_l}{\rho}\right) - 1 \tag{6.25}$$

which shifted and rescaled to vary between 0 and 1 rather than -1 and 1:

$$\begin{aligned} \rho^{\bar{N}}_{lm} &= \frac{1}{2}\left(\rho^N_{lm} + 1\right) \\ \rho^{\bar{N}}_{lm} &= \left(\frac{\rho_l}{\rho}\right) \end{aligned} \tag{6.26}$$

[5] The cited reference [2] indeed uses an arithmetic average of a phase-field normalized by pure-fluid densities.

[6] In the perturbation step, the same reference interpolates local mixture velocity ***separately*** as $\tau_{\text{eff}} = \sum_k (\rho_k/\rho)\tau_k$. This phase-field-weighted arithmetic average of relaxation times is fortunately equivalent to the density-weighted arithmetic average of the employed phase-field.

[7] See appendix B for the corresponding algebra.

[8] Other publications indeed make interpolation choices, but do not explain ***why*** this interpolation is admissible [2, 5, 7].

[9] Its RGB figures ***imply*** a phase-field, for example, for a red fluid R:

$$R = \frac{\frac{\rho_r}{\rho^0_r}}{\sum_k \frac{\rho_k}{\rho^0_k}} \tag{6.23}$$

whereas pure-fluid density normalization does not appear anywhere in the algorithm: the tracked phase-field is never explicitly defined. Using the same author, the same first author produces RGB figures without normalization by pure-fluid densities in a separate publication [4].

Still for $N = 2$, the color-gradient is, from equation (6.10):

$$\begin{aligned}
\boldsymbol{F}_{lm}|_{N=2} &= \frac{\rho_m}{\rho}\nabla\left(\frac{\rho_l}{\rho}\right) - \frac{\rho_l}{\rho}\nabla\left(\frac{\rho_m}{\rho}\right) \\
&= \left(1 - \frac{\rho_l}{\rho}\right)\nabla\left(\frac{\rho_l}{\rho}\right) - \left(\frac{\rho_l}{\rho}\right)\nabla\left(1 - \frac{\rho_l}{\rho}\right) \\
&= \nabla\left(\frac{\rho_l}{\rho}\right) \\
\boldsymbol{F}_{lm}|_{N=2} &= \nabla\rho_{lm}^{\bar{N}}
\end{aligned} \tag{6.27}$$

indeed showing a relationship between $\boldsymbol{F}_{lm}$ and ρ^N: equation (6.26) is the candidate phase-field of fluid l for the color-gradient in equation (6.10).

This $N = 2$ argument can be extended to $N > 2$. Indeed, since fluids locally form a multicomponent mixture, there is a single local set of macroscopic quantities, including phase-fields, which only depend on local component densities. There are no local interfaces separating components from one another.[10] Additionally, if all components mix locally, then there is no difference between mixing N components with one another, and mixing one component with $N - 1$ components. For example, in defining total density:

$$\begin{aligned}
\rho &= \sum_k \rho_k \\
\rho &= \rho_l + \sum_{\substack{m \\ m\neq l}} \rho_m \\
\rho &= \rho_l + \rho_\mu
\end{aligned}$$

where μ is an index denoting the sum for all local components except l. Therefore, for any fluid l, we can define its phase-field $\rho_l^{\bar{N}}$, starting from equation (6.24) but replacing index m with μ:

$$\begin{aligned}
\rho_l^N &= \rho_{l\mu}^N \\
\rho_l^N &= 2\left(\frac{\rho_l}{\rho}\right) - 1
\end{aligned}$$

$$\boxed{\rho_l^{\bar{N}} = \frac{\rho_l}{\rho}} \tag{6.28}$$

where $\rho_l^{\bar{N}} > 0.5$ marks phase l. We note an important requirement on phase-fields, which equation (6.28) satisfies:

$$\sum_k \rho_k^{\bar{N}} = 1 \tag{6.29}$$

otherwise several phases could be defined at the same lattice node.

Substituting equation (6.28) into the color-gradient $\boldsymbol{F}_{lm}$ we find:

$$\boxed{\boldsymbol{F}_{lm} = \rho_m^{\bar{N}}\nabla\rho_l^{\bar{N}} - \rho_l^{\bar{N}}\nabla\rho_m^{\bar{N}}} \tag{6.30}$$

which directly connects N-fluid CG-LBM to its phase-fields. Equation (6.30) notably implies that alternative phase-fields can also be used.

6.2.1 Normalized phase-fields

For $N = 2$, it is common for the following pure-fluid-density-***normalized*** phase-field to be used when there are density ratios [1, 2, 8]:

$$\rho_{lm}^{Nn} = \frac{\frac{\rho_l}{\rho_l^0} - \frac{\rho_m}{\rho_m^0}}{\frac{\rho_l}{\rho_l^0} + \frac{\rho_m}{\rho_m^0}} \tag{6.31}$$

[10] The interface is tracked implicitly and is only reconstructed later with contours or isosurfaces of phase-field values across several nodes.

This phase-field can be extended to N-fluids by following the same steps that led to equation (6.28):

$$\begin{aligned} \rho_l^{Nn} &= \rho_{l\mu}^{Nn} \\ \rho_l^{Nn} &= \frac{\frac{\rho_l}{\rho_l^0} - \frac{\rho_\mu}{\rho_\mu^0}}{\frac{\rho_l}{\rho_l^0} + \frac{\rho_\mu}{\rho_\mu^0}} \end{aligned} \tag{6.32}$$

and using:

$$\frac{\rho_l}{\rho_l^0} + \frac{\rho_\mu}{\rho_\mu^0} = \sum_k \frac{\rho_k}{\rho_k^0} \tag{6.33}$$

$$\rho_{lm}^{\bar{N}n} = \frac{1}{2}\left(\rho_{lm}^{Nn} + 1\right) \tag{6.34}$$

we indeed find:

$$\boxed{\rho_l^{\bar{N}n} = \frac{\rho_l/\rho_l^0}{\sum_k \rho_k/\rho_k^0}} \tag{6.35}$$

This phase field can be directly used in the expression for the color-gradient in equation (6.30).

Figure 6.1 shows how the non-normalized $\rho_l^{\bar{N}}$ will lead to different interfaces upon initialization depending on the density ratio with surrounding fluid, as the phase-field is biased towards dense fluids. A red droplet's density ρ_r profile is initialized with a $\tanh$ profile with suitable thickness, with value at location $\boldsymbol{x}$ for a droplet of initial radius R_0 and center $\boldsymbol{x}_0$:

$$\rho_R(\boldsymbol{x})|_{t=0} = \frac{1}{2}\rho_r^0\left[1 + \tanh\left(\beta\left(R_0 - |\boldsymbol{x} - \boldsymbol{x}_0|\right)\right)\right] \tag{6.36}$$

where ρ_r^0 is the red pure-fluid density and β is the segregation parameter used in the recoloring step. All simulations are initialized with the same amount of red fluid, and with the same initial density profile. However, the simulation with the non-normalized phase-field $\rho_l^{\bar{N}}$ leads to a droplet that is significantly larger than the initialization radius. Indeed, $\rho_l^{\bar{N}}$ in equation (6.28) leads to variations in phase-field depending on the density ratio across the interface, due to the total density ρ in the denominator, which depends on the density of ambient fluid. Since the blue medium is lighter than the red bubble, smaller amounts of red fluid lead to an interface $\rho_r^{\bar{N}} = 0.5$ marking the droplet interface. This means the segregation operator maintains an interface deeper into the lighter blue medium than it would in for unity density ratio, even though the same mass of fluid is present.[11]

The normalized phase-field in equation (6.31) is not affected by this issue, hence its use when density ratios exist across fluids. Thanks to the discovery of the link between phase-field and N-fluid color gradient in equation (6.30), the normalized phase field can be formulated for N-fluid CG-LBM as $\rho_l^{\bar{N}n}$ in equation (6.35).

6.3 Conclusions

By clarifying the existence of local mixtures between components at a node, we were able to show that mixture speed-of-sound constants, used in colorblind CG-LBM formulations [2, 5], are fully constrained. Mixture viscosity interpolation, however, is free, justifying the investigation of various interpolation methods in the thesis. The choice on which averaging to use can be motivated by performance in different validation cases.

More importantly, the phase-fields for N-fluid CG-LBM were clarified for the first time, and a clear relationship between them and the N-fluid color-gradient was found. This seamlessly allows the use of normalized phase-fields in N-fluid CG-LBM, expanding its reliability at high density ratios λ_ν.

[11] Using the non-normalized phase-field ρ^N (or $\rho^{\bar{N}}$), even when there are density ratios, will ***not*** lead to an incorrect pressure jump across the interface: it is the ***position*** of the interface which will be incorrect, and biased to push towards lighter fluids. CG-LBM is otherwise formulated to generate the pressure jump across the interface, wherever it is defined [7].

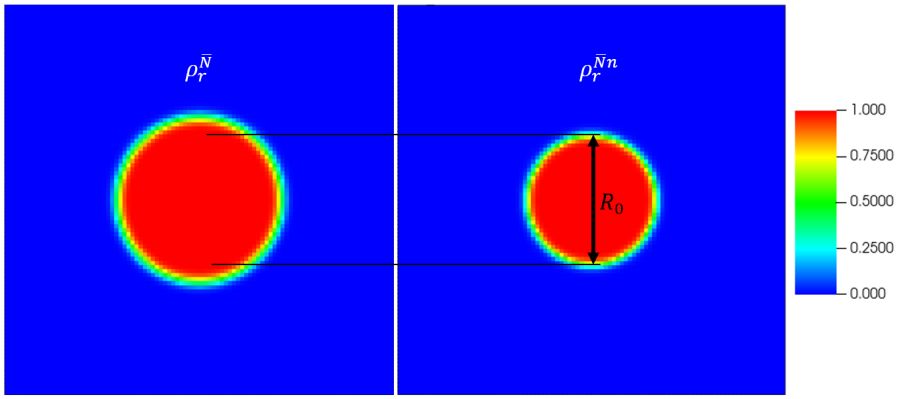

Figure 6.1: Droplet of dense red r fluid initialized in a medium of lighter blue fluid, with density ratio $\lambda_\rho = 1000$. The droplet is initialized with its pure-fluid density with a $\tanh$ interface profile centered around radius R_0. On the left, the interface maintained when using the non-normalized phase-field $\rho_l^{\bar{N}}$. On the right, using a normalized phase-field $\rho_l^{\bar{N}n}$, the effective radius of the droplet identified at $\rho_r^{\bar{N}} = 0.5$ is practically R_0, as this phase-field is more reliable for non-unity density ratios.

The first research question on superviscous fluids in section 5.1.2 has been answered:

Research Questions: Superviscous Particles

- What are the phase-fields for N-fluid CG?

  For a phase-field equivalent to equation (3.42), the phase-field $\rho_l^{\bar{N}}$ varying between 0 and 1 for fluid l is:

  $$\rho_l^{\bar{N}} = \frac{\rho_l}{\rho}$$

  For a pure-fluid-density-normalized phase field $\rho_l^{\bar{N}n}$, appropriate at non-unity density ratios λ_ν:

  $$\rho_l^{\bar{N}n} = \frac{\rho_l/\rho_l^0}{\sum_k \rho_k/\rho_k^0}$$

  Regardless of its particular definition, normalized or not, the phase-fields $\rho_l^{\bar{N}(n)}$ enter the definition of the color-gradient between fluid l and m directly:

  $$\boldsymbol{F}_{lm} = \rho_m^{\bar{N}(n)} \nabla \rho_l^{\bar{N}(n)} - \rho_l^{\bar{N}(n)} \nabla \rho_m^{\bar{N}(n)}$$

- What is the effect of diffuse CG-LBM interfaces on momentum-transfer to s-fluids?
- Could superviscous particles be used in the ink-jet printing regime?

We also note that the new expression for the color-gradient $\boldsymbol{F}_{lm}$ apparently allows us to define phase-fields without defining whole new fluids: fluids can interact directly with phase-fields. This will turn out to

be extremely important in chapter 9, where we will try to have fluids interact with solids using additional perturbation.

Chapter 6 References

[1] Karun Pravin Nirod Datadien. "Directional instabilities in microdroplet jetting: a numerical approach". PhD thesis. Applied Physics and Science Education, Jan. 31, 2024.

[2] Alessandro De Rosis, Rongzong Huang, and Christophe Coreixas. "Universal formulation of central-moments-based lattice Boltzmann method with external forcing for the simulation of multiphysics phenomena". In: *Physics of Fluids* 31.11 (Nov. 2019). doi: 10.1063/1.5124719.

[3] S. Leclaire et al. "Modeling of static contact angles with curved boundaries using a multiphase lattice Boltzmann method with variable density and viscosity ratios". In: *International Journal for Numerical Methods in Fluids* 82.8 (2016). doi: 10.1002/fld.4226.

[4] S. Leclaire et al. "Multiphase flow modeling of spinodal decomposition based on the cascaded lattice Boltzmann method". In: *Physica A: Statistical Mechanics and its Applications* 406 (2014). doi: 10.1016/j.physa.2014.03.033.

[5] Sébastien Leclaire, Marcelo Reggio, and Jean-Yves Trépanier. "Progress and investigation on lattice Boltzmann modeling of multiple immiscible fluids or components with variable density and viscosity ratios". In: *Journal of Computational Physics* 246 (2013). doi: https://doi.org/10.1016/j.jcp.2013.03.039.

[6] Y.K. Lee and K.H. Ahn. "Particle dynamics at fluid interfaces studied by the color gradient lattice Boltzmann method coupled with the smoothed profile method". In: *Physical Review E* 101.5 (2020). doi: 10.1103/PhysRevE.101.053302.

[7] Haihu Liu, Albert J. Valocchi, and Qinjun Kang. "Three-dimensional lattice Boltzmann model for immiscible two-phase flow simulations". In: *Phys. Rev. E* 85.4 (Apr. 2012). doi: 10.1103/PhysRevE.85.046309.

[8] Shimpei Saito et al. "Color-gradient lattice Boltzmann model with nonorthogonal central moments: Hydrodynamic melt-jet breakup simulations". In: *Phys. Rev. E* 98.1 (July 2018). doi: 10.1103/PhysRevE.98.013305.

[9] A. Subhedar. "Color-gradient lattice Boltzmann model for immiscible fluids with density contrast". In: *Phys. Rev. E* 106.4 (Oct. 2022). doi: 10.1103/PhysRevE.106.045308.

[10] A. Subhedar et al. "Interface tracking characteristics of color-gradient lattice Boltzmann model for immiscible fluids". In: *Phys. Rev. E* 101.1 (Jan. 2020). doi: 10.1103/PhysRevE.101.013313.

Part III

Simulations and Results

Chapter 7 | Code Validation

Key Points

- Colorblind CG-LBM was developed for Flow Matters during the thesis.
- The code was validated with steady-state and transient cases, with hydrodynamic and capillary phenomena.

Superviscous Particles in more than one fluid phase would require an N-fluid CG-LBM solver. Separately, Solid-Phase Perturbation may be a practical way to impose contact angles for N fluids without separate boundary conditions. In this chapter, the N-fluid CG-LBM implementation delivered to Flow Matters is documented, along with validation cases.

7.1 The CGN Submbodule

CG-LBM was developed for Flow Matters' C code before the thesis, `lbe-direct`, as part of the work in [3]. These capabilities were expanded during the thesis to support N-fluid CG-LBM, whereas the code was originally limited to $N = 2$. This was done through an optional submodule, `CGN`. The colorblind algorithm from [7], described in section 6.1.1, was implemented to limit memory needs.

The novel pair-wise perturbation step in equation (6.16) is used, halving the number of perturbation operations. phase-fields for fluid l, can be non-normalized $\rho_l^{\bar{N}}$ or normalized $\rho_l^{\bar{N}n}$, per equations (6.28) and (6.35), respectively. phase-fields vary between 0 and 1, with $\rho_l^{\bar{N}} > 0.5$ associated with phase l. Compared to the algorithm in [7], `CGN` explicity uses the relationship between phase-field and color-gradient in equation 6.30. phase-fields are therefore computed separately, and their gradient components (rather than the fractional density gradients) are stored to compute the color-gradient when needed. Local mixture speed-of-sound $\bar{\alpha}$ is always expressed by equation (6.22), but mixture viscosity ν_{eff} can be computed using as harmonic or artihmetic phase-field averages.[1]

Flow Matters' `lbe-direct` code is parallelized, and supports 3D simulations. The standard lattice is D3Q19 [3, 6].

[1] So-called q-averages from reference [7] where implemented:

$$\nu_{\text{eff}} = \left(\sum_k W_i (\nu_k)^q \right)^{1/q} \tag{7.1}$$

where W_i^k is the weight for each fluid, either the phase-field $\rho_k^{\bar{N}(n)}$ or fractional density $\frac{\rho_k}{\rho}$, ν_k is the pure-fluid viscosity of fluid k, and $q \neq 0$ is the averaging variable, with $q = 1$ corresponding to an arithmetic average, and $q = -1$ to a harmonic average. The user can select how to weight the average along with the q value.

7.2 Capturing Surface-Tension

7.2.1 3D $N = 3$ Fluid Laplace Test

Figure 7.1 shows the $N = 3$ Laplace test case, with a (red) droplet/bubble contained within a capsule of another (blue) fluid, itself in contact with background (green) fluid. Across each diffuse $N = 2$ fluid interface, CG-LBM must generate a pressure jump according to equation (2.8). Since the interface is not sharp, neither is the distributed pressure jump, and so the pressure p_l in phase l is measured as the average of points where $\rho_l^{\bar{N}n} \to 1$. *Total* pressure is measured at those points, since fluids form local mixtures, and components indexed $m \neq l$ still contribute to pressure at points $\rho_l^{\bar{N}n} > 0.5$. Therefore, with a single pressure associated with each phase, we compute per equations (3.43) and (6.22):

$$p_l = \left\langle \rho \frac{1 - \bar{\alpha}}{2} \right\rangle \Bigg|_{\left(\rho_l^{\bar{N}n} \to 1\right)} \tag{7.2}$$

where $\langle . \rangle$ is the average operator. Pressure jumps Δp across interfaces are calculated using these phase pressures. The droplet and capsule outer radii are computed from the surface area A of the 0.5 phase-field contours of the red and green phases, respectively:

$$R = \frac{1}{2}\sqrt{A/\pi} \tag{7.3}$$

The in-simulation apparent surface tension σ_{sim} is computed:

$$\sigma_{\text{sim}} = \frac{R}{2}\Delta p \tag{7.4}$$

and is compared to the input surface tension for the fluid-pair corresponding to the interface. All post-processing was done in ParaView. Normalized phase-fields $\rho_l^{\bar{N}n}$ are used. Viscosity interpolation is irrelevant at steady state without fluid motion, and relaxation time $\tau = 1$ is selected for all fluids.

The blue pure-fluid density ρ_b^0 is varied to impose a density ratio across all fluid-fluid interfaces. Simulations are run in a $80 \times 80 \times 80$ domain. The following parameters, in lattice units, remain constant across runs:

- initial red droplet radius 10 ;
- initial blue capsule radius 30 ;
- segregation parameter $\beta = 0.9$;
- fluid-fluid surface tension $\sigma_{lm} = 0.1$.

Densities are initialized with $\tanh$ interface profiles so that interfaces are initialized with as close as possible to a typical CG-LBM fluid-fluid interface.[2] This is the case for all simulations in this thesis, except when stated otherwise.

Table 7.1 shows the tests results after 5000 timesteps, for different pure-fluid densities ρ_r^0, ρ_b^0, and ρ_g^0 of the red, blue, and green fluids, respectively. Each increase in ρ_b^0 correspondingly raises the density ratio across the red-blue (bubble-to-capsule) and blue-green (capsule-to-background) interfaces. The model performs well and consistently for density ratios up to $\mathcal{O}(10^3)$. The larger error on the red-blue interface

[2] Interfaces are initialized according to the expected analytical interface maintained by the recoloring operator [2, 5, 12]. For example, for a fluid l defined up to $x = X$ (i.e., its phase-field drops under 0.5 at X):

$$\rho_l(x, t = 0) = \frac{1}{2}\rho_l^0 \left[1 - \tanh(\beta(x - X)) \right] \tag{7.5}$$

Note the use of β as a "smoothing factor". It is also used to initialized curved features, such as spheres of fluid l of radius R_0 centered about $\boldsymbol{X}$ [9]:

$$\rho_l(\boldsymbol{x}, t = 0) = \frac{1}{2}\rho_l^0 \left[1 + \tanh\left(\beta(R_0 - |\boldsymbol{x} - \boldsymbol{X}|)\right) \right] \tag{7.6}$$

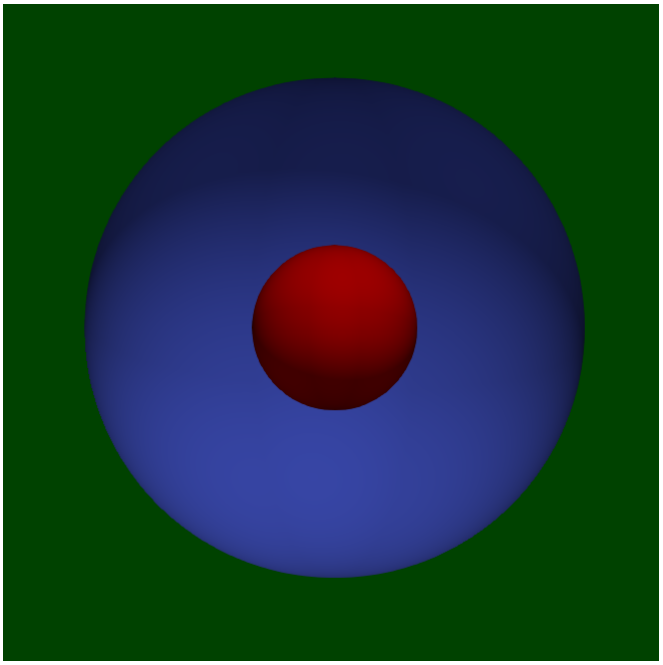

Figure 7.1: $N = 3$ Laplace Test. A red droplet/bubble is contained within a capsule of blue fluid within a green fluid background. The algorithm must handle $N = 3$ fluids, although only $N = 2$ interfaces are present. Phases are identified when respective phase-fields are above 0.5

ρ_r^0	ρ_b^0	ρ_g^0	$\sigma_{\text{sim},rb}$	Relative Error	$\sigma_{\text{sim},bg}$	Relative Error
1	1	1	0.010198	1.98%	0.010094	0.94%
1	100	1	0.010180	1.80%	0.010013	0.13%
1	1000	1	0.010187	1.87%	0.009928	0.72%

Table 7.1: $N = 3$ Laplace Test Results. $\sigma_{\text{sim},rb}$ is the apparent in-simulation surface tension between the red and blue fluids, as evaluated between the droplet and capsule with equation (7.4). Likewise for $\sigma_{\text{sim},bg}$ for the interface between the blue capsule and the green background fluid.

is due to the fact that there are fewer points for which $\rho_r^{\bar{N}(n)} \to 1$, or $\rho_b^{\bar{N}(n)} \to 1$, and those points are for values farther away from 1. Indeed, those phase-fields are constrained on either side and cannot freely increase to 1 (on the inside of the droplet/bubble or capsule).[3] This could be remediated by a larger domain, and larger initialization radii.

The test shows that the algorithm is able to reproduce the correct pressure jump across interfaces defined by the phase-fields. This is the first steady state $N > 2$ result with surface tension ever obtained with Flow Matters' code.

7.3 Capturing Hydrodynamic Behavior

7.3.1 1D $N = 4$ Steady-State Couette Flow

Figure 7.2 shows the diagram for $N = 4$ Couette Flow.

Figure 7.3 shows the velocity profile for a 1D Couette flow with $N = 4$ in a 64 node wide domain after 10^6 timesteps. Fluid-fluid interfaces are visible as velocity discontinuities in the analytical profile. Simulation parameters are, in lattice units:

- individual fluid layer are initialized $L = 16$ nodes thick;

[3] The phase-field profile does not have the "space" to approach 1 as it does in the background fluid.

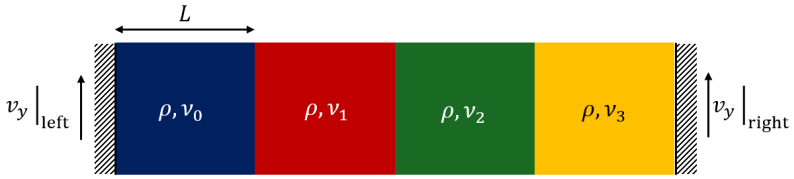

Figure 7.2: $N = 4$ Couette Flow Diagram. Fluid layers are accelerated by momentum diffusing from the moving boundaries.

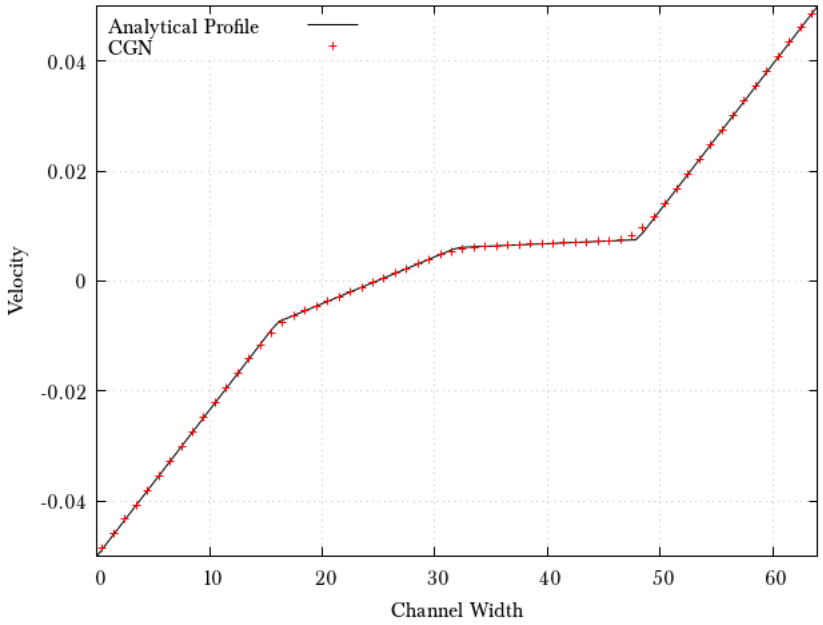

Figure 7.3: Results for $N = 4$ Steady State Couette Flow, unity density ratio, variable viscosity ratios.

- unity density ratio across all fluids with $\rho = 1$;
- left wall velocity $v_y|_{\text{left}} = -0.05$;
- right wall velocity $v_y|_{\text{right}} = 0.05$;
- segregation parameter $\beta = 0.9$;
- no surface tension between fluids $\sigma = 0$.[4]

From left to right, in each 16-node layer, pure-fluid viscosities ν_i for fluids indexed i are:

- $\nu_0 = 1/300$;
- $\nu_1 = 1/96$;
- $\nu_2 = 1/10$;
- $\nu_3 = 1/300$.

Local viscosity ν_{eff} is computed as the phase-field-weighted harmonic average of the pure-fluid viscosities.

The analytical solution is obtained using momentum diffusion circuits (see appendix C), analogously to heat transfer circuits [1]. This technique yields a momentum diffusion resistance $R_{\nu,i} = \frac{L}{\mu_i}$ in the i fluid layer, where $\mu_i = \rho\nu_i$ is the fluid's dynamic viscosity. The total resistance allows us to define the Reynolds number for the entire flow, with characteristic velocity $\mathcal{U} = v_y|_{\text{right}} - v_y|_{\text{left}}$:

$$\begin{aligned} \text{Re} &= \frac{\rho\mathcal{U}\mathcal{L}}{\mu} = \rho\mathcal{U}(R_\nu)|_{\text{total}} \\ &= \rho\mathcal{U}\sum_i \frac{L}{\rho\nu_i} \\ \text{Re} &= 1129.6 \end{aligned}$$

Numerical results are very close to the analytical profile. Small discrepancies near the interfaces are attributable to the diffuse interface viscosity averaging.

This is the first $N > 2$ steady state hydrodynamic result with non-zero velocity profile ever obtained with Flow Matters' code.

7.3.2 1D $N = 2$ Transient Couette Flow

Figure 7.4 shows the solution for 1D transient Couette flow at various timesteps in a $H = 64$ node wide domain. Parameters are, in lattice units:

- prescribed velocity on right-hand wall $U = 0.1$;
- fluid viscosity is $\nu = 0.128$;
- fluid density is $\rho^0 = 1$.

This leads to a viscous timescale $\tau_\mu = H^2/\nu = 32000$ and a Reynolds number $\text{Re} = 50$.

The numerical solution is compared to a known analytical solution [11], with which we observe good agreement. Small discrepancies for the earliest represented timestep can be attributed to the sharpness of the velocity profile compared to a small number of nodes: lattice resolution is perhaps slightly too low. This does not harm the development of the solution at later timesteps.

This validation case is supplied to confirm the submodule's ability to reproduce transient hydrodynamics, rather than showcase any new capability.

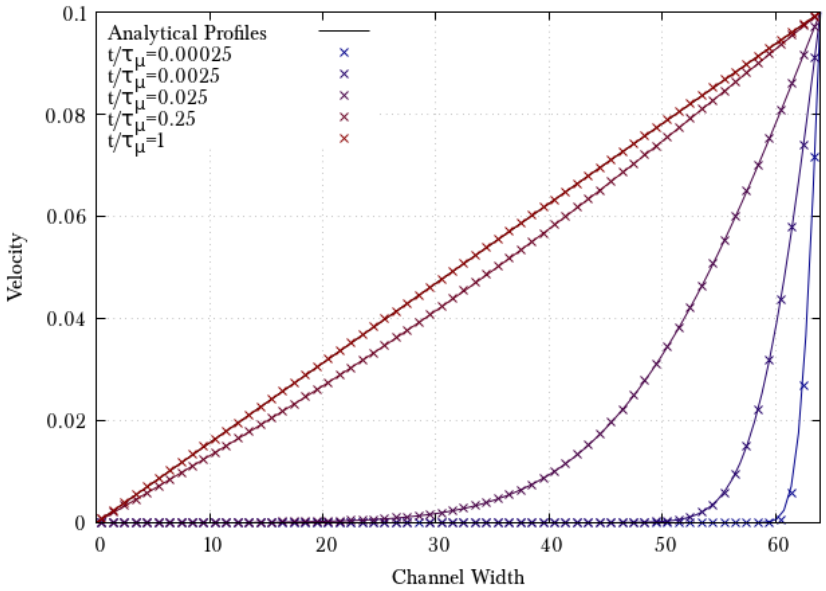

Figure 7.4: Single-Phase Transient Couette Flow Results, $Re = 50$.

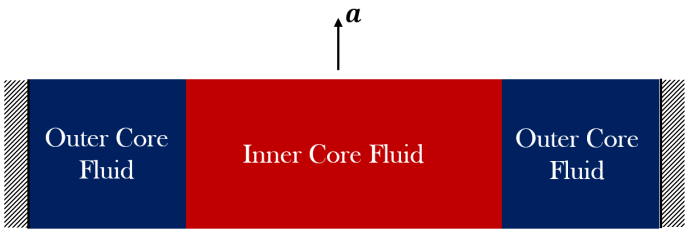

Figure 7.5: $N = 2$ Poiseuille Flow Diagram. The flow is driven by a gravitational acceleration a. No-slip applies at the fixed walls at the boundaries.

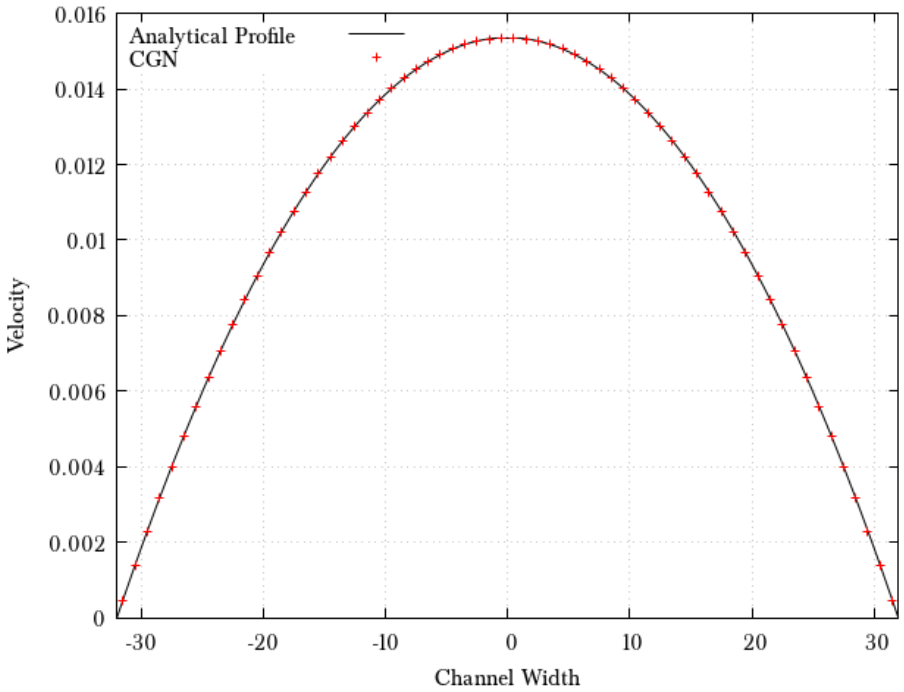

Figure 7.6: $N = 2$ Steady-State Poiseuille Flow for Unity Viscosity Ratio.

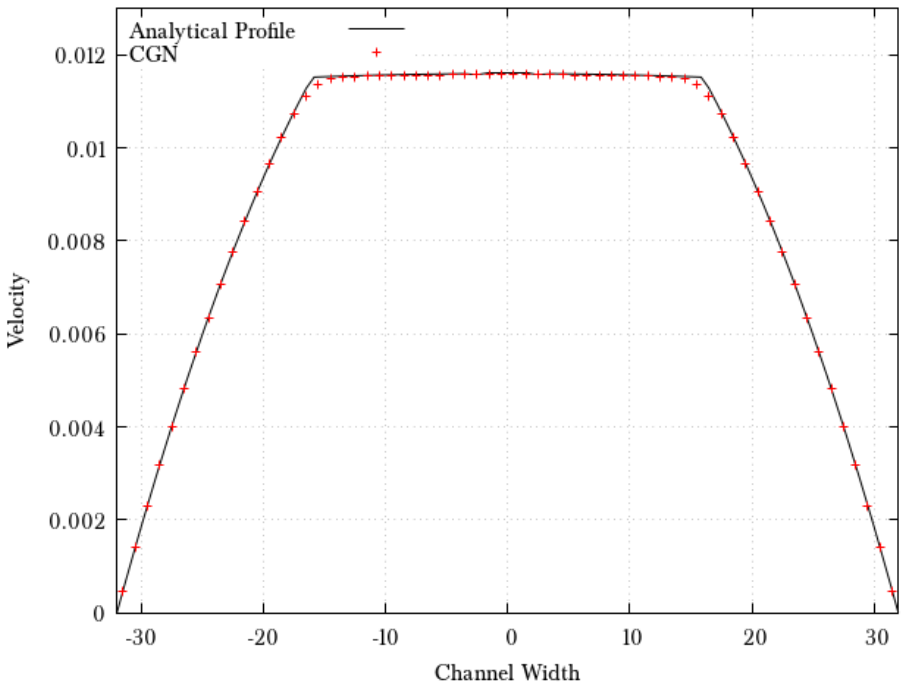

Figure 7.7: $N = 2$ Steady-State Poiseuille Flow for Viscosity Ratio $\lambda_\nu = 50$ with more viscous inner core.

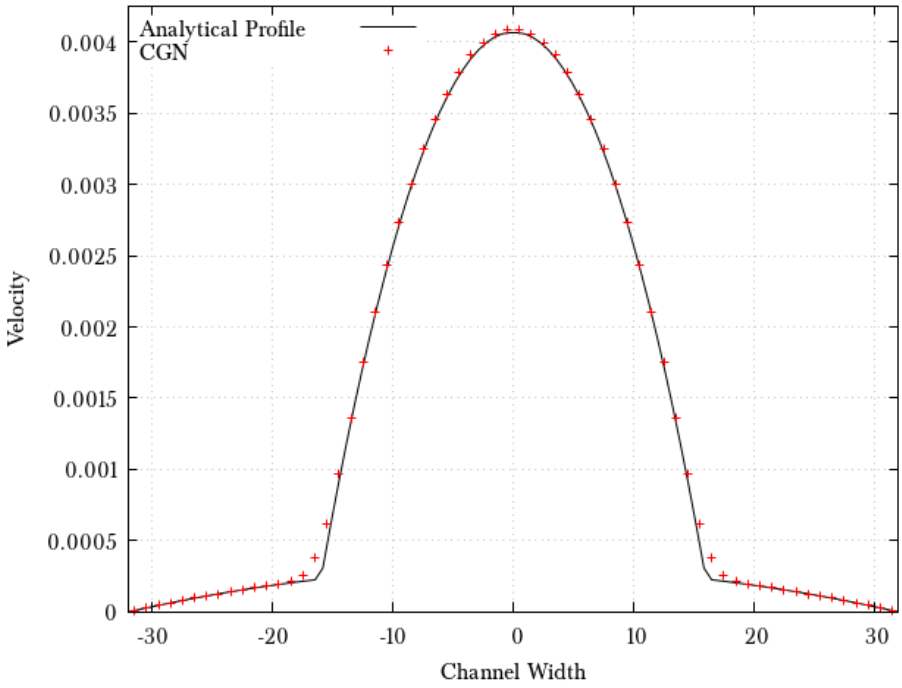

Figure 7.8: $N = 2$ Steady-State Poiseuille Flow for Viscosity Ratio $\lambda_\nu = 50$ with more viscous outer core.

7.3.3 1D $N = 2$ Steady-State Poiseuille Flow

Figure 7.5 shows the diagram for $N = 2$ Poiseuille Flow with inner and outer cores of different fluids.

Figures 7.6, 7.7, and 7.8 show the velocity profiles for $N = 2$ Poiseuille flow at unity density ratio, and respectively unity viscosity ratio, viscosity ratio $\lambda_\nu = 50$ with a more viscous inner core, and viscosity ratio $\lambda_\nu = 50$ with a more viscous outer core, in a 64-node wide domain. The flow is force-driven, with a gravitational acceleration a in the streamwise direction. Guo forcing from section 3.3.4 is used. Parameters are, in lattice units:

- inner core is initialized 32 nodes wide;
- fluid densities are $\rho = 1$;
- when the viscosity ratio is $\lambda_\nu = 1$, fluid viscosities are $\nu = 1/300$;
- when $\lambda_\nu = 50$, the most viscous fluid has viscosity $\nu = 1/6$;
- gravitational acceleration is $a = 10^{-7}$;
- segregation parameter is $\beta = 0.9$;
- no surface tension between fluids $\sigma = 0$.

Local viscosity ν_{eff} is computed as the phase-field-weighted harmonic average of the pure-fluid viscosities. Non-normalized phase-fields $\rho_l^{\bar{N}}$ are used. Fluid-fluid interfaces on the figures coincide with the velocity discontinuities on the analytical profiles.

The numerical solution is compared to a known analytical solution, following a publication with this very validation case [10]. Small discrepancies in the interface region are attributable to the diffuse interface and viscosity averaging.

This validation case is supplied to introduce the submodule's ability to support viscosity ratios, rather than showcase any new capability.

[4]The recoloring operator indeed keeps phases separate entirely separately from the perturbation operator. No surface tension is required to keep phases separate.

7.4 Central Moments and Extended Equilibria

Central Moments and Extended Equilibria were also implemented for the `CGN` submodule. Fortunately, as described in 6.1.1, both can be implemented by directly acting on the total populations f_i and the total density ρ. Central Moments are implemented as in the original CG-LBM code, on a D3Q27 lattice [3, 4, 6].

7.4.1 1D Steady-State $N = 2$ Couette Flow with Density Ratios

CG-LBM without Extended Equilibria is not able to capture momentum discontinuities resulting from density gradients across interfaces. Figures 7.9, 7.10, and 7.11 reproduce a validation case from [8], where, respectively:

- case LD-LV with density ratio $\lambda_\rho = 2$ and viscosity ratio $\lambda_\nu = 2$;
- case MD-MV with $\lambda_\rho = 20$ and $\lambda_\nu = 20$;
- case HD-HV with $\lambda_\rho = 1000$ and $\lambda_\nu = 100$.

Note that figures plot ***momentum*** profiles, accounting for both local density and velocity, across a 160-node domain. Fluid-fluid interfaces coincide with discontinuities in the analytical profile. The following parameters are used, in lattice units:

- each fluid layer is initialized 80-nodes thick;
- the lighter fluid's density is $\rho_{\text{min}} = 1$;
- the least viscous fluid's viscosity is $\nu_{\text{min}} = 1/2$;
- the left wall velocity is $v_{\text{wall}} = 0.0001$;
- the right wall velocity is $v_{\text{wall}} = -0.01$;
- the segregation parameter is $\beta = 0.9$;
- no surface tension between fluids $\sigma = 0$.

Local viscosity ν_{eff} is computed as the phase-field-weighted harmonic average of the pure-fluid viscosities. Fluid-fluid interfaces on the figures coincide with the velocity discontinuities on the analytical profiles.

Although there are rather significant differences between the numerical results and the analytical profiles, the momentum profile is able to transition quickly across the interface.[5] We note that the differences with the analytical profile closely follow (if they are not identical) to those in [8], where this validation originates from. How well Extended Equilibria reproduce momentum discontinuities arising from density ratios is very flow-dependent, and the figures do not suggest that Extended Equilibria perform better

[5] Without Extended Equilibria, CG-LBM completely fails to capture momentum discontinuities arising from density ratios [8].

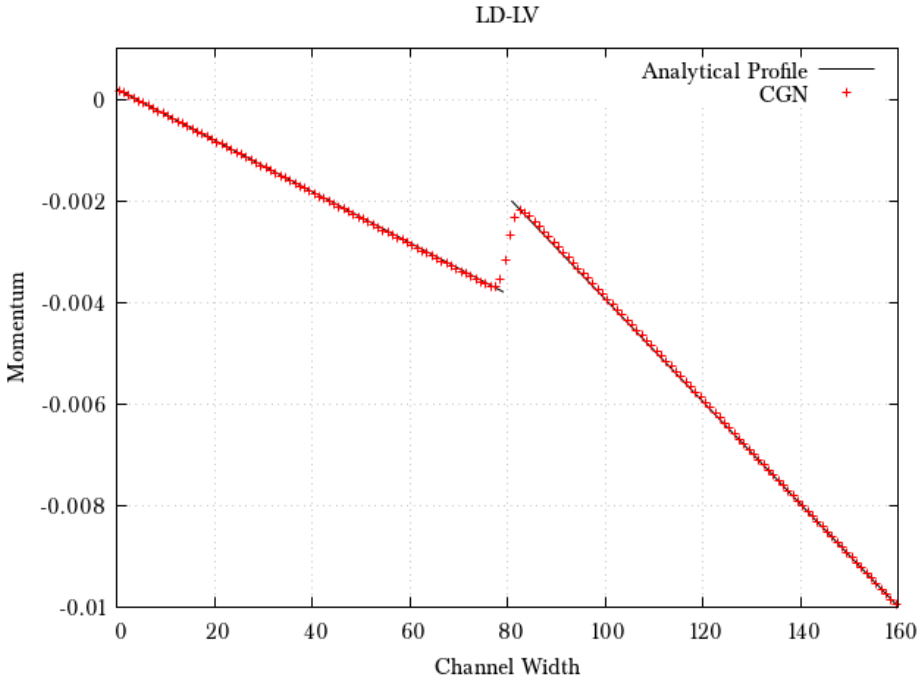

Figure 7.9: $N = 2$ Steady-State Couette Flow for case LD-LV.

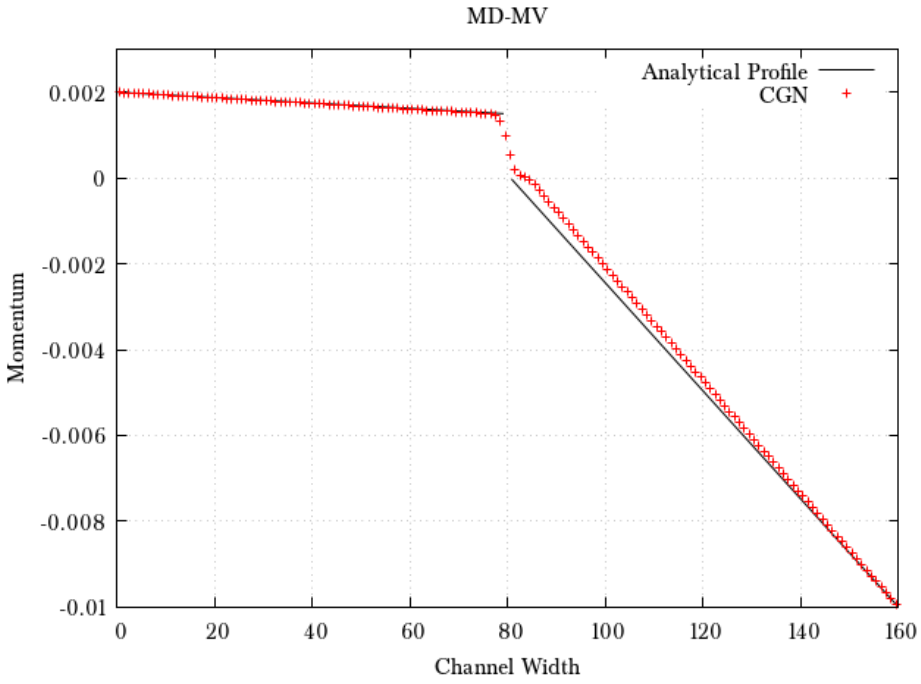

Figure 7.10: $N = 2$ Steady-State Couette Flow for case MD-MV.

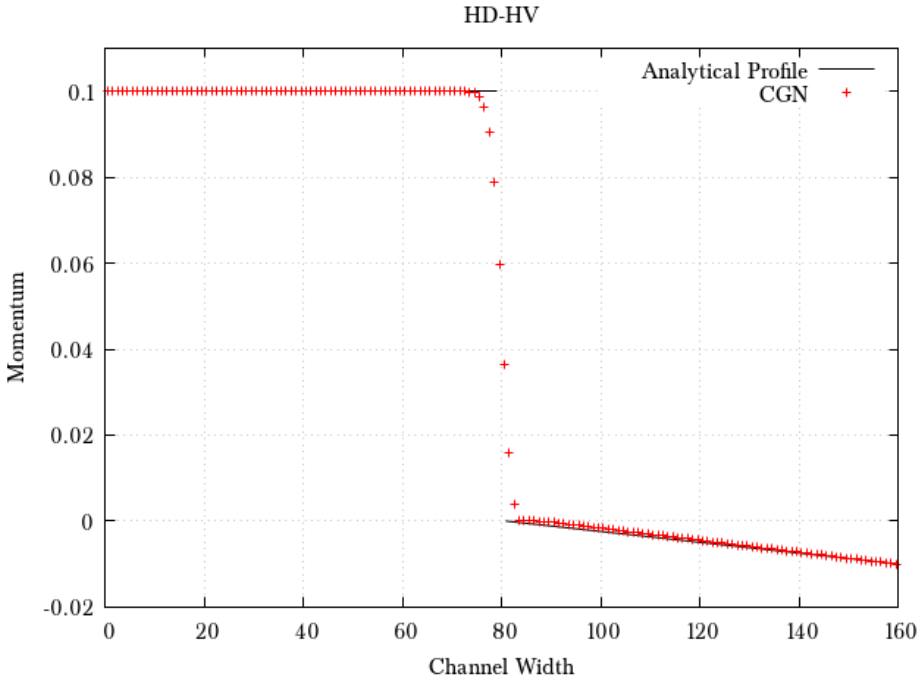

Figure 7.11: $N = 2$ Steady-State Couette Flow for case HD-HV.

7.4.2 3D $N = 2$ Ligament Contraction

Figure 7.12 shows the ligament contraction case, chosen from [3]. A long ligament capped by hemispheres of radius R_0 is initialized, and contracts into a sphere under the effect of surface tension. The ligament half-length $x(t)$ is measured from the midplane to the end of the ligament. This case was selected to validate the `CGN` submodule in dynamic conditions with viscous and capillary behavior, against the original `CG` submodule developed before the start of the thesis.

Simulation parameters are, in lattice units, for both the `CG` and `CGN` runs:

- fluid densities $\rho = 1$;
- ligament fluid viscosity $\nu_0 = 1/6$;
- background fluid viscosity $\nu_1 = 1/6000$;[6]
- initial capsule radius is $R_0 = 12$;
- initial ligament length (excluding the hemispheric caps) is $L = 100$.
- segregation parameter is $\beta = 0.5$;
- surface tension is $\sigma = 0.05$;

These parameters lead to a capillary timescale $t_{\text{cap}} = \sqrt{\rho R_0^3/\sigma} = 185.9$.

Figure 7.13 shows that the new `CGN` produces the same results as the extensively validated original `CG` code from [3]. Even in this $N = 2$ case, the `CGN` submodule uses the colorblind algorithm, which is structured very differently from the original `CG`. Since colorblind formulations are meant to be strictly mathematically equivalent to non-colorblind CG-LBM, figure 7.13 confirms there are no accidental differences across algorithms.

[6] Note the viscosity ratio is $\lambda_\nu = 10^3$, with background fluid relaxation time $\tau_1 = 0.5005$, which would not be stably accessible without Central Moments.

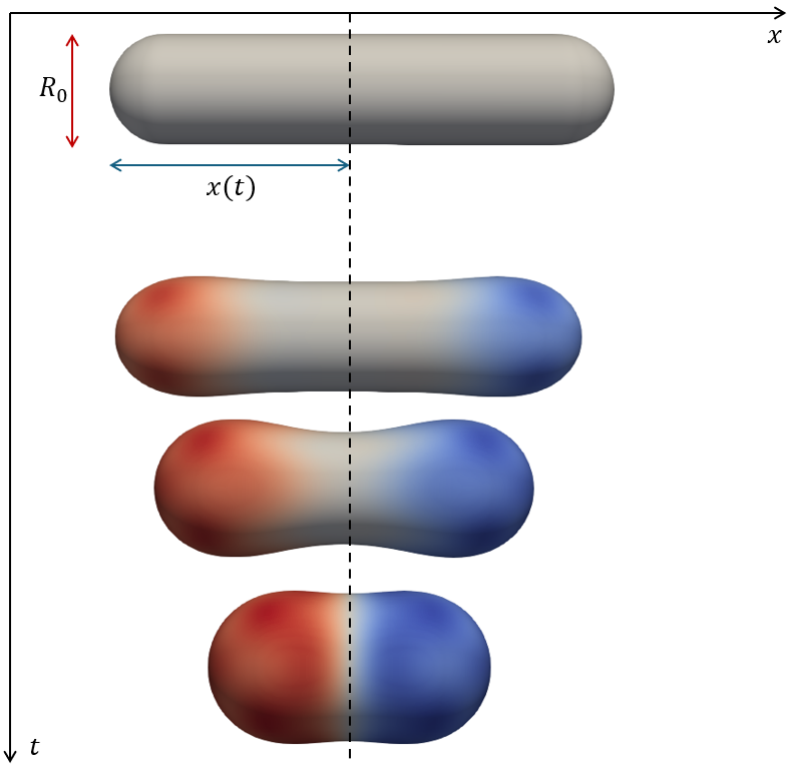

Figure 7.12: 3D $N = 2$ Ligament Contraction Case Diagram. The ligament contracts under the effect of surface tension. Red color qualitatively chose rightward local velocity, blue leftward.

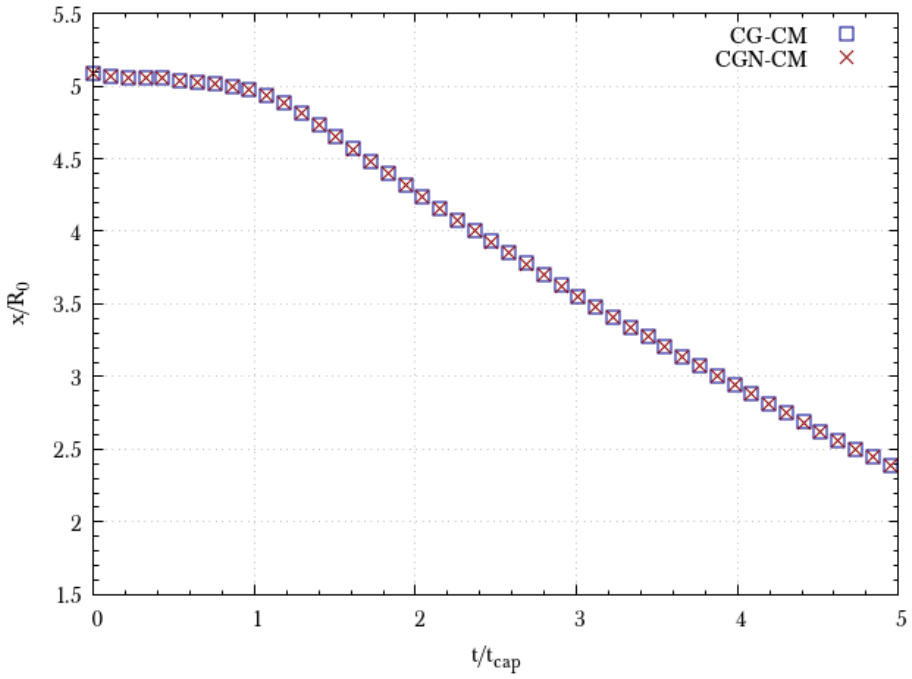

Figure 7.13: 3D $N = 2$ Ligament Contraction Results from the new CGN submodule against the original CG code.

Chapter 7 References

[1] Theodore L. Bergman et al. *Fundamentals of Heat and Mass Transfer*. 8th ed. 1 online resource (1045 pages) vols. New York: Wiley, 2017.

[2] K. Burgin et al. "Kinematics of chromodynamic multicomponent lattice Boltzmann simulation with a large density contrast". In: *Phys. Rev. E* 100.4 (Oct. 2019). doi: 10.1103/PhysRevE.100.043310.

[3] Karun Pravin Nirod Datadien. "Directional instabilities in microdroplet jetting: a numerical approach". PhD thesis. Applied Physics and Science Education, Jan. 31, 2024.

[4] Alessandro De Rosis, Rongzong Huang, and Christophe Coreixas. "Universal formulation of central-moments-based lattice Boltzmann method with external forcing for the simulation of multiphysics phenomena". In: *Physics of Fluids* 31.11 (Nov. 2019). doi: 10.1063/1.5124719.

[5] I. Halliday, A. P. Hollis, and C. M. Care. "Lattice Boltzmann algorithm for continuum multicomponent flow". In: *Phys. Rev. E* 76.2 (Aug. 2007). doi: 10.1103/PhysRevE.76.026708.

[6] Timm Krüger et al. *The Lattice Boltzmann Method: Principles and Practice*. Graduate Texts in Physics. Springer, 2016.

[7] Sébastien Leclaire, Marcelo Reggio, and Jean-Yves Trépanier. "Progress and investigation on lattice Boltzmann modeling of multiple immiscible fluids or components with variable density and viscosity ratios". In: *Journal of Computational Physics* 246 (2013). doi: https://doi.org/10.1016/j.jcp.2013.03.039.

[8] Sébastien Leclaire et al. "Enhanced equilibrium distribution functions for simulating immiscible multiphase flows with variable density ratios in a class of lattice Boltzmann models". In: *International Journal of Multiphase Flow* 57 (2013). doi: https://doi.org/10.1016/j.ijmultiphaseflow.2013.07.001.

[9] Y.K. Lee and K.H. Ahn. "Particle dynamics at fluid interfaces studied by the color gradient lattice Boltzmann method coupled with the smoothed profile method". In: *Physical Review E* 101.5 (2020). doi: 10.1103/PhysRevE.101.053302.

[10] A. Montessori et al. "Mesoscale modelling of near-contact interactions for complex flowing interfaces". In: *Journal of Fluid Mechanics* 872 (June 2019). doi: 10.1017/jfm.2019.372.

[11] C. Pozrikidis. *Introduction to theoretical and computational fluid dynamics*. New York: Oxford University Press, 1997.

[12] T. J. Spencer, I. Halliday, and C. M. Care. "Lattice Boltzmann equation method for multiple immiscible continuum fluids". In: *Phys. Rev. E* 82.6 (Dec. 2010). doi: 10.1103/PhysRevE.82.066701.

Chapter 8 | Superviscous Fluids

Key Points

- CG-LBM superviscous fluids' effect on surrounding flow depends on viscosity interpolation in the interface region.
- The CG-LBM recoloring operator can catastrophically deform superviscous fluid particles depending on initialization.
- CG-LBM superviscous fluids are not recommended for the ink-jet printing regime.

In this chapter, we investigate the use of superviscous fluids (s-fluids) to model solid particles. As s-fluid viscosity grows, resistance to shear deformation increases, and applied forces should increasingly go to other mechanical degrees of freedom. Indeed, when viscosity tends towards infinity, a force applied to the surface of the s-fluid generates a momentum change that is instantaneously diffused throughout the whole phase, and induces solid-body-like linear or rotational motion.

As CG-LBM users, our interest is in mediating wetting on the s-fluids' surfaces with perturbation with surrounding fluids according to equation (6.16). The use of superviscous fluids in CG-LBM introduces at least two unusual features:

- particles formed with s-fluid now have a diffuse interface;
- this interface is maintained by the recoloring operator of equation (6.15).

The diffuse interface can cause viscosity-interpolation-dependent wall positions or slip, but can still prove useful for small, light particles. The recoloring operator, however, can generate forces that have no physical basis and yet deform particles of s-fluid.

8.1 Effects of the Diffuse Interface on Momentum Transfer

CG-LBM phase-field interfaces are diffuse, and local viscosity must be interpolated. Differences between pure-fluid and local mixture viscosities, which are interpolation-dependent, can affect the flow field [3]. Phase-field-weighted arithmetic and harmonic averages of pure fluid viscosities are typical choices for mixture viscosities [2, 3], and are investigated in this section. Figure 8.1 shows the steady-state result for a 1D $N = 2$ Couette flow with a viscosity ratio $\lambda_\nu = 100$. The domain is separated into two equal-width fluid layers. A Reynolds number of $\mathrm{Re} = 20$ is obtained by assuming all viscous dissipation occurs in the least viscous fluid layer (to the left). The harmonic averaging of fluid kinematic viscosities in the diffuse interface leads to a better match with the analytical solution. The difference in results is directly caused by the choice in viscosity averaging.

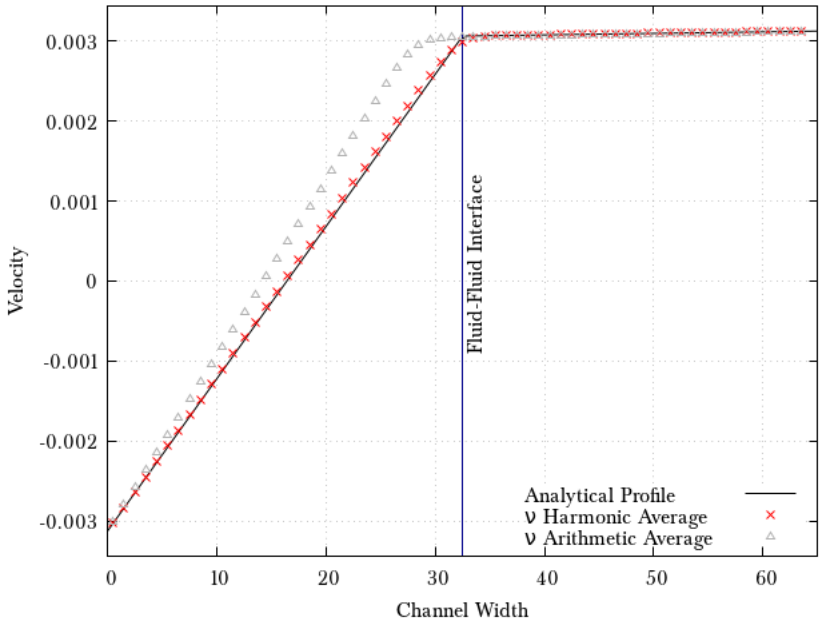

Figure 8.1: Simulation Results for 1D $N = 2$ Steady State Couette Flow with Reynolds Number Re $= 20$ and viscosity ratio $\lambda_\nu = 100$ (more viscous fluid to the right). LBM simulation solutions with either harmonic or arithmetic averaging of viscosities. Viscosity interpolation at higher viscosity ratios can significantly affect the flow, especially when arithmetic averaging is used.

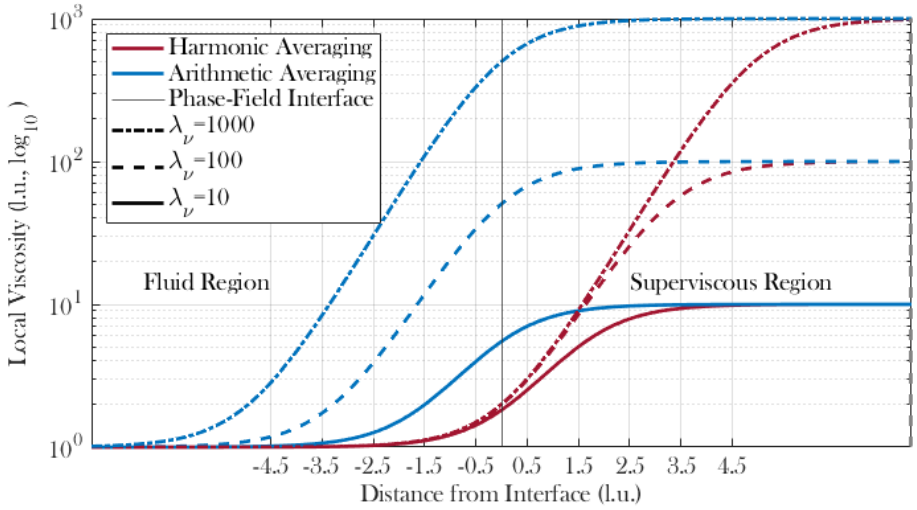

Figure 8.2: Local Viscosity across a Fluid/S-Fluid Interface at different viscosity ratios λ_ν and for harmonic or arithmetic averaging of pure-fluid viscosities. Solid vertical line represents the position of the interface. Segregation parameter $\beta = 0.7$.

8.1.1 Viscosity across a CG-LBM Interface

Figure 8.2 shows local viscosity across a planar interface at different viscosity ratios. The lower viscosity region is the fluid region, and the higher viscosity region is the superviscous region. The plot is continuous, as the phase-fields $\rho_f^{\bar{N}}$ and $\rho_S^{\bar{N}}$, respectively of the fluid and solid regions, are computed from the expected analytical $\tanh$ profile maintained by the recoloring operator for $\beta = 0.7$, centered at the origin:

$$\rho_f^{\bar{N}} = \frac{1}{2}\left(1 + \tanh(\beta x)\right)$$
$$\rho_S^{\bar{N}} = 1 - \rho_f^{\bar{N}}$$

The lower x-axis is defined in lattice units, and plot readings spaced by 1 on this axis correspond to node-to-node differences in corresponding CG-LBM simulations. We observe that:

- arithmetic averaging consistently contaminates the fluid side of the interface with the higher s-fluid viscosity;[1]
- harmonic averaging consistently contaminates the superviscous side of the interface with the lower fluid viscosity.

However, every increase in order in viscosity ratio λ_ν leads to:

- for arithmetic averaging, an increase in order in local viscosity in the fluid region very close to the interface;
- for harmonic averaging, very small changes in local viscosity in the superviscous region very close to the interface.

This suggests that arithmetic averaging will increasingly affect the flow for every increase in s-fluid viscosity, whereas harmonic averaging isolates changes to the superviscous region. This will be in fact confirmed in the following test case, and mark harmonic averaging as preferable for s-fluid applications.

8.1.2 S-Fluid Particle in Shear Flow

S-fluids shear continuously, and must therefore be given different degrees of freedom to convert applied forces into motion approaching that of a solid body, rather than shear dissipation. A simple 1D case was used to study the conversion of shear forces into linear momentum, and the effects of viscosity averaging. For light particles in shear flow, harmonic viscosity averaging was shown to model solid response to flow well. Arithmetic averaging on the other hand leads to significant change in the flow field in the fluids.

The Accelerated Slab Test Case

Figure 8.3 shows a test case for the acceleration of a particle under shear flow: 1D $N = 1$ Couette flow with an accelerated wall. A fixed velocity U is set on the left-hand wall. Due to fluid viscosity ν_f, momentum diffuses across the H-wide profile to the right-hand wall, which is accelerated by viscous shear forces. This flow is equivalent to the acceleration of a slab in a channel shear flow, shown in figure 8.4. When shear forces reach the right-hand wall, they are transferred to the rigid slab and converted to linear momentum. By the continuity of momentum flow at this boundary, we indeed have:

$$-\rho_f \nu_f \left.\frac{\partial u}{\partial x}\right|_{x=H} = L\rho_S \frac{dV_{\text{wall}}}{dt} \tag{8.1}$$

where ρ_f and ν_f are respectively fluid density and viscosity, u is the flow velocity, V_{wall} is the velocity of the right-hand wall, L is the half-length of the 1D solid slab, and ρ_S is the solid density. As shown in

[1] The effect or arithmetic averaging explains the discrepancy in figure 8.1: the large viscosity from the high-viscosity region bleeds into the low-viscosity region and significantly increases resistance to shear close to the interface, leading to more shear dissipation to occur in the low viscosity region farther away from the interface.

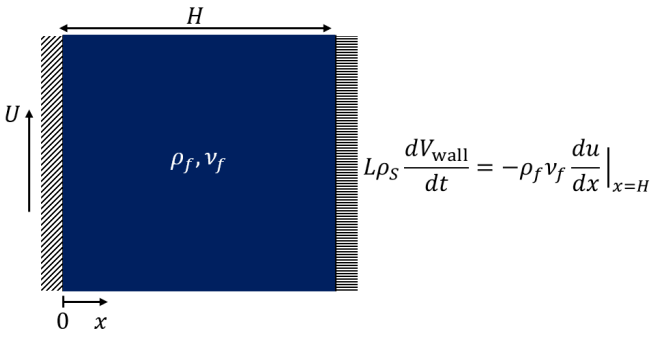

Figure 8.3: 1D $N = 1$ Couette Flow with Accelerated Wall. The left wall moves at constant velocity U, whereas the right wall is progressively accelerated by the flow. This is the 1D approximation of the acceleration of a solid slab by a shear flow in a channel, shown in figure 8.4.

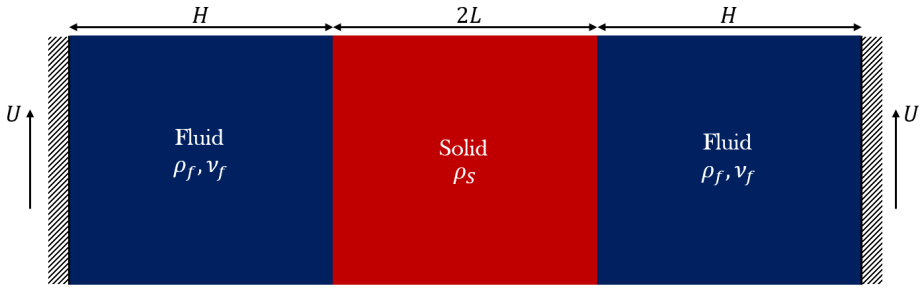

Figure 8.4: Solid Slab Acceleration in Couette Flow. A slab is located in the center of a channel, and is accelerated by momentum diffusing across the fluid layers.

appendix D, this boundary defines the following slab acceleration timescale t_a:

$$t_a = \frac{\rho_S H L}{\rho_f \nu_f} \tag{8.2}$$

Appendix D also shows how benchmark results are obtained with a Finite Difference (FD) method.

As shown in figure 8.5, this case can also be run in a CG-LBM simulation with an s-fluid modeling the solid slab. The equivalent slab acceleration case is symmetrical about the axis cutting the slab into two halves, and the right-hand wall is now a free-slip boundary condition. Either phase is initialized with a CG-LBM $\tanh$ profile with $\beta = 0.7$ segregation parameter. There is no surface tension between the fluids. The s-fluid is sheared by the fluid at the interface, but its high viscosity converts shear forces into momentum, which is distributed across the entire slab.

To approach a case relevant to the inkjet printing regime, we set:

- a Reynolds number $\text{Re}_f = 100$ in the fluid region, matching the upper range of inkjet printing values [5];
- an s-fluid half-length $L = H/2$ half the fluid region's characteristic lengthscale;
- unity density ratio between the s-fluid and the fluid.

Using a fluid region $H = 32$-nodes long, the Reynolds number and fluid viscosity set the left-wall velocity U. The next two settings lead to the following dimensionless quantity, scaling with the ratio of phase masses (in lattice units):

$$\frac{\rho_f H}{\rho_S L} = \frac{1 \cdot 32}{1 \cdot 16} = 2 \tag{8.3}$$

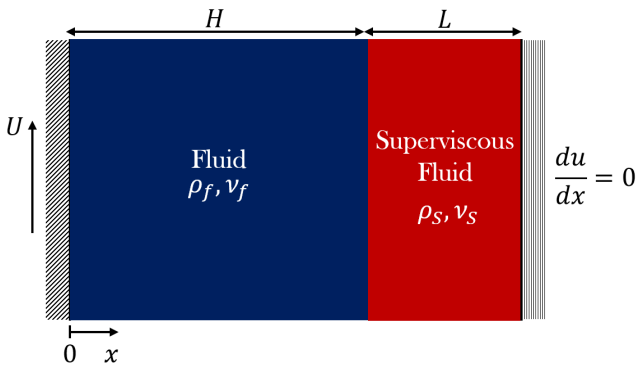

Figure 8.5: 1D $N = 1$ Couette Flow with Accelerated Wall, using an s-fluid. The half-slab of length L is now part of the simulation domain.

Compare this with the ratio obtained from parameters used in the mobile particle jetting simulations in [1] (where a particle of radius $R_p = D_p/2$ is present in the nozzle of radius R_{nozzle}, and using fluid properties of the ink present in the nozzle):

$$\frac{\rho_f}{\rho_S} \cdot \frac{R_{\text{nozzle}}}{R_p} = \frac{1}{2.3} \cdot \frac{15\mu\text{m}}{6.67\mu\text{m}/2} = 1.96$$

Therefore, dimensionless quantities are matched for inkjet printing. It should be noted, however, that the current test case is a pure shear flow, which the full jetting simulation is not. The case is characterized by a ratio of viscous timescale in the fluid phase t_ν to the particle acceleration timescale t_a:

$$\frac{t_\nu}{t_a} = \frac{H^2/\nu_f}{\frac{\rho_S HL}{\rho_f \nu_f}} = \frac{\rho_f H}{\rho_S L} = 2 \tag{8.4}$$

which we note is the same as the ratio of masses in equation 8.3 for this shear flow.

Physically, the fact that $t_a < t_\nu$ means that the solid will be very responsive to the flow. Indeed, the smaller this effective particle response time t_a, the more similar the boundary between the fluid and the solid is to a free-slip wall. This means that larger ratios in equation (8.4) lead to less shear stress at the interface to be distributed across the s-fluid. The current regime is suited for s-fluid simulations, since shear will be limited. The distribution of applied shear stresses and its conversion into rigid-body-like momentum is ensured by the viscosity ratio λ_ν between the s-fluid and actual fluid. Clearly, the viscous timescale in the s-fluid L^2/ν_s (where ν is the s-fluid viscosity) must be very short compared to either t_ν or t_a in order to diffuse momentum across the s-fluid without interfering with physical timescales.

Viscosity-Interpolation Effective Wall Position

Figure (8.6) shows the wall velocity response over time for CG-LBM with s-fluids. Wall velocity is measured at the phase-field interface between the fluid and s-fluid. Local viscosity is computed with arithmetic averaging. With every increase in viscosity ratio λ_ν, we observe a *faster*-than-expected particle response time, when compared to the FD benchmark. Indeed, due to the arithemtic averaging of viscosities, increases in λ_ν leads to significant increases in viscosity in the fluid region close to the interface, as explained by figure 8.2. This pushes the effective extent of the superviscous layer (and hence the effective accelerated wall position) into the fluid. The region where viscosity is on the order of that of the pure fluid becomes narrower, raising the shear rate and hence the shear accelerating the s-fluid, quickening the convergence to U.

The effective wall position can be found by finding the position of the sharpest velocity discontinuity in the CG-LBM simulation. This is measured after the diffusing momentum reaches the s-fluid and begins to accelerate it, and does not vary over time after $t/t_a \sim 0.2$. Indeed, once the acceleration of the wall is underway, this effective wall position is determined by the phase-field interface profile and local viscosity,

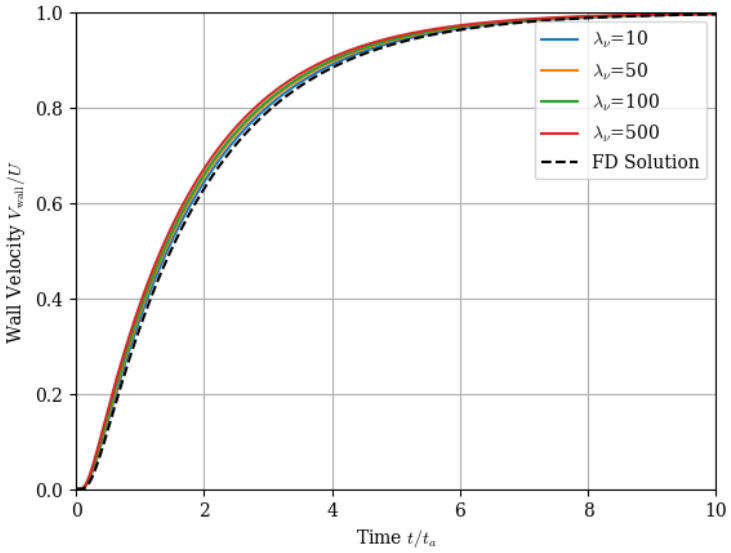

Figure 8.6: Solid Wall Velocity V_{wall} over Time for Different Viscosity Ratios λ_ν, with Arithmetic Viscosity Averaging for CG-LBM. FD benchmark measured at the right-hand simulation boundary. LBM results measured at the phase-field boundary between fluid and s-fluid layers.

λ_ν	**Node with Maximum $\partial^2 u/\partial x^2$**	**Distance From Interface**
10	29	2.5
50	28	3.5
100	27	4.5
500	26	5.5

Table 8.1: Node with Maximum $\partial^2 u/\partial x^2$ after momentum diffusion reaches the s-fluid, a proxy for effective accelerated wall position, for the CG-LBM simulations with arithmetic averaging. The fluid/s-fluid interface is actualy located between the 31st and 32nd nodes.

which is constant through time. The sharpest discontinuity is coarsely measured as the node where $\partial^2 u/\partial x^2$ is maximum. Table 8.1 shows how each increase in viscosity pushes the effective wall position towards the fluid phase-field, away from the actual interface. Clearly, for a case roughly representative of inkjet printing, arithmetic viscosity averaging causes significant changes in the flow in the fluid-phase.

Figure 8.7 shows the same s-fluid response, but using harmonic viscosity averaging. The s-fluid response times are very close to the FD benchmark. CG-LBM response curves are practically indistinguishable from each other, and the s-fluid predicts the solid particle response at even very moderate viscosity ratio. CG-LBM curves are so similar because very close to the interface, increases in viscosity ratio are barely felt under harmonic averaging (see figure 8.2).

From this, we conclude even very mild viscosity ratios are sufficient for the s-fluid to emulate a solid accelerated slab's response to the shear flow. This is in fact due to the small t_a/t_ν ratio: the particle is small and light enough to respond to the flow faster, accelerate, and prevent significant shear from growing on the particle surface in the first place. Therefore, viscosity-deficit in the s-fluid close to the interface under harmonic averaging does not affect the physics as significantly as the viscosity-surplus in the fluid phase under arithmetic averaging.

Viscous Dissipation in the Solid

Even if the wall response time is captured correctly, some energy is still lost to s-fluid shearing. Fortunately, this is limited in the first place by the fast particle response time t_a. Figure 8.8 shows the fraction of viscous dissipation in the CG-LBM domain that occurs in the s-fluid. After the diffusing momentum

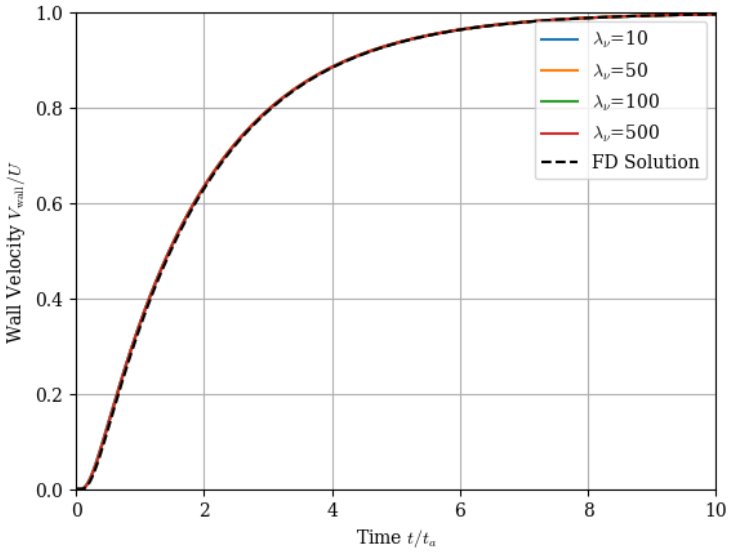

Figure 8.7: Solid Wall Velocity V_{wall} over Time for Different Viscosity Ratios λ_ν, with Harmonic Viscosity Averaging for CG-LBM. FD benchmark measured at the right-hand simulation boundary. LBM results measured at the phase-field boundary between fluid and s-fluid layers.

reaches the s-fluid, this fraction is essentially constant; less than a percent of all energy dissipated in the domain is dissipated in the s-fluid. This does not change the fact that the fluid shears continuously, and accumulated displacement on the surface of the s-fluid may be significant over time. Furthermore, as the s-fluid accelerates towards the left-side velocity U, shear rates drop throughout the domain, and the effective Reynolds number drops. This case and the measurement of velocity at the interface were therefore particular suited to be captured by an s-fluid.

8.2 Effects of the Recoloring Operator

In CG-LBM, immiscibility and phase-field interfaces are maintained by the recoloring operator (equation (6.15) for colorblind CG-LBM). Because the recoloring operator introduces an additional, purely numerical lengthscale $\delta \sim 1/\beta$ through the segregation parameter β, it can induce non-physical phenomena in the flow field through the diffuse interface.

8.2.1 Spurious Smearing

As mentioned in section 3.5.3, the recoloring operator implicitly solves an Allen-Cahn interface-tracking equation, which describes the time-evolution of the tracked phase-field [7]. When explicitly tracking the interface, an *interface mobility* parameter is tuned to control the movement of the phase-field interface. In CG-LBM, however, this parameter is not only hidden and implicitly defined, it is *not* free, and depends on the lattice speed-of-sound.[2] Analysis of the implied Allen-Cahn system shows that there is a mobility-dependent "artificial diffusion-like mechanism that attempts to achieve radial symmetry" and smears out sharp phase-field corners [7]. Therefore, through this *spurious smearing*, the recoloring operator itself can cause fluid motion, through effective forces which are entirely numerical and have no basis in hydrodynamic or capillary phenomena.[3]

[2] Alternative CG-LBM formulations can allow interface mobility tuning [6].

[3] For $N = 2$ fluids, such sharp corners are unlikely except perhaps at initialization. For $N > 2$, however, three-phase contact between fluids can occur. Fortunately, N-fluid CG-LBM is able to reproduce the sharp contact angles between the fluid phases, which depend on their respective surface tensions [3].

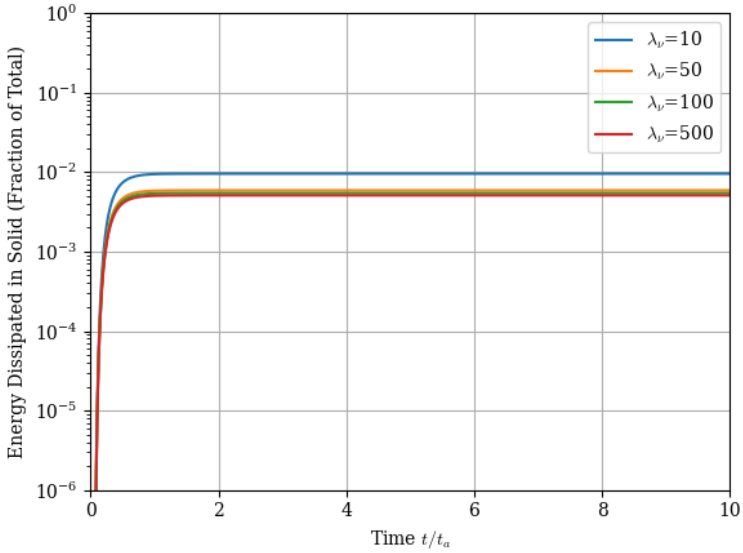

Figure 8.8: Fraction of Viscous Dissipation occurring in the S-fluid, of the total Viscous Dissipation in the domain. Accelerated Wall Case under harmonic viscosity averaging.

This effect is strictly limited to sharp features across phase-field interfaces maintained by the recoloring operator. Hence, in two-phase flow, while the contact line must necessarily intercept a solid wall at a sharp contact angle, the interface between individual fluids and the wall is not maintained by recoloring, and no spurious smearing occurs. The same is true for contact lines on any solid particle, which can be modelled without issues [4]. However, s-fluid particle surfaces, which are maintained by the recoloring operator, are now subject to such smearing effects. This limits admissible s-fluid particle geometries: in 2D, for instance, an angular feature will smear its sharp edges and approach a circular shape [7]. However, certain flow conditions may induce these sharp edges even for radially symmetrical s-fluid particles.

8.2.2 Catastrophic S-Fluid Particle Smearing

In this section, we discuss how spurious smearing can catastrophically deform s-fluid particles, even when they are radially symmetrical.

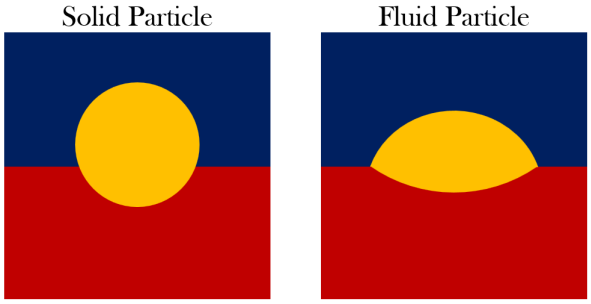

Figure 8.9: Particle at a Fluid-Fluid Interface. On the left, the steady-state solution for a solid particle, which migrates towards the fluid that preferentially wets in to minimize its interfacial surface energy. On the right, the steady state for a liquid droplet, which deforms into a lens, with interface curvatures reflecting surface tensions with either other fluid, and forms contact angles with the flat fluid-fluid interface as predicted by Young's law.

Figure 8.9 shows a good validation case for wettable particles. A solid particle located at a fluid-

fluid interface will experience capillary forces that push it towards the fluid that preferentially wets it. Mechanical equilibrium is reached when the particle migrates at a position predicted by the fluid-fluid surface tensions and both solid-fluid surface tensions [4, 8]. The case is also a good test for s-fluid particles. Since the latter are, in fact, fluids, the steady-state solution is that for fluids: a lensed particle which exhibits contact angles predicted by Young's law. A sufficiently viscous s-fluid particle, however, should converge to the solid's steady-state solution first, and experience limited deformation to the fluid steady-state over a limited span of time, which in our case should match that of ink-jetting phenomena after scaling.

This 2D case was initially selected to study s-fluid particles' ability to convert capillary forces into linear momentum. A circular s-fluid particle is initialized at the interface, with viscosity ratio $\lambda_\nu = 100$ between the s-fluid particle and the fluids. Surface tension between the fluids is obtained from an Ohnesorge number $\mathrm{Oh} = 0.5$ representative of ink-jet printing [5], and therefore correctly scaled to the viscosity inside the fluids; droplet radius is used as a characteristic length. Preferential wetting of the s-fluid particle is adjusted by setting different solid-fluid surface tensions, which are of the same order as the fluid-fluid surface tension to avoid high spurious velocities from perturbation. A capillary timescale t_{cap} can be computed for the particle as:

$$t_{\text{cap}} = \sqrt{\frac{\rho_S R^3}{\sigma}} \tag{8.5}$$

where ρ_S is the s-fluid density, R is its initialization radius, and σ is the surface tension between the ***fluids***.

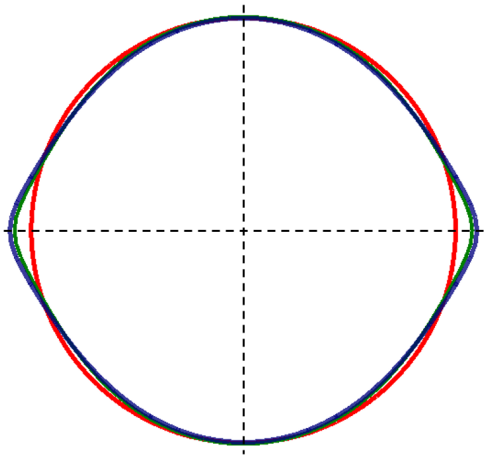

Figure 8.10: Catastrophic S-Fluid Particle Deformation. Each line represents the $\rho_S^{\tilde{N}} = 0.5$ s-fluid phase-field marking the particle. The horizontal dashed line represents the plane of the fluid-fluid interface where the particle rests. Vertical line marks an axis of symmetry for the initialized particle. Successive red-green-blue contours respectively correspond to $t = \{0, 0.1t_{\text{cap}}, 0.2t_{\text{cap}}\}$ where t_{cap} is a capillary timescale for the particle. The particle deforms symmetrically to the fluid-fluid interface, which is not consistent with either physical tendency towards the steady-state solutions for a solid or fluid particle. The deformation is in fact due to spurious smearing.

Figure 8.10 shows three phase-field contours marking the boundaries of an s-fluid particle in such a simulation. Surface tension parameters are such that the steady-state solution should lead the particle to migrate upwards above the fluid-fluid interface, the plane of which is denoted by the horizontal dashed line. The fluid steady-state solution should lead to droplet to bulge into the fluid on the top, with which it has a lower surface tension. However, after little time (on the scale of capillary behavior on the particle), the particle displays a quasi-symmetrical deformation which stretches it tangentially along the fluid-fluid interface. This deformation is not consistent with a tendency:

- towards the solid steady-state solution, which leads to forces ***normal*** to the fluid-fluid interface pushing the particle upwards;

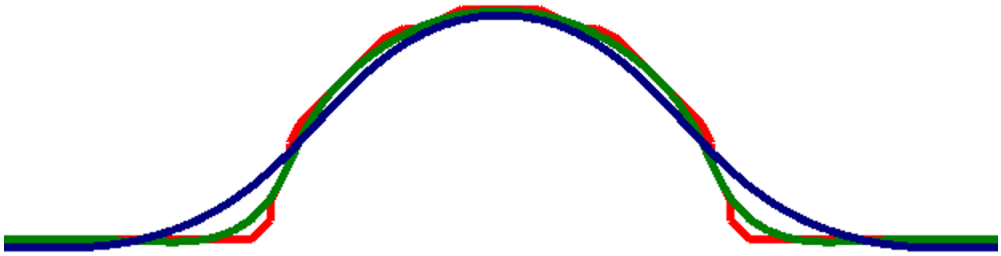

Figure 8.11: Spurious Smearing for $N = 2$ case. Each line represents the interface between the two phases. Successive red-green-blue lines correspond to increasing timesteps. Simulation contains no physical mechanism to cause fluid flow, and yet the interface deforms under the effect of phase-field mobility. The contact of the hemispherical feature with the otherwise flat interface is in fact a sharp edge which the recoloring operator will smear.

- towards the liquid steady-state solution, which is not symmetrical and also leads to a net movement of fluid towards the upper fluid.

This deformation is catastrophic, because the particle is no longer spherical, and has apparently deformed due to a non-physical phenomena. The same behavior is observed even in the absence of surface tension, and is due to the recoloring perturbation.

Figure 8.11 shows a similar $N = 2$ case, obtained with Flow Matter's original code, before the implementation of N-fluid CG-LBM. Two fluids with equal density, viscosity, and no surface tension between them are initialized across a flat interface. The fluid at the bottom is also initialized with a hemispherical sector jutting into the fluid at the top. There are no physical parameters that could induce flow in this simulation. However, the intersection of the hemispherical profile, orthogonal to the flat interface, is a sharp edge, and tends to be smoothed by the perturbation operator. The segregation lengthscale $\delta \sim 1/\beta$ and the implicit interface mobility are the only possible cause for the resulting flow.

Therefore, even if the particle in figure 8.10 was initially radially symmetrical, its presence at the interface caused a sharp edge in the phase-fields of either fluid. The resulting smearing of the fluid phase-fields must also be accompanied by a smearing of the particle.

8.3 Conclusions

The use of s-fluids in inkjet printing simulations was initially considered as a means to use CG-LBM perturbation to mediate wetting on particles entrained in jets. Therefore, s-fluid particles would necessarily be used in the presence of at least two other actual fluids. The recoloring-induced spurious smearing of s-fluid particles is sufficient cause to not recommend their use in such simulations, since even radially symmetrical particles can apparently cause unphysical flows when located at an interface. It is not clear whether setting arbitrarily large surface tensions between the fluids and the solid could have maintained the s-fluid particle interface. Doing so, however, would induce larger spurious velocities in the actual fluids. It is also possible that s-fluid particles are less susceptible to these smearing effects if initialized away from a fluid-fluid interface, and allowed to evolve towards them through actual flow.

The second research question on superviscous fluids in section 5.1.2 can be answered, and a first recommendation on the third research question given:

Research Questions: Superviscous Particles

- What are the phase-fields for N-fluid CG?

  See section 6.3.

- What is the effect of diffuse CG-LBM interfaces on momentum-transfer to s-fluids?

  Diffuse CG-LBM interfaces lead to continuous transitions in viscosity between fluid and artifically superviscous s-fluids. Viscosity averaging at the interface determines how this affects the flow field. When *arithmetic viscosity averaging* is used, high s-fluid viscosity bleeds into the fluid. Effective s-fluid particle surfaces appear to penetrate deeper and deeper into the fluid. *Harmonic viscosity averaging* limits viscosity discrepancies to the s-fluid-side of the interface, and allows s-fluid particle response to flow to approach that of an actual solid particle. Diffuse CG-LBM interfaces also mean that s-fluid surfaces are maintained by the recoloring operator. The latter tends to smoothen sharp corners formed by phase-fields, which leads to *catastrophic spurious smearing* of even radially symmetrical s-fluid particles, when located at fluid-fluid interfaces.

- Could superviscous particles be used in the ink-jet printing regime?

  Spurious smearing is sufficient cause to not recommend s-fluid particles for use in the inkjet printing regime. However, s-fluid particles were shown to be able to respond well to single-phase flows, and the case revealing the issue of spurious smearing may be avoided by other initializations.

Chapter 8 References

[1] Karun Pravin Nirod Datadien. "Directional instabilities in microdroplet jetting: a numerical approach". PhD thesis. Applied Physics and Science Education, Jan. 31, 2024.

[2] Alessandro De Rosis, Rongzong Huang, and Christophe Coreixas. "Universal formulation of central-moments-based lattice Boltzmann method with external forcing for the simulation of multiphysics phenomena". In: *Physics of Fluids* 31.11 (Nov. 2019). doi: 10.1063/1.5124719.

[3] Sébastien Leclaire, Marcelo Reggio, and Jean-Yves Trépanier. "Progress and investigation on lattice Boltzmann modeling of multiple immiscible fluids or components with variable density and viscosity ratios". In: *Journal of Computational Physics* 246 (2013). doi: https://doi.org/10.1016/j.jcp.2013.03.039.

[4] Y.K. Lee and K.H. Ahn. "Particle dynamics at fluid interfaces studied by the color gradient lattice Boltzmann method coupled with the smoothed profile method". In: *Physical Review E* 101.5 (2020). doi: 10.1103/PhysRevE.101.053302.

[5] D. Lohse. "Fundamental Fluid Dynamics Challenges in Inkjet Printing". In: *Annual Review of Fluid Mechanics* 54 (2021). doi: 10.1146/annurev-fluid-022321-114001.

[6] A. Subhedar. "Color-gradient lattice Boltzmann model for immiscible fluids with density contrast". In: *Phys. Rev. E* 106.4 (Oct. 2022). doi: 10.1103/PhysRevE.106.045308.

[7] A. Subhedar et al. "Interface tracking characteristics of color-gradient lattice Boltzmann model for immiscible fluids". In: *Phys. Rev. E* 101.1 (Jan. 2020). doi: 10.1103/PhysRevE.101.013313.

[8] Lin Zheng, Song Zheng, and Qinglan Zhai. "Phase-field lattice Boltzmann equation for wettable particle fluid dynamics". In: *Phys. Rev. E* 108.2 (Aug. 2023). doi: 10.1103/PhysRevE.108.025304.

Chapter 9 | Solid-Phase Perturbation

Key Points

- Solid-Phase Perturbation (SPP) can be adapted to modern CG-LBM.
- SPP is very sensitive to phase-field boundary treatment near walls.
- SPP reproduces physical wetting/dewetting phenomena when a solid phase-field is defined.
- The novel colorblind CG-LBM color-gradient formulation from chapter 6 can be used to directly recover a consistent SPP operator.
- Single-Node SPP is not appropriate in the ink-jet printing regime due to inaccuracies resulting from sharp phase-field gradients near walls.

In this chapter, SPP ideas from [2] and [4] are adapted to modern CG-LBM. In section 9.1, SPP is developed by injecting information about wall-normal vectors into the perturbation operator. Among other problems, this gives no information on how to treat phase-fields near the wall, and leads to competing enforcement of different contact angles. In section 9.2, a different approach considering a solid phase-field directly produces a consistent SPP operator, and physically consistent contact angles. Previously unresolved inaccuracies also arising in [4] are explained.

Following other energy-based wetting implementations [2, 4, 5], we define a wetting parameter χ_{lm} for a fluid-pair lm using Young's law in equation (2.11) and a desired contact angle $\theta_{lm,\text{in}}$ for the fluid pair and the solid surface:

$$\chi_{lm} = \cos\theta_{lm,\text{in}} = \frac{\sigma_{Sm} - \sigma_{Sl}}{\sigma_{lm}} \tag{9.1}$$

where σ_{Sl} is the surface tension between the solid and fluid l, and likewise with σ_{Sm} and fluid m. For $N = 2$, we denote χ the single wetting parameter. Flat walls coinciding with domain boundaries are considered.

9.1 Single-Node SPP with Wall-Normal Vectors

CG-LBM perturbation generates the interfacial force at the interface, in a direction normal to it. Since the interface is diffuse, it is localized by proxy with the color-gradient $\boldsymbol{F}_{lm}$. For a known wall position captured with the bounce-back boundary condition from section 3.3.3, the interface location is known exactly, and we replace, in the perturbation operator in equation (6.16):

$$\boldsymbol{F}_{lm} \to \boldsymbol{n}$$

where $\boldsymbol{n}$ is the wall-normal vector located at the first node off the wall. We set $\boldsymbol{n} = \boldsymbol{0}$ in the bulk away from these nodes. Recall that since no-slip is enforced at the wall, no recoloring needs to occur between the fluid and the wall.

9.1.1 SPP Operator

Since pair-wise perturbation for colorblind CG-LBM from equation 6.16 is used, we recover the corresponding single-node SPP operator $\Omega_i^{(2S)}$ acting on the post-(fluid-fluid)-perturbation populations $f_i^{\star\star}$ to yield to post solid-fluid-perturbation populations $f_i^{S\star\star}$:

$$f_i^{S\star\star} = \Omega_i^{(2S)}(f_i^{\star\star}) = f_i^{\star\star} + \sum_l \sum_{m>l} A_{lm}^S C_{lm} |\boldsymbol{n}| \left[w_i \frac{(\boldsymbol{c}_i \cdot \boldsymbol{n})^2}{|\boldsymbol{n}|^2} - B_i \right] \tag{9.2}$$

where A_{lm}^S contains information about fluid-solid surface tensions. The combination of the concentration factor C_{lm} and our definition of $\boldsymbol{n}$ mean that SPP is only active for sufficient concentrations of both fluids l and m near the wall marked by $\boldsymbol{n} \neq \boldsymbol{0}$. From equation (6.12), while local relaxation rate ω_{eff} is defined, SPP surface tension is not. Since surface tension σ_{Sl} between the wall and a fluid l is a property defined at the ***interface*** between the wall and the fluid, we weight the surface tension from each fluid by its ***phase-field*** $\rho_l^{\bar{N}(n)}$, leading to:[1]

$$A_{lm}^S = \frac{9}{2} \left(\rho_l^{\bar{N}(n)} \sigma_{Sl} + \rho_m^{\bar{N}(n)} \sigma_{Sm} \right) \omega_{\text{eff}} \tag{9.3}$$

We can identify several issues with this line of thinking, and the SPP operator defined by equations (9.2) and (9.3):

- we have no information about how to normalize the wall-normal vector $\boldsymbol{n}$, and its magnitude is free;
- the phase-field averaging in (9.3) is a guess, and is not constrained by this "derivation";
- since the weighting of surface tensions or wall-normal vectors is not constrained, the $9/2$ scalar factor in (9.3) is entirely unclear;
- *no information is given as to the treatment of phase-fields near walls.*

9.1.2 Competition with Boundary Conditions

In the code, the physical domain is enclosed by ghost nodes where information is included to enable information to stream in or out of domain boundaries, and evaluate gradients there. When SPP in (9.2) is used, fluid phase-field gradients near the wall still need to be closed by assigning phase-field values to the ghost-nodes. A natural choice is set ghost node phase-field values as the average computed from neighboring fluid nodes.[2] However, note that this necessarily suppresses phase-field gradients at the wall: if an interface meets the wall with no gradients, it is orthogonal to it, and a ***neutral*** $90°$ ***contact-angle is enforced*** by means of a geometry-based wetting boundary condition. This effective boundary condition will in fact compete with the SPP operator in equation 9.2.

Figure 9.1 shows the time-evolution towards steady state of the phase-field contour for a droplet on a solid surface, using SPP from equation (9.2) and the phase-field average treatment described above. SPP is able to induce dewetting (left) and wetting (right) phenomena.[3] However, it competes with the geometry-based boundary condition.

Figure 9.2 shows how in a simulation ***with no surface tension***, neither between the fluids or with the solids through SPP, the contact line moves to form a neutral contact angle. Without fluid-fluid surface tension, the rest of the droplet's shape mostly does not adjust to reflect this. The fact that a contact angle is enforced despite the absence of surface tension also underlines the complete disconnect between fluid-fluid perturbation and geometry-based boundary conditions.

[1] The SPP operator (5.3) from [2] suggests that surface tensions be ***density***-weighted. However, in equation (6.16), concentration factor aside, it is the magnitude of the color-gradient $\boldsymbol{F}_{lm}$ which determines the magnitude of the perturbation. For a variation in color-gradient of order 1 (from a pure phase to the absence thereof) across an interface width $\delta \sim 1/\beta = \mathcal{O}(1)$, we find $|\boldsymbol{F}_{lm}| = \mathcal{O}(1)$, with no density-weighting. This supports the idea of phase-field-weighting used here.

[2] This is similar to the treatment of fluid density at the wall used in the bounce-back boundary condition with moving walls of equation 3.32.

[3] The dewetting on the left of figure 9.1 could also be attributed in part to the phase-field boundary condition.

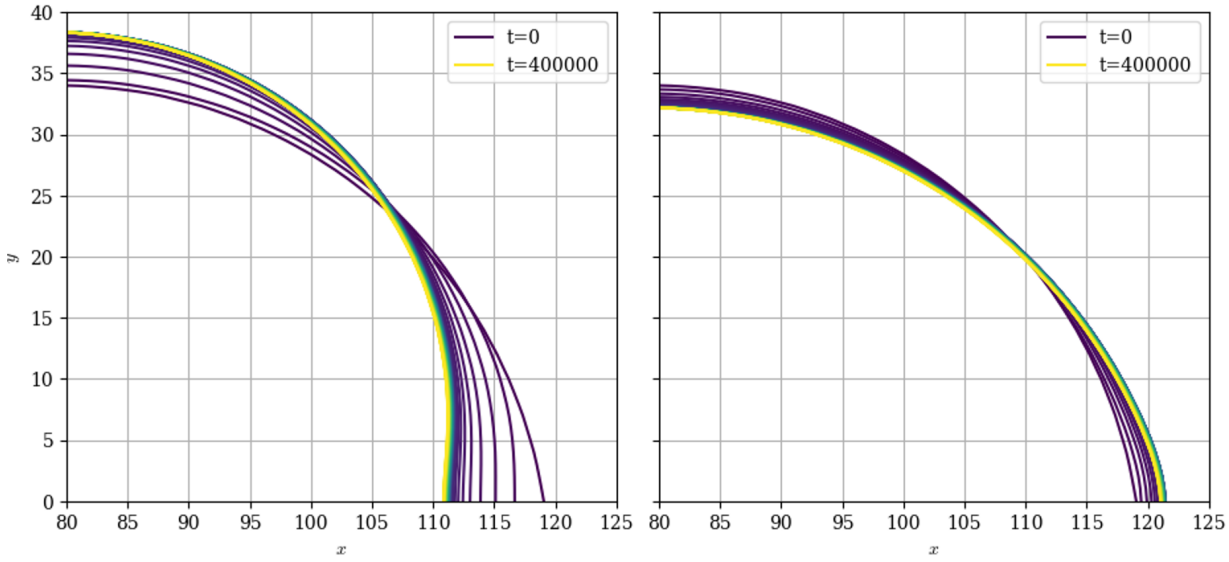

Figure 9.1: Time-Evolution of Droplet Contours using SPP with Wall-Normal Vectors. On the left, a value of χ implying dewetting is used; on the right, a value implying wetting. This SPP competes with an implied geometry-based boundary conditions which tends to impose a neutral contact angle.

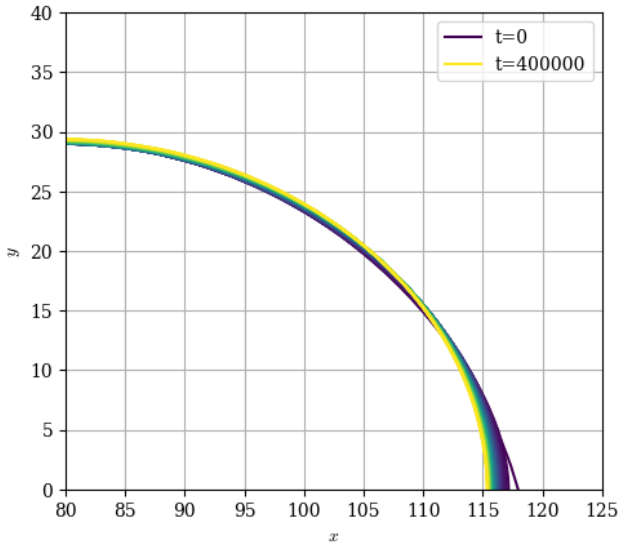

Figure 9.2: Time-Evolution of Droplet Contours with no Surface Tension or SPP. The phase-field boundary treatment implies a neutral contact angle, towards which the contact line evolves.

In simulations, it was noted that regardless of input χ, if the droplet was initialized with a neutral contact angle, SPP was not able to move the contact line at all. The problematic effects of the phase-field boundary treatment also appeared to depend on the required path towards the desired contact angle. Therefore, we conclude that SPP should not be formulated only using wall-normal vectors, due to undefined boundary treatment and competing wetting enforcement.

9.2 SPP with Solid phase-field

In reference [4], fluids interact with the wall by treating it as a "stationary fluid" with "constant mass density at the boundary nodes". This information affects the color-gradient at the boundary nodes. The authors of the publication achieve controllable wetting behavior after generating a calibration curve. Especially since constant density and viscosity ratios are considered, this constant "solid" density implies a constant *solid phase-field.*

Following a similar approach, this section defines a consistent SPP operator through the definition of a solid phase-field. Physical wetting behavior is achieved, and unresolved inaccuracies in [4] are addressed.

9.2.1 SPP Operator

The wall is ***not*** treated as a stationary fluid, has no corresponding density, and is directly defined through a phase-field $\rho_S^{\bar{N}}$, with $\rho_S^{\bar{N}} = 1$ defining pure solid. The sum of local phase-fields now includes $\rho_S^{\bar{N}}$, which therefore defines the fluid-solid interfaces for CG-LBM. The solid phase-field is constant, and is not recolored: it is not a fluid's phase-field.

The resulting SPP operator can be written with no assumptions. Thanks to the new relationship found between the fluid phase-fields $\rho_k^{\bar{N}(n)}$ and the color-gradient $\boldsymbol{F}_{lm}$ in equation (6.30), the color-gradient $\boldsymbol{F}_{lS}$ between a fluid l and the solid is:

$$\boldsymbol{F}_{lS} = \rho_S^{\bar{N}} \nabla \rho_l^{\bar{N}(n)} - \rho_l^{\bar{N}(n)} \nabla \rho_S^{\bar{N}} \tag{9.4}$$

And so, merely applying the perturbation operator from equation (6.11) between all fluid k's phase-fields and the solid S's phase-field:

$$\boxed{f_i^{S\star\star} = \Omega_i^{(2)}(f_i^\star) = f_i^\star + \sum_k \frac{1}{2} A_{kS} |\boldsymbol{F}_{kS}| \left[w_i \frac{(\boldsymbol{c}_i \cdot \boldsymbol{F}_{kS})^2}{|\boldsymbol{F}_{kS}|^2} - B_i \right]} \tag{9.5}$$

where the concentration factor has been removed for conciseness, noting the return of the $1/2$ factor since there is no solid population to perturb, and:

$$A_{kS} = \frac{9}{2} \sigma_{Sk} \omega_{\text{eff}} \tag{9.6}$$

where σ_{Sk} is the surface tension between the solid S and the fluid k.

9.2.2 Single-Node SPP with $\rho_S^{\bar{N}}$

Recall that we are attempting ***single-node*** SPP only, where SPP is limited to the first node off the wall. For single-node SPP, no diffuse solid phase-field is defined, and we ***treat the ghost nodes as physical solid nodes.*** There, inside the solid walls, we set $\rho_S^{\bar{N}} = 1$ and fluid phase-fields $\sum_k \rho_k^{\bar{N}(n)} = 0$, whereas $\rho_S^{\bar{N}} = 0$ and $\sum_k \rho_k^{\bar{N}(n)} = 1$ in the fluid nodes. In this way, SPP only occurs in the first fluid node off the wall, where the phase-field gradient $\nabla \rho_l^{\bar{N}(n)}$ for fluid l is affected by the (physical) ghost node values, and where $\rho_S^{\bar{N}} = 0$. There, equation (9.4) yields for single-node SPP:

$$\boldsymbol{F}_{lS} = -\rho_l^{\bar{N}(n)} \nabla \rho_S^{\bar{N}} \tag{9.7}$$

and in turn, noting $|\boldsymbol{F}_{lS}| = \rho_l^{\bar{N}(n)} |\nabla \rho_S^{\bar{N}}|$, equation (9.5) can be rewritten:

$$
\begin{aligned}
f_i^{S\star\star} = \Omega_i^{(2)}(f_i^{\star\star}) &= f_i^{\star\star} + \sum_k \frac{1}{2} A_{kS} \rho_l^{\bar{N}(n)} |\nabla \rho_S^{\bar{N}}| \left[w_i \left(\frac{-\rho_l^{\bar{N}(n)}}{\rho_l^{\bar{N}(n)}} \right)^2 \frac{(\boldsymbol{c}_i \cdot \nabla \rho_S^{\bar{N}})^2}{|\nabla \rho_S^{\bar{N}}|^2} - B_i \right] \\
&= f_i^{\star\star} + \sum_k \frac{1}{2} A_{kS} \rho_l^{\bar{N}(n)} |\nabla \rho_S^{\bar{N}}| \left[w_i \frac{(\boldsymbol{c}_i \cdot \nabla \rho_S^{\bar{N}})^2}{|\nabla \rho_S^{\bar{N}}|^2} - B_i \right] \\
f_i^{S\star\star} &= f_i^{\star\star} + \frac{1}{2}\frac{9}{2} \left(\sum_k \rho_k^{\bar{N}(n)} \sigma_{Sk} \right) \left[w_i \frac{(\boldsymbol{c}_i \cdot \nabla \rho_S^{\bar{N}})^2}{|\nabla \rho_S^{\bar{N}}|^2} - B_i \right]
\end{aligned}
\tag{9.8}
$$

Equation (9.8) shows that, following a phase-field-weighted arithmetic average of fluid-solid surface tensions, single-node SPP can be simplified to a single operation, down from N operations (one for each fluid). For $N = 2$ fluids l and m, we write:

$$
f_i^{S\star\star} = f_i^{\star\star} + \frac{1}{2}\frac{9}{2} \left(\rho_l^{\bar{N}(n)} \sigma_{Sl} + \rho_m^{\bar{N}(n)} \sigma_{Sm} \right) \left[w_i \frac{(\boldsymbol{c}_i \cdot \nabla \rho_S^{\bar{N}})^2}{|\nabla \rho_S^{\bar{N}}|^2} - B_i \right] \tag{9.9}
$$

Considering the local gradients are computed using immediate neighbors only [1, 6], we have $\nabla \rho_S^{\bar{N}} = 0$ at all points not in immediate contact with solid nodes. Therefore, if $N = 2$, the SPP operator can reintegrate the C_{lm} concentration factor, and SPP only occurs for sufficient concentrations of two different fluids near a solid wall. From equation (9.9), we therefore use for ***single-node SPP with*** $N = 2$:

$$
\boxed{f_i^{S\star\star} = f_i^{\star} + \frac{1}{2}\frac{9}{2} C_{lm} \left(\rho_l^{\bar{N}(n)} \sigma_{Sl} + \rho_m^{\bar{N}(n)} \sigma_{Sm} \right) \left[w_i \frac{(\boldsymbol{c}_i \cdot \nabla \rho_S^{\bar{N}})^2}{|\nabla \rho_S^{\bar{N}}|^2} - B_i \right]} \tag{9.10}
$$

Note that following the definition of a solid phase-field, no assumptions were made to obtain equation (9.5) (or (9.8) for single-node SPP, or (9.10) for $N = 2$), the form of which is fully constrained by the original perturbation operator in equation (6.11) and the relationship between phase-fields and color-gradients in equation (6.30). No solid density or viscosity was defined either.

Initially, the wall-normal vector $\boldsymbol{n}$ used in section 9.1 was used in equation (9.10) in place of $\nabla \rho_S^{\bar{N}}$. However, it is more consistent to use the isotropic gradient operator from equation (3.55) (the same used to compute other phase-field gradients), which for our flat walls, is nonzero for the first fluid nodes off the wall, with:

$$
|\nabla \rho_S^{\bar{N}}| = 0.5
$$

Figure 9.3 shows a red droplet in a blue medium for different contact angles, for different values of the wetting parameter χ from equation 9.1. From a neutral initialization ($\theta = 90°$), both wetting (top) and dewetting (bottom) behavior is qualitatively captured.

9.2.3 Assessing the Method

To understand what this SPP is capturing, a series of $N = 2$ droplet simulations with different wetting parameters χ was run. In a 120×80 domain, common parameters are, in lattice units:

- hemispherical droplet initialization radius $R_0 = 40$ (initialized with a neutral contact angle with the bottom wall);
- fluid density $\rho = 1$ with unity density ratio $\lambda_\rho = 1$ across fluids;
- fluid viscosity $\nu = 1/6$ with unity viscosity ratio $\lambda_\nu = 1$ across fluids;
- segregation parameter $\beta = 0.7$;
- surface tension between fluids $\sigma_{rb} = 0.01$.

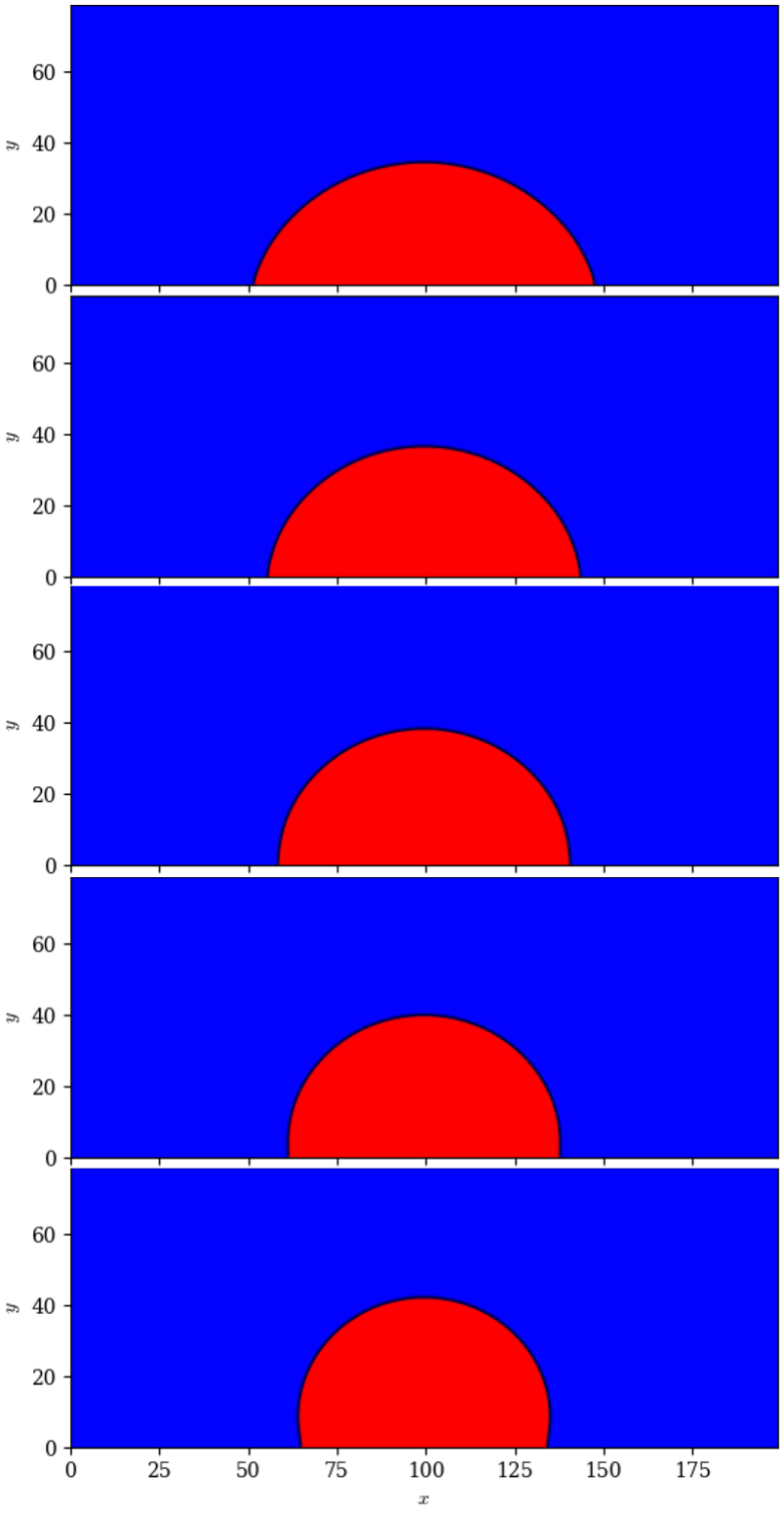

Figure 9.3: Red Drops in Blue Fluid with Different Contact Angles, as recovered by SPP in equation (9.10), identified by respective phase-fields above 0.5. Steady state results for different values of the wetting parameter χ.

σ_{Sb}	σ_{Sr}	$\chi_{\mathbf{in}}$	$\theta_{\mathbf{in}}$
0.02	0.02	0	90°
0.02	0.019	0.1	84.26°
0.02	0.018	0.2	78.46°
0.02	0.017	0.3	72.54°
0.02	0.016	0.4	66.42°
0.02	0.015	0.5	60°
0.02	0.014	0.6	50.13°
0.02	0.013	0.7	45.57°

Table 9.1: Input Wetting Parameters for the Simulation, with expected equilibrium contact angle θ_{in}.

At unity density ratio, non-normalized and normalized phase-fields are equivalent. Viscosity interpolation is irrelevant for unity viscosity ratio. Table 9.1 shows the range of tested parameters, with different combinations of σ_{Sb} and σ_{Sr} leading to different wetting parameters χ_{in} *in*put into the simulation. After 200 000 timesteps, the contact angle is measured by measuring the base c and height h of an assumed spherical cap droplet of radius R, and computing the contact angle θ_{out} from trigonometry:

$$\begin{aligned} R &= \frac{h}{2} + \frac{c^2}{8h} \\ \theta &= \arctan\left(\frac{c/2}{R-h}\right) \end{aligned} \tag{9.11}$$

Equation (9.11) yields a contact angle that describes the droplet as a whole.[4] These *out*put contact angles θ_{out} are used to compute apparent in-simulation output wetting parameters χ_{out}, and to plot an input-output curve.

Different simulation outcomes can be identified. If the input-output χ curve is:

1. completely nonlinear, the SPP method has failed, as there is no consistent and predictable effect of wetting parameter χ;
2. linear, but does not pass through the origin, regardless of its slope, the SPP method is physically inaccurate, but can be calibrated for practical use;
3. linear, passes through the origin, but with a non-unity slope, the SPP method is correctly formulated, but the perturbation operator is incorrectly scaled;
4. $\chi_{\text{out}} = \chi_{\text{in}}$, then the SPP method is entirely successful, and strict equivalence between physical and simulation surface tensions/energies for all fluid-fluid and fluid-solid interfaces is maintained.

Figure 9.4 shows SPP simulation results consistent with predicted outcome 2. A linear fit closely follows results. The linear fit with the circular cap assumption also confirms by proxy that surface tension maintains a circular cap.[5] The recovery of a linear profile clearly indicates that ***the boundary treatment with physical solid phase-fields is conceptually correct***, and produces controllable and consistent contact angles. Something at the boundary is adversely affecting the relationship between physical and simulation

[4] At least, if the droplet is in fact a spherical cap.

[5] The contact angle was also measured by fitting a polynomial function g to the last 2 points (nearest to the wall) of the $\rho_r^{\tilde{N}} = 0.5$ contour marking the fluid-fluid interface on the solid wall, and computing the contact angle from the gradient thereof:

$$\theta = \arctan\left(\nabla g\right) \tag{9.12}$$

Including the last 2 points nearest to the wall reveals that contact angle directly off the wall is not the same as the contact angle that describes the overall droplet shape. Including the last 2 points after that first point off the wall yielded contact angles that were practically equal to those computed with the spherical cap assumption, confirming the droplets have a spherical shape. Not including that first point is common for energy-based wetting [7], and merely isolates out near-boundary effects which do not reflect actual droplet shape. This data is not shown here, because the interpolation script is unreliable at time of writing, and requires some manual oversight for which time ran out.

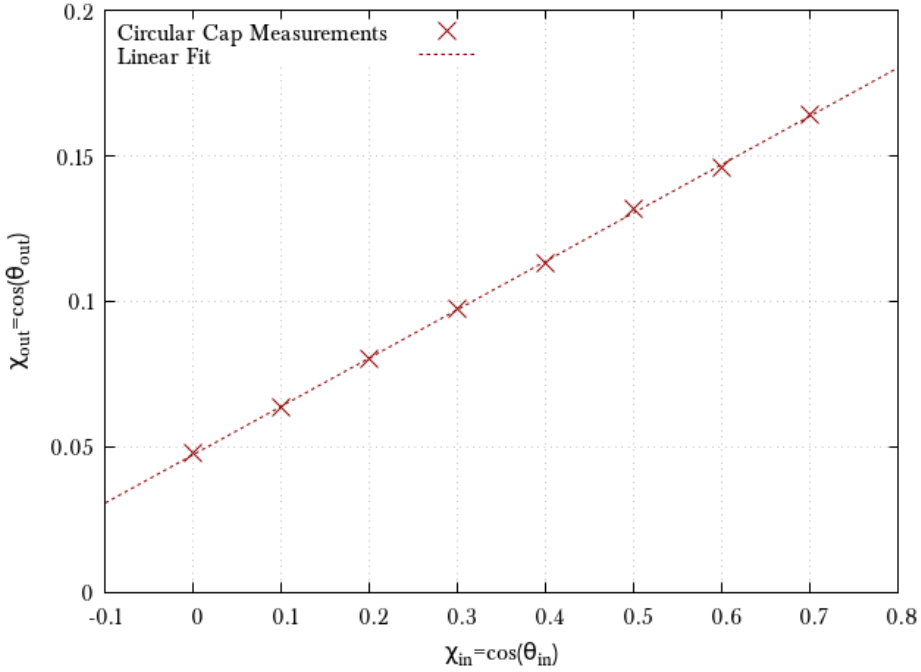

Figure 9.4: Input-Output Curve for single-node SPP with $\rho_S^{\bar{N}}$.

parameters, but the linear profile indicates no irresolvable bias towards a different contact angle, as was the case in section 9.1.

While the response could be calibrated, it depends on many parameters, and doing so would mean to abandon attempting to recover a fully physically consistent SPP with strict equivalence of physical and simulation parameters. The slope of the calibration curve appeared to depend on viscosity ratio.[6] This marks *single-node* SPP as inappropriate in the ink-jet printing regime, due to necessary viscosity and density ratios: attempting to tune the calibration curve only furthers the disconnection from physical parameters, with unpredictable effects on dynamic response, for instance.

9.2.4 Explaining Inaccuracies

In figure 9.4, we note that for $\chi_{\text{in}} = 0$, where there should be no mechanism for either fluid to preferentially wet the solid, a non-neutral contact angle is recovered. Since a linear relationship is still obtained, this does not point to a competing contact angle enforcement, but specifically to a source of inaccuracies. This result is similar to that from [4]. The latter reference, however, does not comment on this, and uses SPP after obtaining the calibration curve.

Since we have defined a solid phase-field $\rho_S^{\bar{N}}$, we have also implicitly implied a macroscopic interface between fluid and solid regions. As shown in figure 9.5 the single-node treatment means that fluid phase-fields must transition to 0 across a single node, and vice versa for the solid phase-field. Even though we know where the wall is located, the phase-field transition is so abrupt that it could occur anywhere across the lattice link to the ghost (wall) node: gradient $\rho_l^{\bar{N}(n)}$ and $\rho_S^{\bar{N}}$ evaluations, respectively for fluid l and the solid, will be inaccurate. The position of the solid-fluid interface marker $\rho_S^{\bar{N}} = 0.5$ is sub-grid and badly resolved. Consistently with the fact that the fluid-solid interface is essentially defined like a fluid-fluid interface, this mirrors a feature of CG-LBM interfaces in general. Fluid-fluid interfaces are maintained by the perturbation operator over a thickness $\delta \sim 1/\beta$. Smaller values of β extend the thickness of interfaces, meaning phase-field transitions are spread over a larger number of nodes: gradients are better resolved

[6] In one simulation, a neutral $\chi_{\text{in}} = 0$ with viscosity ratio $\lambda_\nu = 10^3$ setting caused an extremely violent dewetting event which caused the droplet to fly off the solid wall.

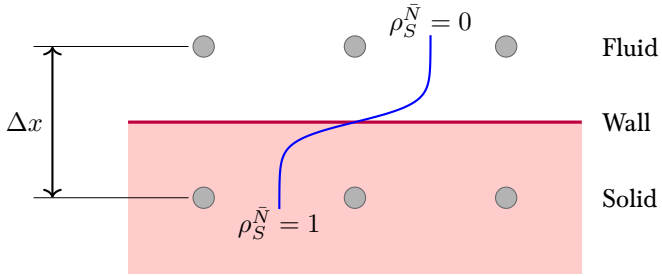

Figure 9.5: Schematic Solid Phase-Field Transition for Single-Node SPP. LBM nodes are represented by the gray circles. A possible solid phase-field transition with a $\tanh$ profile is qualitatively shown: the phase transition is too abrupt and entirely sub-grid, and gradient evaluations for both the fluid and solid phase fields will be inaccurate near the wall.

and measured more accurately. Instead, single-node SPP leads to fluid-solid interfaces where $\beta > 1$ or $\beta \to \infty$, in the limit of a very sharp interface. This leads to poor phase-field gradient accuracy near solid walls, and a skewed input/output relationship for χ. In addition, the large resultant color-gradients are associated with larger spurious velocities from perturbation operations [6].[7]

Note that despite the implied $\beta > 1$ parameter for the solid-fluid interfaces, no instabilities are observed as would be for fluid-fluid interfaces [3]. This is because segregation between the fluid and solid phases is effectively maintained by the bounce-back boundary condition, rather than by the segregation operator, which indeed requires $0 < \beta < 1$ in general and $\beta < 0.7$ for more consistent stability.

9.3 Conclusions

A solid phase-field $\rho_S^{\bar{N}}$ can be directly integrated in the new formulation of N-fluid color-gradients in equation (6.30) to yield a model-consistent SPP operator with no additional assumptions. The single-node application of this SPP, which only defines non-zero solid phase fields at a single node, is able to capture wetting/dewetting behavior as in [4]. The method is ***inaccurate*** but ***precise***, yielding a linear and calibratable relationship between fluid-solid surface-tensions and apparent contact angles. These inaccuracies can be explained by the effective sharpness of solid-fluid phase-field interfaces in CG-LBM.

The first two research questions from section 5.2.2 have been answered. Sufficient insights have been obtained to give a first recommendation for SPP applicability to inkjet printing:

[7] These large spurious velocities, when large viscosity ratios were attempted, were observed to cause significant spurious flow (including vortex formation and detachment) in the less-viscous phase.

Research Questions: Solid-Phase Perturbation

- Can SPP be adapted to modern CG-LBM to induce wetting/dewetting behavior?

  SPP can be adapted to N-fluid CG-LBM by defining a solid phase-field $\rho_S^{\bar{N}}$ which is directly injected in the new color-gradient formulation in equation (6.30) to yield a fluid-l-solid color-gradient:

  $$\boldsymbol{F}_{lS} = \rho_S^{\bar{N}} \nabla \rho_l^{\bar{N}(n)} - \rho_l^{\bar{N}(n)} \nabla \rho_S^{\bar{N}}$$

  which can be used in regular inter-phase perturbation.

- Can SPP be restricted to a single node off solid boundaries?

  Single-node SPP leads to precise but inaccurate contact-angle enforcement. Inaccuracies arise because fluid-solid transitions are too abrupt, and CG-LBM requires diffuse interfaces to accurately compute phase-field gradients. Input-parameter response can be calibrated.

- Could SPP be used in the ink-jet printing regime?

  Only single-node SPP could be attempted in this report, a technique which is not suited for larger density or viscosity ratios, which affect the calibration of input-parameter response. However, the inaccuracies of single-node SPP could be resolved by using a diffuse solid phase-field.

Chapter 9 References

[1] Karun Pravin Nirod Datadien. "Directional instabilities in microdroplet jetting: a numerical approach". PhD thesis. Applied Physics and Science Education, Jan. 31, 2024.

[2] M.M. Dupin, I. Halliday, and C.M. Care. "Multi-component lattice Boltzmann equation for mesoscale blood flow". In: *Journal of Physics A: Mathematical and General* 36.31 (2003). doi: 10.1088/0305-4470/36/31/313.

[3] I. Halliday, A. P. Hollis, and C. M. Care. "Lattice Boltzmann algorithm for continuum multicomponent flow". In: *Phys. Rev. E* 76.2 (Aug. 2007). doi: 10.1103/PhysRevE.76.026708.

[4] A. Kawasaki et al. "A lattice Boltzmann model for contact-line motions". In: *Computers and Mathematics with Applications* 55.7 (2008). doi: 10.1016/j.camwa.2007.08.026.

[5] Y.K. Lee and K.H. Ahn. "Particle dynamics at fluid interfaces studied by the color gradient lattice Boltzmann method coupled with the smoothed profile method". In: *Physical Review E* 101.5 (2020). doi: 10.1103/PhysRevE.101.053302.

[6] Haihu Liu, Albert J. Valocchi, and Qinjun Kang. "Three-dimensional lattice Boltzmann model for immiscible two-phase flow simulations". In: *Phys. Rev. E* 85.4 (Apr. 2012). doi: 10.1103/PhysRevE.85.046309.

[7] Sebastian Schmieschek and Jens Harting. "Contact Angle Determination in Multicomponent Lattice Boltzmann Simulations". In: *Communications in Computational Physics* 9.5 (2011). doi: 10.4208/cicp.201009.271010s.

Chapter 10 | Recommendations

Key Points

- The connection between N-fluid phase-field and color-gradient could be used to significantly reduce the number of recoloring operations.
- Superviscous fluids should be tested in single-phase hydrodynamic flows.
- Superviscous fluid susceptibility to spurious smearing should be investigated further, especially with more "permissive" initialization.
- The connection between N-fluid phase-field and color-gradient could also be used to improve the CG-SPM approach in [4] and extend its applicability to non-unity density and viscosity ratios.
- Solid-Phase Perturbation with Solid Phase-Fields should be attempted with *diffuse* solid phase-fields.

In this final chapter, we discuss recommendations based on the conclusions of chapters 6, 8, and 9.

10.1 Reducing Recoloring Operations

In chapter 6, a new link between phase-fields $\rho_l^{\bar{N}(n)}$ and N-fluid color-gradient $\boldsymbol{F}_{lm}$ was found in equation (6.30):

$$\boldsymbol{F}_{lm} = \rho_m^{\bar{N}} \nabla \rho_l^{\bar{N}} - \rho_l^{\bar{N}} \nabla \rho_m^{\bar{N}}$$

Consider that CG-LBM recoloring is a ***numerical*** operation that artificially keeps phases separate [5], even in the absence of surface tension. Recoloring effectively identifies the position of the interface and re-assigns particle color to keep them on "their" side of the interface. In the original colorblind CG-LBM implementation, fluids are individually recolored by all other fluids, one-by-one, through the color gradients $\boldsymbol{F}_{lm}$, as in equation (6.15) [3]. This means each fluid must interact with $N-1$ other fluids, for recoloring operations scaling with $\mathcal{O}(N^2)$

Since we have found the phase-fields $\rho_l^{\bar{N}(n)}$ of N-fluid CG-LBM, it may be possible to directly recolor fluids with their phase-field gradient $\nabla \rho_l^{\bar{N}(n)}$. Note indeed that the color-gradient between fluid l and all other fluids $\mu \neq l$ is:

$$\begin{aligned}
\boldsymbol{F}_{l\mu} &= \rho_\mu^{\bar{N}} \nabla \rho_l^{\bar{N}} - \rho_l^{\bar{N}} \nabla \rho_\mu^{\bar{N}} \\
&= \left(1 - \rho_l^{\bar{N}}\right) \nabla \rho_l^{\bar{N}} - \rho_l^{\bar{N}} \nabla \left(1 - \rho_l^{\bar{N}}\right) \\
\boldsymbol{F}_{l\mu} &= \nabla \rho_l^{\bar{N}(n)}
\end{aligned} \tag{10.1}$$

which is consistent with the idea that $\nabla\rho_l^{\bar{N}(n)}$ should include information about fluid l interfaces with any other fluid.

For $N = 2$ interfaces, where fluid l is anyway effectively recolored by a single fluid m, equation (10.1) (with $\mu \to m$) is already equivalent to the color-gradient $\boldsymbol{F}_{lm}$ that recolors fluid l. In any case, the presumed form of recoloring operations done directly with $\nabla\rho_l^{\bar{N}(n)}$ is, if a single segregation parameter β is in use:[1]

$$f_i^{l\star\star\star} = \Omega_i^{l,(3)}(f_i^{\star\star}) = \frac{\rho_l}{\rho} f_i^{\star\star} + \beta\frac{\rho_l}{\rho}\left(1 - \frac{\rho_l}{\rho}\right)\cos(\varphi_i^l) f_i^{\text{eq}}|_{\boldsymbol{u}=0} \tag{10.2}$$

where:

$$\cos(\varphi_i^l) = \frac{\boldsymbol{c}_i \cdot \nabla\rho_l^{\bar{N}(n)}}{|\boldsymbol{c}_i||\nabla\rho_l^{\bar{N}(n)}|}$$

This would reduce the number of recoloring operations by a whole order, down to $\mathcal{O}(N)$. The exact form of this single-phase-field recoloring, its mass- and momentum-conserving properties, and equivalence to standard recoloring should be investigated.

That being said, computations can also be saved by using operations nominally scaling with $\mathcal{O}(N^2)$, but that are only triggered for sufficient concentrations of a particular fluid. Instead of (or, in addition to) using fluid-pair concentration factor C_{lm}, boolean evaluations of sufficient phase-field or color-gradient magnitudes would determine which fluid-pairs interact in perturbation and recoloring.

10.2 Superviscous Particles

10.2.1 For $N = 1$ Single-Phase Flows

In chapter 8, a superviscous fluid was in fact able to capture the benchmark solution of a 1D momentum diffusion problem. Although the measurement of wall velocity was probably especially suited to be captured correctly,[2] this suggests that s-fluids could be used in other simple flows where applied forces can be readily converted to linear or rotational momentum. As long as the s-fluid particles have radial symmetry (such as for a sphere), particles would not be affected by spurious smearing in single-phase flows. For users equipped with a CG-LBM implementation, this may represent a practical way to investigate particle-laden flows without having to implement bounce-back on moving particles, or to decide how to initialize fluid nodes that are uncovered by a moving solid particle [2].

10.2.2 To Mediate Wetting

The spurious smearing issue in chapter 8 led to catastrophic non-physical deformation of a particle, before it could exhibit either solid- or fluid-like behavior. Because this occurred when an s-fluid particle was directly initialized at a fluid-fluid interface, it is not clear if these issues would occur with more "permissive" initializations away from fluid-fluid interfaces, or later in simulations where s-fluid particles move towards fluid-fluid interfaces.

When a fluid is initialized with a curved interface in CG-LBM, the segregation parameter β can be used to generate model-consistent diffuse interfaces. Consider an s-fluid particle initialized in a single other fluid. The perturbation step will begin to generate a pressure jump across the s-fluid/fluid interface. What this corresponds to physically, for a solid, is not clear, but it is known that N-fluid CG-LBM can reproduce static contact angles between fluids, despite resulting in sharp phase-field edges [3]. These contact angles are enforced by fluid-fluid perturbation: s-fluid particles might be more resilient to spurious smearing if the initialization allows for them to first develop a pressure jump with their surrounding fluid.

Under those conditions, one could study s-fluid particles moving *towards* fluid-fluid interfaces, and study how interface mobility or spurious smearing affects simulations.

[1] This would not allow the use of different segregation parameters β_{lm} for fluid-pairs lm. Special relations that locally redefine β to achieve higher accuracy in resolving small static three-phase contact angles are also probably no longer usable [3]. Note this is likely not an issue for dynamic simulations.

[2] Measuring mass-flux of s-fluid, for example, would have accounted for undesired shearing inside the s-fluid.

10.3 Solid-Phase Perturbation

10.3.1 Improved CG-SPM

The main weakness of the original CG-SPM approach in [4] is the lack of support of non-unity density ratios. As discussed in chapter 5, this is because the effective solid-fluid interface location implied by the color-gradient depends on the density of surrounding fluids. This is a feature of non-normalized phase-fields, which chapter 6 clarified were the phase-fields for the original colorblind CG-LBM used in CG-SPM [3, 4].

Users of CG-SPM could directly use the conclusions of chapter 6, and use a normalized phase-field, which does not lead to density-ratio-dependent phase-field interfaces. This should immediately extend the applicability of CG-SPM to non-unity density ratios.

10.3.2 Diffuse Solid Phase-Fields

In CG-SPM, a full additional fluid is defined to mediate wetting. This s-fluid has its own viscosity and population, which relaxes and streams (albeit confined by the desired solid geometry) [4]. The only desirable feature of this fluid's presence is its incorporation in the perturbation step in order to mediate wetting. The presence of the additional viscosity is in fact problematic, since it is a non-physical parameter, and complicates the use of the model at non-unity viscosity ratios.

Chapter 6 revealed a direct connection between phase-field and N-fluid color-gradients, which allowed us to directly define a solid phase field $\rho_S^{\bar{N}}$ in chapter 9. This solid phase-field was sufficient to use the perturbation operator to reproduce wetting phenomena. The method's inaccuracy for single-node solid-phase perturbation was attributable to the effective sharpness of solid-fluid phase-field interfaces, and is believed to be resolvable by a diffuse interface and solid phase-field.

Considering that CG-SPM users have already implemented diffuse solid interfaces [4, 6], the lessons of chapters 6 and 9 could be used to remove the presence of the additional fluid, and only use the solid phase field to mediate wetting. This would reduce computational costs associated with additional fluid relaxation and streaming, and remove the need for an additional viscosity.

Indeed, diffuse solid-fluid phase-field interfaces should resolve the inaccuracies of single-node SPP presented in section 9.2. Because fluids are *not* recolored by the wall (since "immiscibility" is enforced by bounce-back), diffuse solid-fluid interfaces should only be as thick as is required to achieve accurate wetting (i.e., a 1:1 correspondence of input and output static contact angles implied by all surface tensions) that is independent of density and viscosity ratios. The resulting energy-based wetting implementation might be applicable to the inkjet printing regime.

Because solid phase-fields could be used as "masks" following solid particles, and because dynamic contact angle response is probably tunable through the magnitude of the solid-liquid surface tensions [1], SPP with diffuse solid-phase fields might prove useful in capturing wetting on moving particles, and in adjusting meniscus response to the pressure waves in inkjet printing.

Chapter 10 References

[1] A. Kawasaki et al. “A lattice Boltzmann model for contact-line motions”. In: *Computers and Mathematics with Applications* 55.7 (2008). doi: 10.1016/j.camwa.2007.08.026.

[2] Timm Krüger et al. *The Lattice Boltzmann Method: Principles and Practice*. Graduate Texts in Physics. Springer, 2016.

[3] Sébastien Leclaire, Marcelo Reggio, and Jean-Yves Trépanier. “Progress and investigation on lattice Boltzmann modeling of multiple immiscible fluids or components with variable density and viscosity ratios”. In: *Journal of Computational Physics* 246 (2013). doi: https://doi.org/10.1016/j.jcp.2013.03.039.

[4] Y.K. Lee and K.H. Ahn. “Particle dynamics at fluid interfaces studied by the color gradient lattice Boltzmann method coupled with the smoothed profile method”. In: *Physical Review E* 101.5 (2020). doi: 10.1103/PhysRevE.101.053302.

[5] Haihu Liu, Albert J. Valocchi, and Qinjun Kang. “Three-dimensional lattice Boltzmann model for immiscible two-phase flow simulations”. In: *Phys. Rev. E* 85.4 (Apr. 2012). doi: 10.1103/PhysRevE.85.046309.

[6] Young Ki Lee. “Applications of lattice Boltzmann method combined with smoothed profile method for particulate flows: a brief review”. In: (Oct. 21, 2023). doi: 10.1007/s13367-023-00077-8.

Part IV

Appendices

Appendix A | Systematic Literature Review

This appendix details the systematic literature search process used to identify the research gap to emerge from the research question from chapter 1:

How can Lattice Boltzmann Methods be used to simulate multiphase flows with dynamic capillary phenomena?

A.1 Research Database Selection

The following databases were selected from the TU Delft library recommended sources for Mechanical Engineering:

- Scopus
- Web of Science

The selection was made according to the following additional criteria:

- focus on academic publications,
- support of advanced search with boolean search operators,
- search engine with “relevance” metric,
- ability to filter, save, and merge search results,
- ability to export citations to a citation management format.

A.2 Advanced Search

For a single search, the first 25 most relevant papers are retained (based on the search engine’s own assessment), along with the 25 most recent in order to orient results towards new results. These two sets of results may overlap. Each search employs additive (each are added with `AND`) boolean search field to the content inside the title, abstract, and keywords of a search result. Search fields are divided in *universal* fields, which are always applied, and *filter* fields. Individual advanced searches always include all universal fields, and a combination of filter fields. For a given set of filter fields, all possible combinations are tested.

To target boundary-condition-based wetting implementations typical of CG-LBM, the following search field set was used:

Search Field Set 1 - Universal Fields

- `lattice AND boltzmann`
- `wetting`
- `boundary AND condition`

Filter Fields

- `curved OR moving`
- `(color AND gradient) or (rothman)`

To target wetting implementations for moving or curved boundaries with applications to particle-laden flows especially:

Search Field Set 2 - Universal Fields

- `lattice AND boltzmann`
- `wetting`
- `(colloidal OR suspension) OR particle OR laden`

Filter Fields

- `curved OR moving`
- `(color AND gradient) or (rothman)`
- `“boundary condition” OR “boundary conditions”`
- `angle OR (contact AND line)`

The results of both search field sets, which may overlap, are combined.

A.3 Article Filtering

The following criteria were used to exclude articles from the accumulated references:

- the article is not in English,
- the article does not use LBM,
- the article couples LBM with a non-LBM method,
- the article's focus is AI/ML- or GPU-acceleration-related,
- the model considers heat transfer and/or phase change,
- the implementation is not tested for fluid density ratio above 100,
- the simulation does not model dynamic phenomena, or an equilibrium that is the outcome of dynamic phenomena,
- the model includes more than two fluids,

- the article not does not provide a clear analytical or experimental validation, or comparison with another source's numerical results,
- the model's wetting implementation is not clearly defined.

The filtering is operated in three phases:

1. on the basis of article titles and abstracts,
2. on the basis of a cursory read,
3. during the categorization process for outliers.

A.4 Categorization

Remaining articles are read and categorized following section 4.2.

Appendix B | Requirements on Independent Relaxation of Mixture Components

Section 6.1.2 describes how local mixture components in CG-LBM must all relax at the same rate. Although viscosity interpolation is free, reference [1] interpolates for a local mixture relaxation time τ_{eff} from the relaxation times τ_k of local components:

$$\tau_{\text{eff}} = \frac{1+\rho^N}{2}\tau_r + \frac{1-\rho^N}{2}\tau_b \tag{B.1}$$

where indices r and b respectively refer to the ($N = 2$) red and blue fluids, with the original CG-LBM phase field from equation (3.42). This interpolation is actually equivalent to a density-weighted arithmetic average of relaxation times, summed over all fluids k.

$$\tau_{\text{eff}} = \sum_k \left(\frac{\rho_k}{\rho}\right)\tau_k \tag{B.2}$$

Separately, during the relaxation step, reference [1] claims that individual fluid component populations f_i^k relax at their pure-fluid relaxation times τ_k to yield post-relaxation populations $f_i^{k\star}$:

$$f_i^{k\star} = \left(1 - \frac{\Delta t}{\tau_k}\right) f_i^k + \frac{\Delta t}{\tau_k} f_i^{k,\text{eq}} \tag{B.3}$$

and therefore claims that mixture components independently relax according to their pure-fluid relaxation times τ_k. This not only suggests that components do not collide with each other during the relaxation step, it also makes a hard claim on local viscosity, which is now constrained by equation (B.3).

For any N, a total population $f_i = \sum_k f_i^k$ is always defined, even if colorblind CG-LBM is not in use, at least to define the total momentum:

$$\rho u_\alpha = \sum_i f_i c_{i\alpha} = \sum_i \sum_k f_i^k c_{i\alpha} \tag{B.4}$$

and since relaxation conserves mass and momentum, the total population is always defined, including at equilibrium:

$$f_i = \sum_k f_i^k \tag{B.5}$$

$$f_i^{\text{eq}} = \sum_k f_i^{k,\text{eq}} \tag{B.6}$$

and indeed including during relaxation, to yield the total post-relaxation population $f_i^\star$:

$$f_i^\star = \sum_k f_i^{k\star} \tag{B.7}$$

Combining equations (B.7) and (B.3), we obtain:

$$f_i^\star = \sum_k f_i^k - \sum_k \frac{\Delta t}{\tau_k} f_i^k + \sum_k \frac{\Delta t}{\tau_k} f_i^{k,\mathrm{eq}}$$
$$f_i^\star = f_i - \Delta t \sum_k \frac{1}{\tau_k} f_i^k + \Delta t \sum_k \frac{1}{\tau_k} f_i^{k,\mathrm{eq}} \tag{B.8}$$

For consistency across CG-LBM steps, the effective local viscosity τ_{eff} relaxing the total population f_i in equation (B.2) must lead to a total relaxation equivalent in equation (B.8), *or vice versa.* By requiring the condition in equation (6.19):

$$f_i^k = \frac{\rho_k}{\rho} f_i$$

we find from equation (B.8):

$$f_i^\star = f_i - \Delta t \sum_k \frac{1}{\tau_k} \frac{1}{\rho_k/\rho} f_i + \Delta t \sum_k \frac{1}{\tau_k} \frac{1}{\rho_k/\rho} f_i^{k,\mathrm{eq}} \tag{B.9}$$
$$= f_i - f_i \Delta t \sum_k \left(\frac{1}{\frac{\rho_k}{\rho}\tau_k} \right) + f_i^{\mathrm{eq}} \Delta t \sum_k \left(\frac{1}{\frac{\rho_k}{\rho}\tau_k} \right)$$
$$f_i^\star = \left(1 - \frac{\Delta t}{\tau_{\text{eff}}}\right) f_i + \frac{\Delta t}{\tau_{\text{eff}}} f_i^{\mathrm{eq}} \tag{B.10}$$

recovering the claimed value of local relaxation τ_{eff} in equation (B.2). And so, requiring fluids to relax according to their pure-fluid relaxation times per equation (B.3), maintaining consistency with both the definition of a total population and the requirement for a single local relaxation rate τ_{eff} from equation (B.2), is contingent on the additional condition in equation (6.19).

Appendix B References

[l] Haihu Liu, Albert J. Valocchi, and Qinjun Kang. “Three-dimensional lattice Boltzmann model for immiscible two-phase flow simulations”. In: *Phys. Rev. E* 85.4 (Apr. 2012). doi: 10.1103/PhysRevE.85.046309.

Appendix C | Momentum Diffusion Circuits

Simple steady diffusion problems can be solved with *circuits*, in analogy to electric charge and heat diffusion [1]. We only consider 1D problems here.

Consider the flow of momentum τ for shear momentum diffusion in a 1D Couette Flow [2]:

$$\tau = \rho\nu\frac{\partial u}{\partial y} \tag{C.1}$$

where ρ and ν are fluid density and kinematic viscosity, u is velocity, and y is the coordinate normal to the fluid bounds. For steady-state Couette flow, the velocity gradient is constant and determined by the velocity difference ΔU across the fluid layer of thickness H:

$$\begin{aligned}\tau &= \rho\nu\frac{\Delta U}{H} \\ &= \frac{\Delta U}{H/(\rho\nu)} \\ \tau &= \frac{\Delta U}{R_\nu}\end{aligned} \tag{C.2}$$

where R_ν is *resistance to momentum diffusion*:

$$R_\nu = \frac{H}{\rho\nu} \tag{C.3}$$

where $\rho\nu = \mu$ dynamic viscosity plays the same role as heat conductivity in analogous heat circuits [1].

Figure C.1 shows a simple single-resistance momentum diffusion circuit. This approach is convenient to solve $N > 1$ multilayered Couette flows, since resistances can be aligned in series, with each resistance representing a different fluid layer. The amount of shear flowing through each resistance is the same at steady state. Total resistance $\sum R_\nu$ across all layers can be used with boundary velocities to find total shear flow, and then to solve for velocities across individual layers. The problem can also be solved with a matrix system, as with other circuits-based approaches [1, 3].

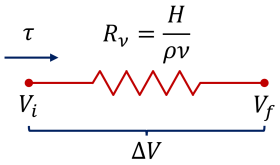

Figure C.1: Single-Resistance Momentum Diffusion Circuit, across a velocity difference ΔV and momentum diffusion resistance R_ν, which define the momentum flow τ across the circuit.

Appendix C References

[1] Theodore L. Bergman et al. *Fundamentals of Heat and Mass Transfer*. 8th ed. 1 online resource (1045 pages) vols. New York: Wiley, 2017.

[2] Pijush K. Kundu et al. *Fluid Mechanics*. Sixth edition. Amsterdam: Elsevier/AP, 2016.

[3] Sébastien Leclaire, Marcelo Reggio, and Jean-Yves Trépanier. "Progress and investigation on lattice Boltzmann modeling of multiple immiscible fluids or components with variable density and viscosity ratios". In: *Journal of Computational Physics* 246 (2013). doi: https://doi.org/10.1016/j.jcp.2013.03.039.

Appendix D | 1D Slab Acceleration Benchmark

Section 8.1.2 uses a simple 1D shear flow to study the use of s-fluids to convert shear forces to linear momentum. This situation can also be simulated using the case represented in figure D.1.

In the bulk of the fluid, the Navier-Stokes equations in 1D with flow orthogonal to the width of the channel (as in $N = 1$ fluid Couette flow) yields a 1D momentum diffusion equation:

$$\frac{\partial u}{\partial t} = \nu_f \frac{\partial^2 u}{\partial x^2} \tag{D.1}$$

where u is the flow velocity, and ν_f is fluid kinematic viscosity (also momentum diffusivity). At the left wall, fluid velocity matches the constant imposed wall velocity U which drives the flow:

$$u|_{x=0} = U \tag{D.2}$$

At the right wall, the shearing momentum flow from the bulk is transferred to the wall, accelerating it. This acceleration is a momentum change over time, which must match the flux from the wall:

$$-\rho_f \nu_f \frac{\partial u}{\partial x}\bigg|_{x=H} = L\rho_S \frac{dV_{\text{wall}}}{dt} \tag{D.3}$$

where L is the half-width of the slab which is effectively accelerated by the flow, ρ_S is solid density, and $V_{\text{wall}} = u|_{\text{right}}$ is the slab velocity, which due to no-slip must also be the flow velocity at the right wall.

D.1 Semi-Analytical Solution

The introduction of the particle lengthscale L also implies the introduction of a particle acceleration timescale t_a. Although it can also be found through dimensional analysis, equation (D.3) can also be simplified to reveal approximate particle response.

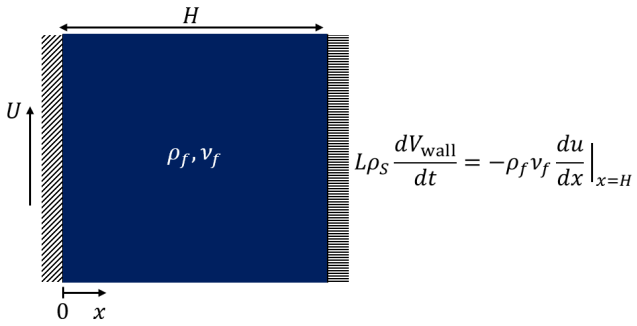

Figure D.1: 1D $N = 1$ Couette Flow with Accelerated Wall. The left wall moves at constant velocity U, whereas the right wall is progressively accelerated by the flow. This is the 1D approximation of the acceleration of a solid slab by a shear flow in a channel, shown in figure 8.4.

For a heavy particle, the timescale of momentum diffusion in the fluid layer $t_\nu = H^2/\nu$ is shorter than t_a, and the right-hand wall is almost fixed. This leads to a linear Couette-flow-like velocity profile to develop in the fluid layer, between the velocities at the left wall U and the right V_{wall}. Therefore, we have:

$$\frac{\partial u}{dx} \approx \frac{V_{\text{wall}} - U}{H - 0}$$

In this limit, we write from equation (D.3):

$$L\rho_S \frac{dV_{\text{wall}}}{dt} = -\rho_f \nu_f \frac{V_{\text{wall}} - U}{H}$$

and with:

$$\begin{aligned} V^* &= V_{\text{wall}} - U \\ dV^* &= dV_{\text{wall}} \end{aligned}$$

we have:

$$\begin{aligned} L\rho_S \frac{dV^*}{dt} &= -\rho_f \nu_f \frac{V^*}{H} \\ \frac{dV^*}{V^*} &= -\frac{\rho_f \nu_f}{\rho_S H L} dt \\ \frac{dV^*}{V^*} &= -\frac{1}{t_a} dt \end{aligned} \tag{D.4}$$

with the particle acceleration timescale t_a:

$$\boxed{t_a = \frac{\rho_S H L}{\rho_f \nu_f}} \tag{D.5}$$

and integrating equation D.4 and reversing our substitution, for an initial state $t = 0$ with quiescent flow and slab:

$$\begin{aligned} \ln V^*\big|_{t=0}^{t} &= -\frac{t}{t_a}\Big|_{t=0}^{t} \\ \ln\left(\frac{V_{\text{wall}} - U}{-U}\right) &= -\frac{t}{t_a} \\ -\frac{V_{\text{wall}}}{U} + 1 &= e^{-t/t_a} \\ \frac{V_{\text{wall}}}{U} &= 1 - e^{-t/t_a} \end{aligned} \tag{D.6}$$

Depending on the ratio between t_ν and t_a, we can expect this response to vary with a scalar k (depending also on fluid-layer Reynolds number), for a rough semi-analytical solution:

$$\boxed{\frac{V_{\text{wall}}}{U} \approx 1 - e^{-k\frac{t}{t_a}}} \tag{D.7}$$

A light solid $t_\nu > t_a$ will respond faster and the right wall approaches a free-slip boundary condition. A heavy solid $t_\nu < t_a$ will respond slower and the right wall approaches a no-slip boundary condition for a resting wall.

D.2 Finite Difference Benchmark Solution

A Finite Difference scheme was used to solve the numerical problem posed by equations (D.1), (D.2), and (D.3), with resting initial conditions. A Crank-Nicolson scheme was chosen for its second-order accuracy in time and space, and unconditional stability [1].

In the bulk, from equation (D.1), we find for the velocity u_i^t at node indexed i and timestep t:

$$-au_{i-1}^{t+1} + (1+2a)u_i^{t+1} - au_{i+1}^{t+1} = au_{i-1}^t + (1-2a)u_i^t + au_{i+1}^t \tag{D.8}$$

with:

$$a = \frac{\nu_f \Delta t}{2(\Delta x)^2} \tag{D.9}$$

The LHS of equation (D.8) yields a tridiagonal system matrix for the array of velocities at $t+1$. The RHS vector contains only known values in the bulk.

At the left boundary, we have a constant velocity which is directly substituted in the bulk-solution equation for the first node off the boundary, yielding for the first inner node at $x_{i=1} = 0 + \Delta x$:

$$(1+2a)u_1^{t+1} - au_2^{t+1} = 2aU + (1-2a)u_1^t + au_2^t \tag{D.10}$$

with a LHS which does not change the system matrix in its upper left corner, and a known RHS which directly incorporates the left-wall velocity at $x = 0$, a point which is not in the velocity solution vector.

At the right boundary $i = N$, Crank-Nicolson yields for equation (D.3), with a second-order accurate backward finite difference for the spatial derivative:

$$-\frac{1}{2}bu_{N-2}^{t+1} + 2bu_{N-1}^{t+1} + \left(1 - \frac{3}{2}b\right)u_N^{t+1} = \frac{1}{2}bu_{N-2}^t - 2bu_{N-1}^t + \left(1 + \frac{3}{2}\right)u_N^t \tag{D.11}$$

The LHS changes the system matrix at the boundary to maintain second order accuracy. The RHS is modified accordingly.

Appendix D References

[1] Steven C. Chapra and Raymond P. Canale. *Numerical methods for engineers.* 6th ed. Boston: McGraw-Hill, 2010.